



8-1998

Angle-Resolved Studies of Inner Shell Excitations for Argon, Krypton and Xenon using Third Generation Synchrotron Sources

Ahmad H. Farhat
Western Michigan University

Follow this and additional works at: <https://scholarworks.wmich.edu/dissertations>

 Part of the Physics Commons

Recommended Citation

Farhat, Ahmad H., "Angle-Resolved Studies of Inner Shell Excitations for Argon, Krypton and Xenon using Third Generation Synchrotron Sources" (1998). *Dissertations*. 1563.
<https://scholarworks.wmich.edu/dissertations/1563>

This Dissertation-Open Access is brought to you for free and open access by the Graduate College at ScholarWorks at WMU. It has been accepted for inclusion in Dissertations by an authorized administrator of ScholarWorks at WMU. For more information, please contact wmu-scholarworks@wmich.edu.



ANGLE-RESOLVED STUDIES OF INNER SHELL EXCITATIONS FOR
ARGON, KRYPTON AND XENON USING THIRD GENERATION
SYNCHROTRON SOURCES

by

Ahmad H. Farhat

A Dissertation
Submitted to the
Faculty of The Graduate College
in partial fulfillment of the
requirements for the
Degree of Doctor of Philosophy
Department of Physics

Western Michigan University
Kalamazoo, Michigan
August 1998

ANGLE-RESOLVED STUDIES OF INNER SHELL EXCITATIONS FOR
ARGON, KRYPTON AND XENON USING THIRD GENERATION
SYNCHROTRON SOURCES

Ahmad H. Farhat, Ph.D.

Western Michigan University, 1998

This dissertation, which is in the area of atomic physics, concentrates on the study of the interaction between VUV-soft X-ray radiation and atoms in the gas phase. The main area of interest is the study of Auger decay in atoms utilizing the process known as the resonance Auger effect, where an inner shell electron is excited to an unfilled orbital followed by the ejection of an Auger electron. The measurements in this thesis were performed by using the high resolution Atomic, Molecular and Optical Physics undulator beam line, which utilizes a spherical grating monochromator at the Advanced Light Source at Lawrence Berkeley National Laboratory. The research focused on three rare gases, argon, krypton and xenon. For argon, high resolution angular-resolved measurements of the $2p \rightarrow 4s, 3d, 4d$ resonant Auger lines have been achieved. By measuring photoelectron spectra simultaneously at two different angles using efficient time of flight spectrometers, the angular distributions anisotropy parameters β have been measured, and relative intensities have been evaluated for each of the resolved final ionic states. For krypton, the resonant Auger decay of all the photoexcited $Kr 3d_{3/2,5/2}^{-1} nl$ ($n = 5-9$) states have been studied using an angle resolved two dimensional photoelectron spectroscopic technique, in which

the electron yield was measured as a function of both photon energy and electron kinetic energy. Angular distributions, spectator and shake probabilities have been derived for the Kr $3d^{-1}np \rightarrow 4s^{-1}4p^{-1}mp + e^{-}$ ($n = 5-9$, $m = 5-11$) resonance Auger decay. The results show that the spectator-core coupling is strong at lower n ($n = 5,6$) but it lessens for higher n , with a shake up of $m = n+1$ preferred. Finally for xenon, the autoionization resonances and angular distribution of the $4d \rightarrow 6p$ decay spectrum were studied utilizing the Auger resonant Raman effect. Using this technique, β parameters of almost all $5p^4$ (3P , 1D , 1S) $6p$ final ionic states were determined. These results contribute to our understanding of atomic structure and dynamics of inner shell processes and hopefully will stimulate further experimental and theoretical work.

INFORMATION TO USERS

This manuscript has been reproduced from the microfilm master. UMI films the text directly from the original or copy submitted. Thus, some thesis and dissertation copies are in typewriter face, while others may be from any type of computer printer.

The quality of this reproduction is dependent upon the quality of the copy submitted. Broken or indistinct print, colored or poor quality illustrations and photographs, print bleedthrough, substandard margins, and improper alignment can adversely affect reproduction.

In the unlikely event that the author did not send UMI a complete manuscript and there are missing pages, these will be noted. Also, if unauthorized copyright material had to be removed, a note will indicate the deletion.

Oversize materials (e.g., maps, drawings, charts) are reproduced by sectioning the original, beginning at the upper left-hand corner and continuing from left to right in equal sections with small overlaps. Each original is also photographed in one exposure and is included in reduced form at the back of the book.

Photographs included in the original manuscript have been reproduced xerographically in this copy. Higher quality 6" x 9" black and white photographic prints are available for any photographs or illustrations appearing in this copy for an additional charge. Contact UMI directly to order.

UMI

A Bell & Howell Information Company
300 North Zeeb Road, Ann Arbor MI 48106-1346 USA
313/761-4700 800/521-0600

UMI Number: 9840036

UMI Microform 9840036
Copyright 1998, by UMI Company. All rights reserved.

**This microform edition is protected against unauthorized
copying under Title 17, United States Code.**

UMI
300 North Zeeb Road
Ann Arbor, MI 48103

Copyright by
Ahmad H. Farhat
1998

To the one who gives, and never asks for return.

To the one who developed in me the strong will
and the solid determination.

To the one who paved my way to success.

To the secret of my existence in this world.

To my mother Mariam.....

I dedicate this work of mine

ACKNOWLEDGMENTS

First of all, I would like to express my sincere appreciation to my advisor Dr. Nora Berrah, not only for her significant support and continuous encouragement, but also for her great help and valuable advice without which this dissertation would have never been able to be brought into existence.

I am also deeply indebted to Dr. Burkhard Langer for his endless assistance throughout the years of my research. His remarkable contributions with regard to the analysis of data, together with his constant readiness and willingness to help at any work related problem have definitely made this dissertation more complete. Similarly, I wish to thank Dr. Ant Wills for his important aid in performing the work.

The members of the committee: Dr. Thomas Gorczyca, Dr. Emanuel Kamber, Dr. Gerald Hardie, and Dr. Gordon Berry are greatly acknowledged for spending their time to review my work, and for their supervision and collaborations.

I also would like to thank my very close friend Nabil Amro for his help whenever I needed him.

Enough gratitude can not be possibly expressed to my parents, Hussein and Mariam, and to my elder brother Mohamad for their limitless support and constant interest in my academic progress, nor can it be expressed to my wife Wadad for her ambitious care for me and for our son, Ali, or for her marvelous patience to bear with me spending tremendous time in front of my computer at my desk with stacks of pap-

Acknowledgments-Continued

ers to be finally able to achieve this dream of life.

Ahmad H. Farhat

TABLE OF CONTENTS

ACKNOWLEDGMENTS.....	ii
LIST OF TABLES.....	vi
LIST OF FIGURES.....	viii
CHAPTER	
I. INTRODUCTION.....	1
II. THEORETICAL BACKGROUND.....	7
Partial Photoionization Cross-section and Asymmetry Parameters.....	7
Normal Auger and Resonant Auger Process.....	12
III. EXPERIMENTAL TECHNIQUE.....	14
Synchrotron Radiation.....	14
Experimental Station.....	18
The Measuring Electronics.....	22
Two-dimensional Photoelectron Spectrum.....	23
IV. ANGLE-RESOLVED STUDY OF ARGON $2p^{-1}_{1/2,3/2}$ ns,d REONANT AUGER DECAY.....	25
Abstract.....	25
Introduction.....	25
Results and Discussion.....	27
The $2p^{-1}4s$ Resonant Auger Spectra.....	29

Table of Contents-Continued

CHAPTER		
	The 2p ⁻¹ 3d Resonant Auger Spectra.....	38
	The 2p ⁻¹ 4d Resonant Auger Spectra.....	44
	Conclusion.....	47
V.	RESONANT AUGER STUDIES IN KR 3d _{3/2,5/2} ⁻¹ np STATES USING ANGLE-RESOLVED ELECTRON IMAGING SPECTROSCOPY.....	51
	Abstract.....	51
	Introduction.....	52
	Results and Discussion.....	53
	Conclusion.....	68
VI.	HIGH-RESOLUTION ANGLE-RESOLVED STUDY OF XE 4d → 6p RESONANT AUGER PROCESS.....	70
	Abstract.....	70
	Introduction.....	70
	Results and Discussion.....	71
	Conclusion.....	78
VII.	CONCLUSION.....	80
	REFERENCES.....	83

LIST OF TABLES

1.	Experimental and Theoretical Angular Distribution Anisotropy Parameters (β) for the Ar $p_{1/2}^{-1}4s$ Resonance.....	33
2.	Experimental and Theoretical Angular Distribution Anisotropy Parameters (β) for the Ar $2p_{3/2}^{-1}4s$ Resonance.....	34
3.	Experimental and Theoretical Relative Intensities for the Ar $2p_{1/2}^{-1}4s$ Resonance (Measured at the Magic Angle).....	36
4.	Experimental and Theoretical Relative Intensities for the Ar $2p_{3/2}^{-1}4s$ Resonance (Measured at the Magic Angle).....	37
5.	Experimental Relative Intensities (Measured at the Magic Angle) and β Parameters for the Ar $2p_{1/2}^{-1}3d$ Resonance.....	42
6.	Experimental Relative Intensities (Measured at the Magic Angle) and β Parameters for the Ar $2p_{3/2}^{-1}3d$ Resonance.....	43
7.	Experimental Relative Intensities (Measured at the Magic Angle) and β Parameters for the Ar $2p_{1/2}^{-1}4d$ Resonance.....	48
8.	Experimental Relative Intensities (Measured at the Magic Angle) and β Parameters for the Ar $2p_{3/2}^{-1}4d$ Resonance.....	49
9.	Experimental Spectator and Shake Probabilities (in Percentage of the Total Intensities of all the $4s^{-1}4p^{-1}(^1P)mp$) Resonances for the $3d^{-1}np \rightarrow 4s^{-1}4p^{-1}mp$ ($n = 5-9, m = 5-11$) Resonance Auger Transitions.....	62
10.	Experimental Angular Distribution Anisotropy Parameters (β) for the $3d^{-1}np \rightarrow 4s^{-1}4p^{-1}mp$ ($n = 5-9, m = 5-11$) Resonance Auger Transitions.....	68
11.	Intensities and β Parameters of the Electron Spectrum of Xe $4d_{5/2} \rightarrow 6p$ Excitation (65.11 eV).....	76

List of Tables-Continued

12. β Parameters of the Electron Spectrum of Xe After $4d_{3/2} \rightarrow 6p$
Excitation With Previous, Low Resolution Data.....78

LIST OF FIGURES

1.	Differential Cross Section for Different β Parameter Using Linearly Polarized Light.....	11
2.	Schematic Contrasting Auger Processes.....	13
3.	Plan View of the ALS and Adjacent Buildings, Showing the Main Elements of a Light Source.....	16
4.	Schematic Diagram of the Experimental Setup Showing Two Time of Flight (TOF) Electron Spectrometers Mounted to a Rotatable Chamber.....	20
5.	Time of Flight Electron Analyzer With a Zoom-in Part of its Entrance.....	21
6.	Photon Energy Scan Over the Ar $2p^{-1}nl$ Resonances, Taken in the Ionization Threshold Region of the $2p_{3/2}$ (248.6 eV) and $2p_{1/2}$ (250.78 eV) Shells [4]...	27
7.	Complete Photoelectron Spectra for the $2p^{-1}4s$ Resonances (A, B), the $2p^{-1}3d$ Resonances (C, E), and the $2p^{-1}4d$ Resonances (D, F).....	28
8.	Auger Decay Spectra for Ar $2p_{1/2}^{-1}4s$ Resonance Shown at (a) $\theta = 0^\circ$ and (b) $\theta = 54.7^\circ$	30
9.	Auger Decay Spectra for Ar $2p_{3/2}^{-1}4s$ Resonance Shown at (a) $\theta = 0^\circ$ and (b) $\theta = 54.7^\circ$	31
10.	Auger Decay Spectra for Ar $2p_{1/2}^{-1}3d$ Resonance Shown at (a) $\theta = 0^\circ$ and (b) $\theta = 54.7^\circ$	40
11.	Auger Decay Spectra for Ar $2p_{3/2}^{-1}3d$ Resonance Shown at (a) $\theta = 0^\circ$ and (b) $\theta = 54.7^\circ$	41
12.	Auger Decay Spectra for Ar $2p_{1/2}^{-1}4d$ Resonance Shown at (a) $\theta = 0^\circ$ and (b) $\theta = 54.7^\circ$	45
13.	Auger Decay Spectra for Ar $2p_{3/2}^{-1}4d$ Resonance Shown at (a) $\theta = 0^\circ$ and (b) $\theta = 54.7^\circ$	46

List of Figures-Continued

14. Three Dimensional Mapping of the Resonant Auger Landscape Measured at 0° Relative to the Polarization Plane.....54
15. Two-dimensional (2D) Map Showing Auger Electron Emissions of the Rydberg Resonances Measured at 0° Relative to the Polarization Plane.....55
16. Photoelectron Spectrum of the $3d_{5/2} \rightarrow 5p$ Resonance Taken at the 54.7° With Respect to the Electric-field Vector of the Incident Radiation.
(a) Data Collected With no Retarding Potential. (b) Data Collected With -30 V Retarding Potential.....59
17. (a)-(g) Constant Ionic State Spectra of the $Kr^{+} np$ ($n = 5-11$) Extracted From the (2D) Display at 0° Relative to the Polarization Plane.....60
18. (a)-(g) Constant Ionic State Spectra of the $Kr^{+} np$ ($n = 5-11$) Extracted From the (2D) Display at 54.7° Relative to the Polarization Plane.....61
19. Constant Ionic State Spectra of the $Kr^{+} 5p$ Extracted From the (2D) Display at Two Different Angles (a) 0° and (b) 54.7° Relative to the Polarization Plane; (c) Shows the Angular Distribution Parameter β for the $3d^{-1}np \rightarrow 4s^{-1}4p^{-1}(^1P)5p$ ($n = 4-9$) Resonance Auger Transitions.....64
20. Constant Ionic State Spectra of the $Kr^{+} 6p$ Extracted From the (2D) Display at Two Different Angles (a) 0° and (b) 54.7° Relative to the Polarization Plane; (c) Shows the Angular Distribution Parameter β for the $3d^{-1}np \rightarrow 4s^{-1}4p^{-1}(^1P)6p$ ($n = 4-9$) Resonance Auger Transitions.....65
21. Constant Ionic State Spectra of the $Kr^{+} 7p$ Extracted From the (2D) Display at Two Different angles (a) 0° and (b) 54.7° Relative to the Polarization Plane; (c) Shows the Angular Distribution Parameter β for the $3d^{-1}np \rightarrow 4s^{-1}4p^{-1}(^1P)7p$ ($n = 4-9$) Resonance Auger Transitions.....65
22. Constant Ionic State Spectra of the $Kr^{+} 8p$ Extracted From the (2D) Display at Two Different Angles (a) 0° and (b) 54.7° Relative to the Polarization Plane; (c) Shows the Angular Distribution Parameter β for the $3d^{-1}np \rightarrow 4s^{-1}4p^{-1}(^1P)8p$ ($n = 4-9$) Resonance Auger Transitions.....66

List of Figures-Continued

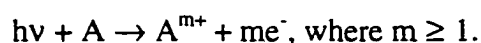
23. Constant Ionic State Spectra of the $\text{Kr}^+ 9p$ Extracted From the (2D) Display at Two Different Angles (a) 0° and (b) 54.7° Relative to the Polarization Plane; (c) Shows the Angular Distribution Parameter β for the $3d^{-1}np \rightarrow 4s^{-1}4p^{-1}(^1P)9p$ ($n = 4-9$) Resonance Auger Transitions.....66
24. Constant Ionic State Spectra of the $\text{Kr}^+ 10p$ Extracted From the (2D) Display at Two Different Angles (a) 0° and (b) 54.7° Relative to the Polarization Plane; (c) Shows the Angular Distribution Parameter β for the $3d^{-1}np \rightarrow 4s^{-1}4p^{-1}(^1P)10p$ ($n = 4-9$) Resonance Auger Transitions.....67
25. Constant Ionic State Spectra of the $\text{Kr}^+ 11p$ Extracted From the (2D) Display at Two Different Angles (a) 0° and (b) 54.7° Relative to the Polarization Plane; (c) Shows the Angular Distribution Parameter β for the $3d^{-1}np \rightarrow 4s^{-1}4p^{-1}(^1P)11p$ ($n = 4-9$) Resonance Auger Transitions.....67
26. (a) Photoelectron Spectra Taken at the Magic Angle on and Below the $4d_{5/2} \rightarrow 6p$ Resonance. (b) Resonant Decay Spectrum in the Kinetic Energy Range Between 33 and 42 eV Using 30 V Retarding Potential.....72
27. Decay Spectra of the $\text{Xe } 4d_{5/2} \rightarrow 6p$ Resonance Taken at the Magic Angle: (a) Aksela et al. [69] and (b) this Work. Resonance Spectra Taken at 0° : (c) This Work and (d) Carlson et al. [15].....73
28. $\text{Xe } 5p^4nl$ Decay Spectra After $4d_{5/2} \rightarrow 6p$ Resonant Excitation in the Kinetic Energy Range of 36.4-37.1 eV at (a) 0° , (b) 54.7° , and (c) 90° With Respect to the Polarization of the Incident photons.....75

CHAPTER I

INTRODUCTION

The study of atoms and molecules is one of the main topics of modern physics, and the field itself is very broad. Understanding of atomic structure and dynamics is an important focus of such field. Several experimental approaches have been used to understand atomic structure and dynamics such as atomic collision, laser spectroscopy, laser cooling and trapping, electron scattering by atoms and ions, photoionization, etc. To understand atomic structure and dynamics, we have chosen the approach of photoexcitation and photoionization, using synchrotron radiation.

Photoionization is a process where a photon of frequency ν and energy $h\nu$ interacts with atoms or molecules to produce ions and one or more electrons. The interaction can be represented by the following equation:



The quantity measured most directly is the ionization potential for the removal of the electrons from different atomic orbitals. According to an approximation known as Koopman's theorem [1] each ionization potential I_j is equal in magnitude to an orbital energy E_j which $I_j = -E_j$. In other word the ionization potential is what we call the binding energy of the state, which is the minimum energy needed to eject an electron to the continuum state. In each orbital j of an atom the electrons have characteristic

binding energy. When a photon $h\nu$ is absorbed by an atom, part of this photon energy is used to overcome this binding energy, I_j , the remainder, $h\nu - I_j$, must appear as kinetic energy (KE) of the ejected electrons:

$$KE = h\nu - I_j$$

If one records the photoelectron spectrum, the number of ionized electrons is detected at each energy, and a peak is found in the spectrum at each energy, $h\nu - I_j$, corresponding to the binding energy, I_j , of the electron.

The main goal of this dissertation is to study an atomic process known as the resonant Auger process, which represents an Auger-like decay of an excited state produced by resonant photoabsorption from an inner shell. At energies about 10 eV below the ionization potential of the core-shell electron, a photoabsorption resonance can occur to a virtual orbital. The excited neutral atom can then decay by an Auger process involving two valence-shell electrons, which results in filling the core vacancy with ejection of an Auger electron. The excited electron can either (a) remain in its orbital as a spectator electron, (b) be directly involved in the Auger process as a participator electron, (c) be shaken up as the result of the Auger process to a higher excited orbital, or (d) be shaken off into the continuum. As one increases the photon energy, higher-energy resonances occur with the production of different Auger processes until the ionization potential is reached. Studies of resonant Auger processes are best carried out with the help of storage rings emitting synchrotron radiation,

which is intense, continuous, selective and sufficiently energetic to excite core-shell electrons.

The Auger decay of core excited states in rare gases has been the subject of intense investigation over a number of years due to its complex nature. In krypton, for example, two strong series of resonances have been observed: $3d_{5/2} \rightarrow 5p,6p$ and $3d_{3/2} \rightarrow 5p,6p$ by Codling and Madden (1964) [2]. In 1968 Fano and Cooper [3] found that the transitions to nf orbitals are quite weak because of the large barrier of the effective potential for the f electrons. Similar resonances occur in argon below the $2p$ thresholds and in xenon approaching the $4d$ thresholds. A number of experiments have studied different aspects of the excitation and decay of a particular set of resonances for $Ar\ 2p \rightarrow ns, nd$, $Kr\ 3d \rightarrow np$ and $Xe\ 4d \rightarrow np$, which have been studied together because of their similarity as inner-shell resonances. Using electron impact, King et al. [4] and King and Read [5] measured energy loss spectra, equivalent to photoabsorption scans. Their high-resolution experiment provides precise energies for the $Ar\ 2p_{3/2,1/2}^{-1}ns,nd$, $Kr\ 3d_{5/2,3/2}^{-1}np$ and $Xe\ 4d_{5/2,3/2}^{-1}np$ resonances and $Ar\ 2p_{3/2,1/2}^{-1}$, $Kr\ 3d_{5/2,3/2}^{-1}$ and $Xe\ 4d_{5/2,3/2}^{-1}$ thresholds. Relative values of the oscillator strength f were determined and found to vary approximately with the separation of the resonance energy levels. Fano and Cooper [6] found the decrease in intensity, along a Rydberg series, results mainly from the overall expansion of the Rydberg orbital. For a given spin-orbit pair of resonances, e.g. $Kr\ 3d_{5/2} \rightarrow np$ and $3d_{3/2} \rightarrow np$, the measured ratios of oscillator strengths were very close to statistical calculations,

suggesting that relativistic effects have little influence on the transition strength of these resonances.

Combining synchrotron radiation and mass spectroscopy, Hayaichi et al. [7] examined the cross sections σ for the formation of singly, doubly and triply charged ions. For Ar $2p \rightarrow ns, nd$ excitations, Ar^+ was found to be the most frequent product of the resonant decay. By contrast, in both krypton and xenon, results were unexpected because the spectator model, in which the Rydberg electron remains in an outer orbital while the core undergoes an Auger-like decay and yields a singly charged ion. Hayaichi et al. [7], show that the autoionization to the valence s^{-1} and p^{-1} final states in Kr and Xe rarely occurs, which indicates that the spectator decay dominates the participator decay. The Rydberg electron could participate in the resonant decay in some other way, such as being excited (shake-up) or ionized (shake-off). For the most important pathway to doubly charged ions, Hayaishi et al. [7] proposed a two step process, such as $Kr\ 3d_{5/2}^{-1}5p \rightarrow Kr^+ 4s^{-1}4p^{-1}5p \rightarrow Kr^{++}4p^{-2}$, rather than a shake-off process.

Electron spectra at the Kr and Xe resonances have been investigated extensively: For both Kr [8] and Xe [9,10], the observed variations in valence cross sections σ_{ns} and σ_{np} caused by autoionization were small, less than 15 %. The electron spectra agree with the expectation of a valid spectator model with two important exceptions. Firstly, shake-up of the Rydberg electron during Auger-like decay contributes additional peaks, e.g. $Kr\ 3d^{-1}5p \rightarrow Kr^+4p^{-2}6p$ [8,11-13]. Secondly, on the Xe 4d

→ np resonances, Becker et al. [10] observed that shake-off contributed 44% of the total resonant intensity, without the non resonant σ_{sat} , σ_{5s} and σ_{5p} .

Angular distributions of the resonant Auger electrons in rare gases have been measured by several groups, [14-18] and an unusually large degree of angular anisotropy has been discovered. This unusually large degree of anisotropy in Ar was first explained by Cooper [19] who used angular momentum transfer theory and treated the resonant decay as a single-step process. Later Hergenhahn et al. [20] treated the resonant Auger transition as a two-step process involving excitation and subsequent Auger decay. They calculated the angular distributions of the resonant Auger transitions for Ar, Kr and Xe by describing the excited and final states in a jK coupling scheme and treating the outer electron as a spectator. Chen [21] has shown the importance of including the effect of intermediate coupling in the calculations of angular distributions of normal Auger decay. Later, Chen [22] reported calculations of the angular anisotropy of the resonant Auger transitions based on a two-step model for Ar, Kr and Xe with 2p-4s, 3d-5p and 4d-6p excitations, respectively. His calculations were carried out using the multiconfiguration Dirac-Fock (MCDF) method in intermediate coupling with configuration interaction.

In this thesis, we have used the high flux and high photon-resolution provided by the Advanced Light Source with two time-of-flight spectrometers to measure the intensity distributions and angular distributions (β parameters) for the Auger decay spectra following the inner-shell excitations in Ar, Kr and Xe.

Chapter II of this thesis is devoted to a brief theoretical background of the angular distribution anisotropy β parameters, and the difference between the normal Auger decay and the resonant Auger decay in detail. Chapter III describes first the Advanced Light Source, where all the experiments in this thesis were carried out, and second the experimental station and measuring electronics. Chapter IV presents the measurements of the intensity distributions and angular distributions of the Auger decay spectra following the $2p \rightarrow 4s$, $3d$, $4d$ resonant excitations in argon. Chapter V discusses the experimental results on photoexcitation and photoionization in krypton by measuring the Auger decay spectra of the $Kr\ 3d^{-1}np \rightarrow 4s^{-1}4p^{-1}mp$ ($n = 5-9$, $m = 5-11$). Chapter VI reports on the study of the angular distributions and decay rates of the $Xe\ 4d_{5/2} \rightarrow 6p$ resonant Auger lines. Finally Chapter VII gives a brief conclusion of this thesis.

CHAPTER II

THEORETICAL BACKGROUND

Partial Photoionization Cross-section and Asymmetry Parameters

In a photoelectron spectroscopy experiment, one measures the intensity $I(\theta)$ of the signal associated with photoelectrons emitted with a particular kinetic energy $E_{e,kin}$ and at a particular angle θ , with respect to the polarization vector of the incoming radiation. $I_i(\theta)$ can be written as a product of factors related to the design and performance of the spectrometer system and of factors related to the electronic properties of the atoms under investigation [23].

$$I(\theta) = \Phi_{h\nu} \times n_g \times Tr(E_{e,kin}) \times \Omega \times d\sigma / d\Omega \quad (2.1)$$

where $\Phi_{h\nu}$ is the absolute flux of the incoming radiation, n_g represents the target particle density, $Tr(E_{e,kin})$ is the transmission function of the electron energy analyzer, Ω represents the solid angle of electron collection, and $d\sigma/d\Omega$ is the differential partial cross-section. Obviously, as the only intrinsic atomic parameter, $d\sigma/d\Omega$ is the most interesting quantity in Eq. (2.1). According to Eq. (2.1) the differential partial cross-section is proportional to the intensities observed in photoelectron spectra. Unfortunately, the proportionality factor contains several elusive quantities, such as $\Phi_{h\nu}$ and

n_g , and the experimentalist will often have to be satisfied with the determination of the relative partial cross-sections.

The theoretical prescription for calculating the differential cross-section is based on Fermi's Golden Rule [24,25] and it has been shown [26-28] that $d\sigma/d\Omega$ is given by:

$$\frac{d\sigma}{d\Omega} = \frac{1}{4\pi\epsilon_0} \frac{4\pi^2 e^2 \hbar^2}{cm^2 \omega} \left| \left\langle \Psi_g \left| \sum_{\mu} e^{ik_{\omega} \cdot r_{\mu}} e_{\omega} \cdot \nabla_{\mu} \right| \Psi_f \right\rangle \right|^2 \quad (2.2)$$

where ϵ_0 is the permeability of the vacuum, e stands for the electronic charge, m is the mass of the electron, ω , k_{ω} and e_{ω} are the angular frequency, the momentum vector and the polarization vector of the incoming radiation, Ψ_g and Ψ_f represent the properly normalized wavefunctions for initial (ground) and final (ion + photoelectron) states, and r_{μ} and ∇_{μ} are the position and gradient vector operators of the μ -th electron. Because of the dependence of $d\sigma/d\Omega$ on Ψ_g and Ψ_f , the photoeffect provides a very direct probe of the electronic properties of the initial and final states. Since Eq. (2.2) is used to calculate the differential cross-section, the energy and the direction of the photoelectron, which is part of Ψ_f , have to be specified. The partial cross-section σ_i can be obtained by integrating $d\sigma/d\Omega$ over all directions [29]. Alternatively, by specifying the energy and the angular momentum of the photoelectron Eq. (2.2) can be employed to calculate the cross-section for a particular photoionization channel. In that case, σ may be evaluated over all relevant channels [29].

For photon energies below about 1 keV the wavelength of the radiation is much larger than the target dimensions and the exponential $\exp(ik_{\omega} \cdot r_{\mu})$ in Eq.(2.2) can be approximated to 1. This approximation, commonly referred to as the electric dipole approximation, is frequently invoked in the calculation of photoionization cross sections. With the assumption that the dipole approximation is valid, the differential cross-section is given by:

$$\frac{d\sigma}{d\Omega} = \frac{1}{4\pi\epsilon_0} \frac{4\pi^2 e^2 \hbar^2}{cm^2 \omega} \left\langle \left| \Psi_g \left| \sum_{\mu} e_{\omega} \cdot \nabla_{\mu} \right| \Psi_f \right| \right\rangle^2 \quad (2.3)$$

Relying on symmetry and angular momentum arguments, it has been shown [30-32] that when a linearly polarized photon interacts with an unpolarized target in the electric dipole approximation, the angular correlation between the incident photon and the ejected photoelectron is proportional to a linear combination of terms involving $(\cos\theta)^0$ and $(\cos\theta)^2$, where θ is the angle between the photoelectron and the polarization vector of the incident photon. The upper limit of two on the powers of $(\cos\theta)$ that determine the angular distribution is fixed by the total angular momentum of unity imparted to the target by the absorbed photon. The absence of a term linear in $(\cos\theta)$ is related to the conservation of parity in the photoionization process. Thus, the differential partial cross-section can be written as [33]:

$$\frac{d\sigma(h\nu)}{d\Omega}(\theta) = \frac{\sigma(h\nu)}{4\pi} \left\{ 1 + \frac{\beta(h\nu)}{4} [1 + 3P_1 \cos(2(\theta - \lambda))] \right\} \quad (2.4)$$

where σ is the partial cross section, β is the angular distribution anisotropy parameter, P_1 is the degree of linear polarization of the monochromatic light (we measured $P_1 = 0.99$ during the Ar, Kr and Xe experiments), and λ is the angle (tilt angle) between the synchrotron plane and the photon electric field vector (0° in all experiments). It can be seen from this relation that the entire angular dependence of the photoionization process can be ascribed solely to the β parameter. Special note should be taken of the angle $\theta_m = 54.7^\circ$ (the magic angle). With this value substituted into the above equation, the angular dependence drops out completely; in other words, the photoionization process is independent of β at this angle. By taking simultaneous measurements at the magic angle and 0° , the experimental values can be combined with equation (2.4) to yield an explicit result for β_{if} :

$$\beta_{if}(h\nu) = \frac{1}{\text{Eff}(h\nu - E_{bin})} \frac{Cts_0(h\nu)}{Cts_{54.7}(h\nu)} - 1 \quad (2.5)$$

where Eff represents the relative efficiency (transmission as a function of kinetic energy) of the detectors, Cts_0 represents the number of counts for a particular final ionic state measured at 0° and $Cts_{54.7}$ represents the number of counts measured at the magic angle (assuming 100% linear polarization and a tilt angle of 0°). The efficiency was calculated using the known β parameters for the 2s and 2p states of neon. With this relationship, the β parameter can be extracted. It can be seen from Eq. (2.4) that in order for the differential cross section to remain positive, β must range between -1 and 2 . With $\beta = 2$, most electron emission is in the direction of the electric-

field vector, $\beta = 0$ represents isotropic emission, and $\beta = -1$ implies emission primarily perpendicular to the electric-field vector. Figure 1 displays a polar plot of the differential cross section for several different β parameters, assuming 100% linearly polarized dipole radiation, and a tilt angle of 0° . All distributions are cylindrically symmetric with respect to the electric-field vector. Note that at a specific angle Θ_m , all the differential cross sections are independent of the β parameter. At this angle, all curves intersect for any β parameter. This magic angle is important for the experimentalist since one can use angle-resolved detectors in order to measure and extract both partial cross-sections and angular distributions.

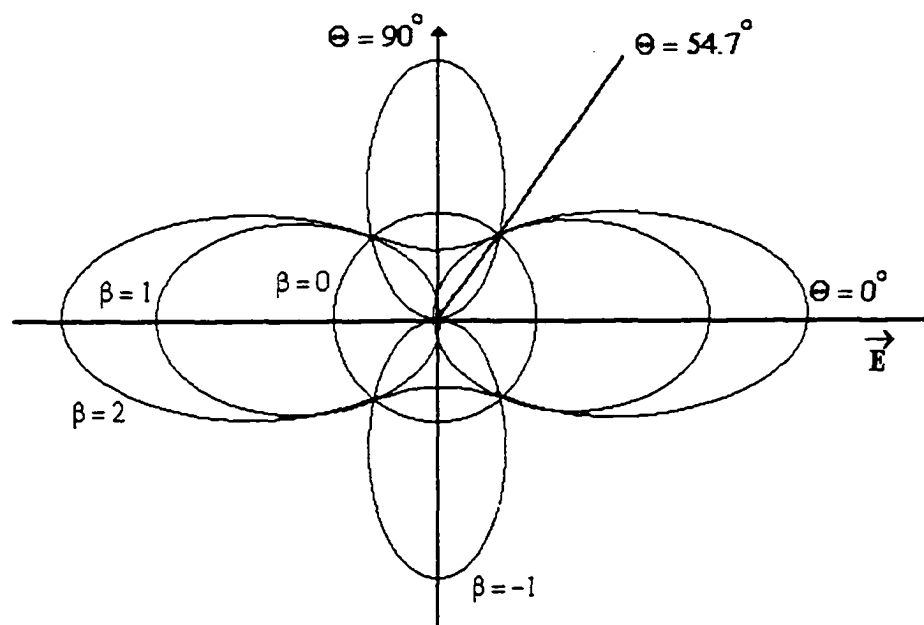
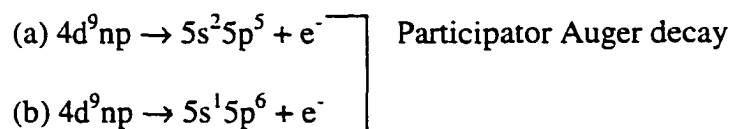


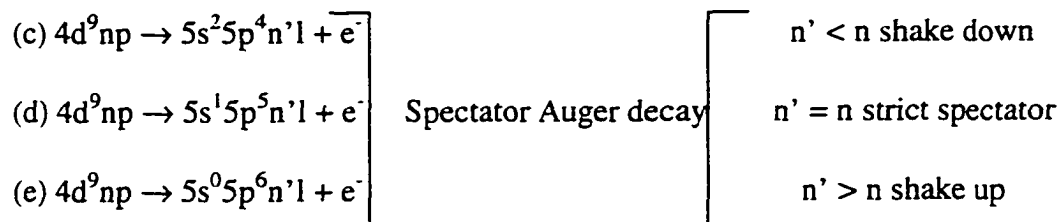
Figure 1. Differential Cross Section for Different β Parameter Using Linearly Polarized Light. It can be seen from this figure that the direction of the electron emission is along the electric field vector when the value of β is positive and equal to 2, while the direction of the electron emission is perpendicular to the electric field vector when β is negative and equal to -1 . The electron emission is isotropic when $\beta = 0$. It can be seen that at the magic angle, the electron emission is independent of β parameter.

Normal Auger and Resonant Auger Processes

Under irradiation with high energy photons, atoms emit at least two energetic electrons: the photoelectron from the initial ionizing event and an Auger electron from the decay of the original ion formed. The initial ionic state after photoelectron emission is an energetic ion with an electron vacancy in an inner shell. Upon decay by the Auger process, the inner vacancy is filled by one electron from an outer shell and another electron is emitted from the same or another outer shell [34]. The energy difference of the initial ion and the final doubly charged ion appears as kinetic energy of the emitted Auger electron. The normal Auger process leads to discrete lines in an electron spectrum. Figure 2a shows schematically the case where a Xe $4d_{5/2}$ electron is photoionized. The hole is filled by a 5p electron and another 5p electron is ejected [35].

The resonant Auger process, which can also be referred to as an autoionization resonance, is usually dominated by the “spectator structure” where the inner shell electron is excited to one of the Rydberg orbitals, described by corresponding quantum numbers n, l, j . In this case, the electronic core relaxes by Auger transition that exposes the Rydberg electron to a changed field of the ion, from singly to doubly charged. As a result, it may change its quantum numbers to n', l', j' . The different decay channels can be summarized, in the case of the $4d \rightarrow np$ transitions in Xe, into five main groups as follows:





If $n = n'$, $l = l'$ and $j = j'$, we would have a pure spectator transition; but if $n < n'$, $l = l'$ and $j = j'$ we would have a shake-up or shake-off; and if $n > n'$, $l = l'$ and $j = j'$ we would have a shake-down ((c)-(e)). The Rydberg electron may also participate in filling the core hole, which leads to a similar final state as in direct photoionization, where we would have participator transitions (a) and (b). It has been shown that the participator transitions are overwhelmingly less intense than the spectator transitions [7]. Figure 2b and Figure 2c show the case of an excitation of the Xe $4d_{5/2}$ electron into the $6p$ level.

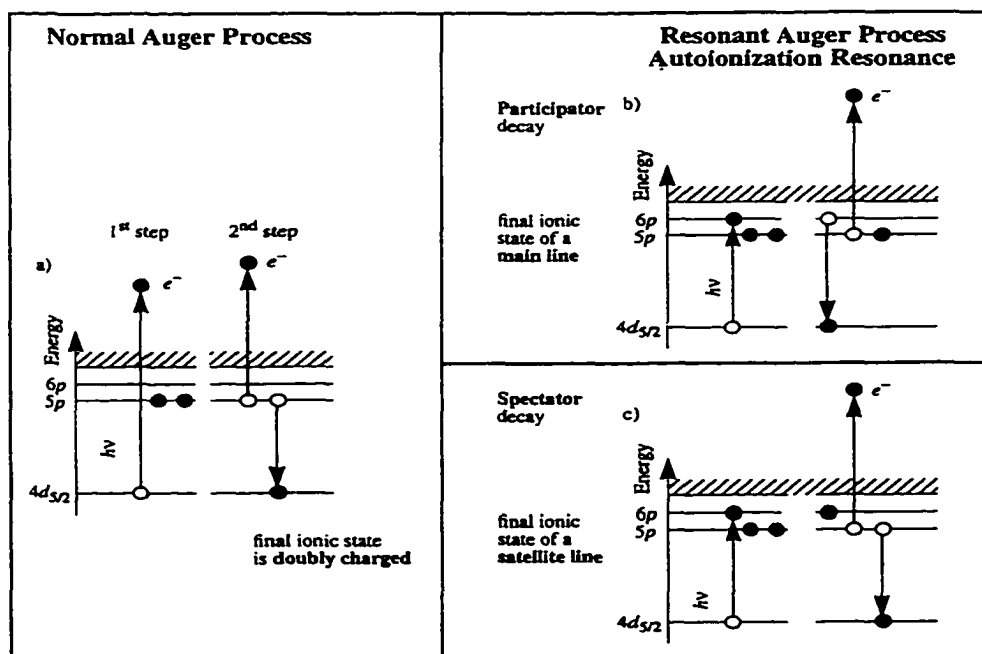


Figure 2. Schematic Contrasting Auger Processes. The left half of the diagram (a) shows a normal Auger process. The right half of the diagram (b, c) shows the resonant Auger decay.

CHAPTER III

EXPERIMENTAL TECHNIQUE

Synchrotron Radiation

When charged particles, in particular electrons or positrons, are forced to move in a circular orbit, photons are emitted. With charged particles at relativistic velocities, these photons are emitted in a narrow cone in the forward direction, at a tangent to the circular orbit. In a high-energy electron or positron storage ring, these photons are emitted with energies ranging from infrared to energetic (short wavelength) X-rays. This radiation is called Synchrotron Radiation. Such emission was first observed at General Electric's 70 MeV synchrotron in 1946 [36]. The history of the synchrotron sources can be divided into a number of generations. The first extraction of synchrotron radiation from a synchrotron source was made in 1963. These earliest beams had typical photon fluxes of 10^6 to 10^8 photons per second, and were used also to conduct photoabsorption experiments although the electron beams were mainly used for high-energy physics. In the 1980's the second generation of synchrotron sources appeared. The main purpose of these new machines was the generation of radiation. These new storage rings (synchrotrons with long lifetime of the particle beam) produced radiation by passing an electron or positron beam through bending magnets to keep the electrons or the positrons in a closed orbit. When these beams are bent by magnets, they emit energy in the form of synchrotron radiation,

whose resolution was sufficient to study complex features such as two-electron processes in atoms, autoionization resonances, photoexcited Auger effects and several other photoionization and photoexcitation processes. Another aspect of this period was the exploration of insertion devices, which consist of periodic arrays of magnets. These devices add transversal oscillations to the motion of the charged particles, generating synchrotron radiation with properties that are superior to the bending magnet [37]. These new insertion devices, namely “wigglers” and “undulators”, are what characterize the current third generation synchrotron radiation sources, where all the experiments of the present thesis were performed [37]. Figure 3 presents schematically the principal elements of a third generation synchrotron source, in this case the Advanced Light Source (ALS), at Lawrence Berkeley National Laboratory since this facility was used for the experiments that are reported in this thesis. The main components of the ALS are:

1. The linear accelerator: The linear accelerator, or linac, is the electromagnetic catapult that accelerates electrons to relativistic velocity. The linac is four meters long, and has three major parts: (1) The electron gun; (2) The buncher, whose purpose is to accelerate the pulsing electrons as they come out from the electron gun and pack them into bunches; and (3) The linac itself, which is an extension of the buncher it receives radio frequency (RF) power to accelerate the electrons and compact them into tighter bunches. Electrons enter the linac from the buncher at a velocity of $0.6c$.

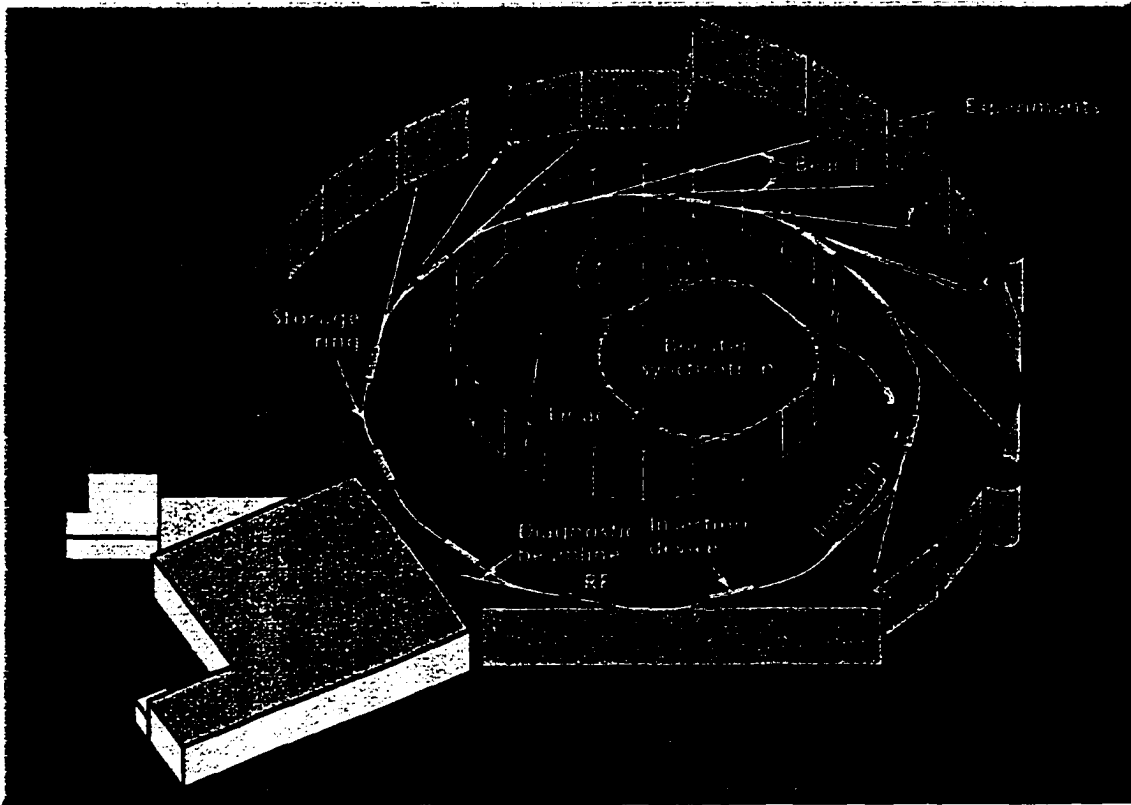


Figure 3. Plan View of the ALS and Adjacent Buildings Showing the Main Elements of a Light Source.

2. The Booster synchrotron: To have a linac long enough to accelerate electrons to the energy needed by the ALS would not be feasible since it would not fit inside the building. Instead, a circular booster synchrotron is used in which the electrons receive a "boost" from an accelerating chamber (RF cavity) each time they go around the booster ring. In less than one second inside the booster, the electrons make 1,300,000 revolutions (and travel 98,000 kilometers), reach 99.999994% of the speed of light, attain their target energy (usually 1.5 billion electron volts), and are ready to be transported to the storage ring.

3. The storage ring: Once the electrons reach their target energy in the booster synchrotron, an injection system transfers them from the booster to the storage ring

where they circulate for hours. The electrons travel in an aluminum vacuum chamber that has fewer atoms per unit volume than the outer space (the pressure is about 10^{-9} Torr), so there are almost no collisions to slow them down. The storage ring is roughly circular with 12 arc-shaped sections (about 10 meters long) joined by 12 straight sections (about 6 meters long). Hundreds of precision electromagnets focus and bend the electron beam as it circles the storage ring more than a million times a second. Electrons, curving through the ring's 12-arc sections, emit fanlike beams of photons. Between these curves there are straight sections where insertion devices, undulators and wigglers, wiggle the electrons back and forth to form a narrow beam of light 100 million times brighter than conventional x-ray sources. The synchrotron light emitted by the electrons is directed to beamlines through beam ports.

4. Undulators and Wigglers: The brightest synchrotron light at the ALS comes from undulators (located in the straight sections of the storage ring) that contain over one hundred magnetic poles lined up in rows above and below the electron beam. The magnets force the electrons into a snake-like path, so that the light from all the curves adds together. Although they are about 4.5 meters long and weigh about 40,000 pounds, the undulators have to be built to extreme precision. Many of the design tolerances are approximately 50 microns, less than the width of a human hair. Wigglers are similar to undulators but have fewer magnetic poles. All the measurements for the present thesis were performed using the 8-cm 55-period U8 undulator of beamline 9.0.1. The undulator is capable of producing intense UV and soft x-ray photons with a typical flux of approximately 10^{13} photon/s [38].

5. Beamline: The beamline transfers the photons from the storage ring to the experimental chamber. In all of the present work, we used beamline 9.0.1. which is the undulator atomic, molecular and optical physics beamline. The radiation produced by the undulator at this beam is monochromatized by a spherical grating monochromator. The monochromator has three different grating: 380, 925 and 2100 l/mm. The broadband radiation reflects from the grating and is spatially dispersed by wavelength. A pair of entrance and movable exit slits select the desired wavelength. The width of the slits determines the photon resolution. After reflection from one of the gratings, photon energies of 20-310 eV are available for use. The degree of the linear polarization P_1 of the monochromatic light has been measured to be 0.99. In this thesis we have performed three experiments for three different energy ranges. For the argon $2p^{-1}_{1/2,3/2}$ ns,d Auger decay study, the energy range was 243.5-250 eV using the monochromator set to its third grating (2100 l/mm). The average photon resolution was 107 meV. The energy range for the krypton $3d^{-1}_{3/2,5/2}$ np Auger decay study was 90-95 eV and the monochromator was set to the second grating (925 l/mm), with an average photon resolution of 40 meV. Finally for the xenon $4d^{-1}_{3/2,5/2}$ 6p Auger decay, the spectra were taken at a photon energy of about 65 eV, which corresponds to the first grating (380 l/mm) of the monochromator. The average photon resolution was 15 meV for this experiment.

Experimental Station

Our experimental method consists of photoelectron spectroscopy that utilizes

electron time-of-flight spectrometers (TOF) [35]. Two TOF spectrometers, as shown in Figure 4, are housed in a rotating chamber and are mounted in a plane perpendicular to the photon beam direction. The spectrometers are mounted with a relative spacing of 125.3° , each equidistant from the gas inlet valve. The spectrometers' apertures and gas inlet needle are each approximately 20 mm from the interaction region on the axis of the chamber. For the measurements described in this thesis, the TOF analyzers were fixed at 0° and 54.7° (magic angle) with respect to electric field vector of the incident radiation. This configuration, shown in Figure 4 allows for two spectra to be taken simultaneously at different angles. Electron of all kinetic energies are detected which allows measurements independent of the fluctuations of the target density or the photon flux. As a result, angular anisotropy can be measured and the β parameters can be extracted. The interior of the chamber is shielded with two layers of magnetic shielding which reduces the local fields, especially the earth's magnetic field, by a factor of two. The chamber is pumped with a turbo pump of 1000 l/s, which is capable of reducing the base pressure to 10^{-8} torr. The gas is passed into the interaction region through a needle to a pressure of about 3×10^{-5} torr. The whole chamber including analyzers, gas inlet, turbo pumps can be rotated around the synchrotron beam to allow measurement of spectra at different angles.

Figure 5 shows one of the analyzers. Electrons created in the source volume fly straight to the micro channel plates (MCPs) where they are detected. In order to measure the flight time of the electrons we have to use the light source in few bunch operation. The synchrotron ring has to operate in the timing mode where there are

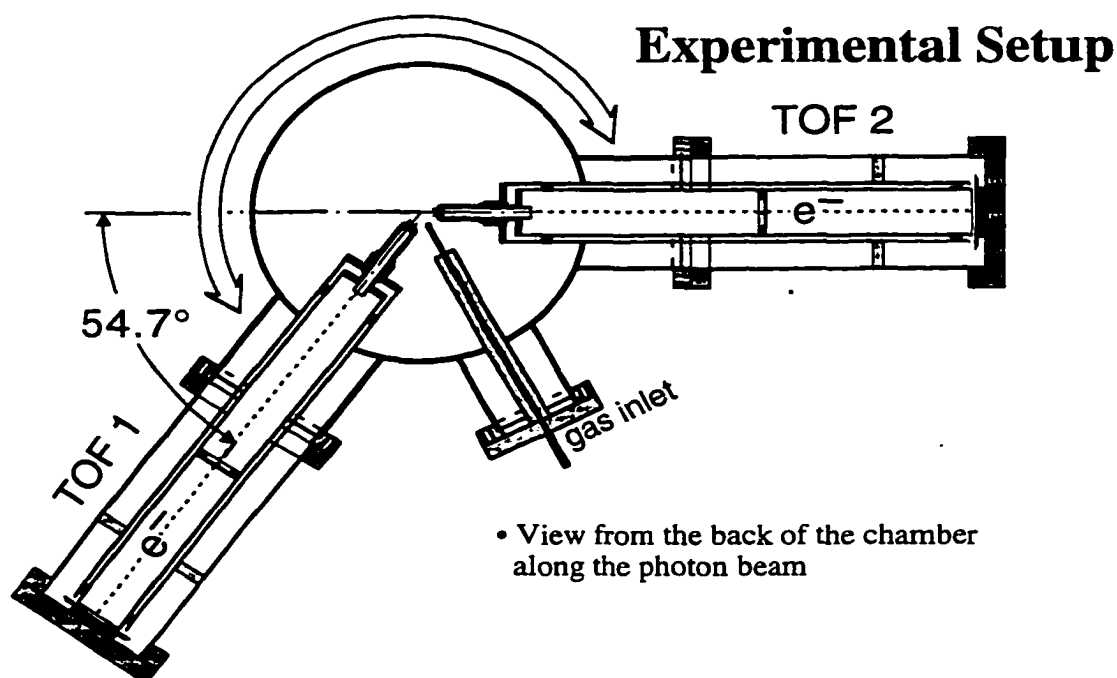


Figure 4. Schematic Diagram of the Experimental Setup Showing Two Time of Flight (TOF) Electron Spectrometers Mounted to a Rotatable Chamber. The incident synchrotron radiation goes through the interaction region, perpendicular with respect to the drawing plane.

only a few bunches of electrons in the ring. In all the experiments conducted in this thesis, we used double bunches with a timing difference of 328 ns between the bunches. Each TOF spectrometer consists of a pair of microchannel plates and a detection plate mounted at the end of a 689-mm flight path. By measuring the arrival times of the ejected electrons relative to the photon pulse, complete photoelectron spectra can be measured. The spectra are then converted from time to kinetic energy as described below. In order to improve the resolution of our spectra, a retarding potential was applied at the retarding cage and the inner nose. We applied different retarding potentials for different experiments, and our retarding potentials were -201 V, -30 V and -32 V for argon, krypton and xenon experiments respectively. To prevent

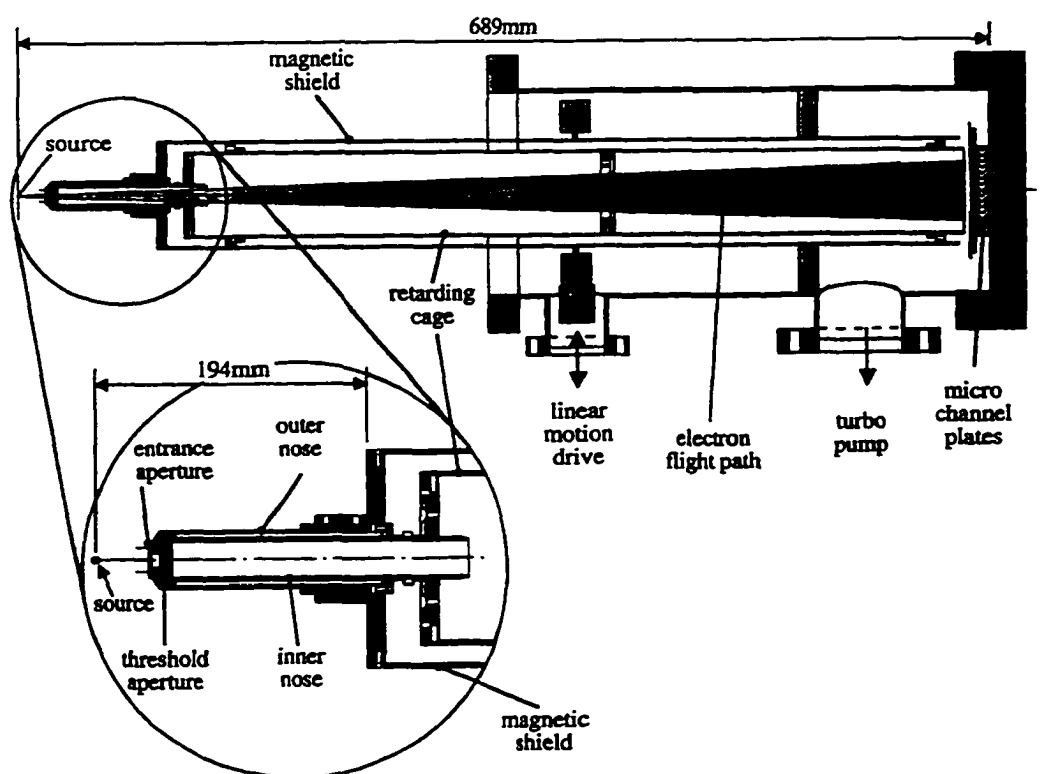


Figure 5. Time of Flight Electron Spectrometer With an Enlarged Part of its Entrance.

the slower electrons being affected by electric and magnetic stray field, we also used a magnetic shield in the drift tube of the analyzer. The time-to-energy conversion curve was obtained by using calibration spectra of the Ne 2s and 2p photoelectron lines of well-known binding energy. In order to obtain the relative detection efficiency of the two analyzers, the Ne calibration spectra are also used for all the photoelectrons and the constant ionic state spectra are corrected for the analyzers' transmission and detector's efficiency. Our spectrometer's resolution varied from one experiment to another. The spectrometer resolution was on average 90 meV in the case of the Ar $2p_{1/2,3/2}^{-1}ns,d$ resonant transition. This resolution changes to an average of 110 meV at the photon energies corresponding to Kr $3d_{3/2,5/2}^{-1}np \rightarrow 4s^{-1}4p^{-1}mp$ reso-

nant Auger transition. Finally an average spectrometer resolution of 46 meV was used for Xe $4d_{5/2}^{-1} \rightarrow 6p$ decay spectrum.

The Measuring Electronics

The electrons created in the source volume fly straight to the microchannel plate (MCP) where they are detected. When the electron hits the first MCP, it results in an avalanche that is amplified by the second MCP. The current amplification on one MCP which has a voltage of 2500 V, is of the order of $(1-5) \times 10^4$. A fast two step amplifier (AMP) amplifies the decoupled signal (50-100 times). Then, the signal is connected to a constant fraction discriminator (CFD). The MCP-pulses have strongly varying amplitudes but have similar shapes. A simple discriminator, which triggers at certain threshold level, would not give the needed time accuracy (<100 ps) because the trigger time would depend on the amplitude of the incoming pulse. The CFD technique operates as follow:

An incoming signal is split into two signals, one of the signals is attenuated by 0.2, and the other signal is not attenuated but delayed by 0.6ns. The attenuated and the delayed signals are then combined in a differential amplifier stage resulting in a subtraction process. The CFD attenuated incoming pulses and the delayed inverted pulses have constant amplitude ratios. The outgoing pulse starts when the combination signal goes through zero. The method works for pulses with similar shape independently of their amplitude. The signal from the CFD is sent to the start of the time-to-amplitude-converter (TAC). The stop signal of the TAC is provided by the bunch

marker signal from the synchrotron radiation ring. The basic time-to-amplitude-converter consists of an integrator, which operates by charging a capacitor with a constant current during the time interval from a start signal to a stop signal. The current linearly charges the capacitor, producing a ramp voltage. The charging process stops when the stop signal is received, the TAC discharges the pulse, whose height is proportional to the time between the starting and the stopping pulse. The analog pulse is then transformed by the analog to digital converter (ADC) which digitizes the pulse and sends it to the multichannel analyzer (MCA). The MCA then histograms the counts by arrival time. The resulting counts versus time spectrum is then stored and displayed on a PC using a labview data acquisition program. The labview acquisition program, in addition to recording spectra, monitors the synchrotron radiation's current and the chamber pressure.

Two-dimensional Photoelectron Spectrum

In the experiment conducted in Chapter V of this thesis, we added to our angle resolved method, an imaging technique to record the electron spectra of Kr near the 3d-ionization threshold. To produce a two-dimensional imaging (2D) electron emission data sets, a photon energy range of 6-eV-wide and a kinetic energy window covering the majority of the ejected electrons was chosen to allow the investigation of the Kr 3d ionization processes. This data was collected by setting the photon energy to the beginning of the range of interest and photoelectron spectra (PES) were accumulated simultaneously in each analyzer for 10 s. The photon energy was then incremen-

ted by 10 meV ($1/4 \times$ photon resolution) and another pair of PES was collected. By repeating this procedure over the photon energy range of interest, which takes a total of two and a half hours, we were able to produce comprehensive and detailed 2D images. This new method of looking at the data collected allows examination of all of the data in order to spot areas of interest and in order to follow the progression of various processes. It also allows experimental artifacts, such as peaks due to higher order or background electron, to be identified and removed from the two-dimensional 2D data wherever possible. Also, in this particular experiment, the 2D technique was used to observe the progression of the np Rydberg series $n = 5-11$ over a photon energy range of 6 eV.

CHAPTER IV

ANGLE-RESOLVED STUDY OF ARGON $2p_{1/2,3/2}^{-1} ns, d$ RESONANT AUGER DECAY

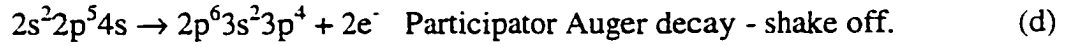
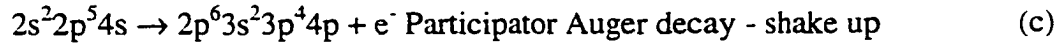
Abstract

Angle-resolved measurements of the Ar $2p_{1/2}^{-1} 4s, 3d, 4d$ and $2p_{3/2}^{-1} 4s, 3d, 4d$ resonant Auger transitions have been carried out using photons from an undulator beamline at the Advanced Light Source. The intensity distributions and angular distribution anisotropy β parameters have been reported for nearly all of the possible $3p^4 nl$ final ionic states. Our results further verify the predictions of the spectator model for the $2p_{1/2,3/2}^{-1} 4s$ resonances and the subsequent breakdown of this model for the $2p_{1/2,3/2}^{-1} 3d$ and $2p_{1/2,3/2}^{-1} 4d$ relative intensities. This is the first report of the resonant Auger β parameters of the $2p_{1/2,3/2}^{-1} 3d$ or $2p_{1/2,3/2}^{-1} 4d$ resonances and the intensity distribution for the $2p_{1/2}^{-1} 4d$ resonance. Our results have been compared with previous experimental and theoretical results wherever possible.

Introduction

After the excitation of an inner shell electron, an atom can relax nonradiatively through one of the following mechanisms, summarized here for the Ar $2p^{-1} 4s$ resonance:





The inner-shell excited states below the 2p thresholds in argon have been known for many years. Accurate measurements were performed by King et al. [4] using the electron energy-loss technique. The first resonant Auger spectra pertaining to the decay of these states were recorded by Aksela et al. [39]. In the previous non-angular-resolved studies of the intensity distributions it was reported that the decay of the Ar $2p^{-1}4s$ states can be described reasonably well by the spectator model, whereas the decay of the $2p^{-1}nd$ states is dominated by shake-up processes [39-45]. The angular distribution of the electrons emitted in a resonance Auger process has been measured by Carlson et al. [15], but their measurement suffered from poor resolution due to the use of broad photon sources. Also, measurements of the $2p^{-1}3d$ and $2p^{-1}4d$ resonances have been unobtainable due to insufficient photon resolution. Theoretically, the Auger decays of the $2p^{-1}4s$ resonances have been studied extensively by Cooper [19], Hergenhausen et al. [20] and Chen [21,22] as mentioned in detail in Chapter I.

The aim of the experiment presented in this chapter is to report measurements of the intensity distributions and angular distributions (β parameters) for the Auger decay spectra following the $2p \rightarrow 4s, 3d, 4d$ resonant excitations in argon. No prior measurements of the resonant Auger β parameters of the $2p^{-1}_{1/2,3/2}3d$ and $2p^{-1}_{1/2,3/2}4d$ resonances, or the intensity distribution for the $2p^{-1}_{1/2}4d$ resonance have been pub-

lished, to the best of our knowledge. We compared our results with previous experimental and theoretical results wherever possible.

Results and Discussion

In order to determine the photon energies necessary to excite the resonant transitions, a measurement of total electron yield versus photon energy was carried out and is shown in Figure 6.

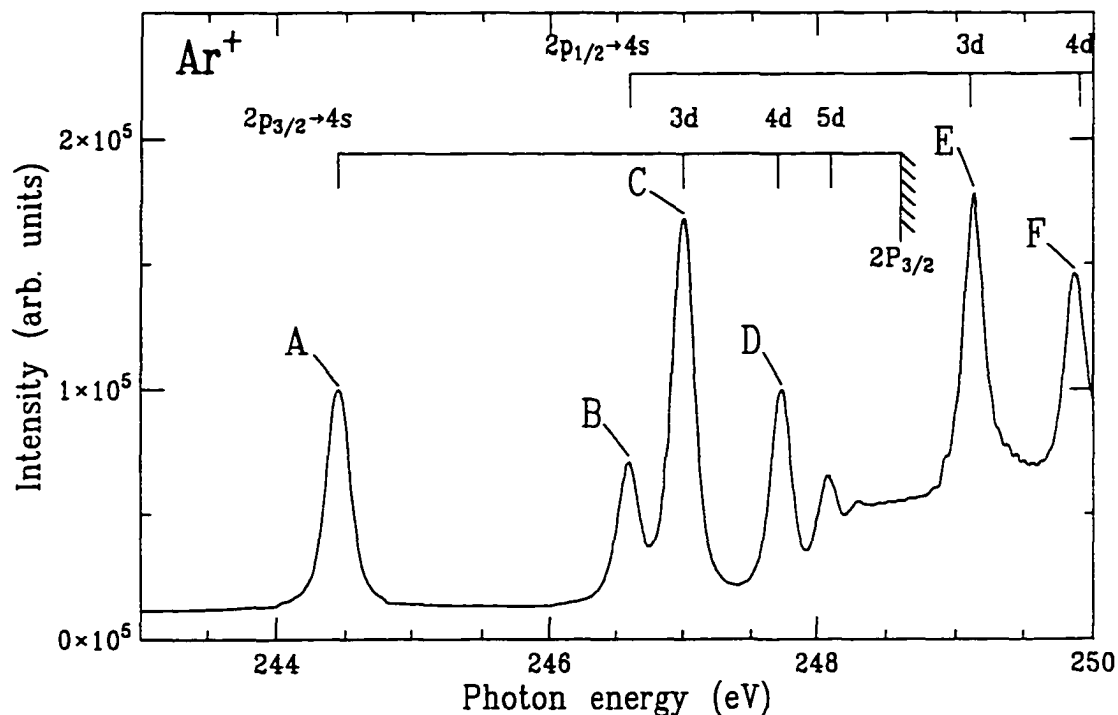


Figure 6. Photon Energy Scan over the Ar $2p^{-1}nl$ Resonances, Taken in the Ionization Threshold Region of the $2p_{3/2}$ (248.6 eV) and $2p_{1/2}$ (250.78 eV) Shells [4]. The resonant energies used in this chapter were taken from this scan. The resonances of interest are labeled A through F.

The resolution for this scan was 160 meV due to photon beam fluctuations. For all of our measurements, the absolute resonant energies have been taken from King et al.

[4]. Kinetic energy spectra were then measured with an average photon resolution of 107 meV and an average spectrometer resolution of 90 meV at the photon energies corresponding to the resonant transitions. These spectra are shown in Figure 7.

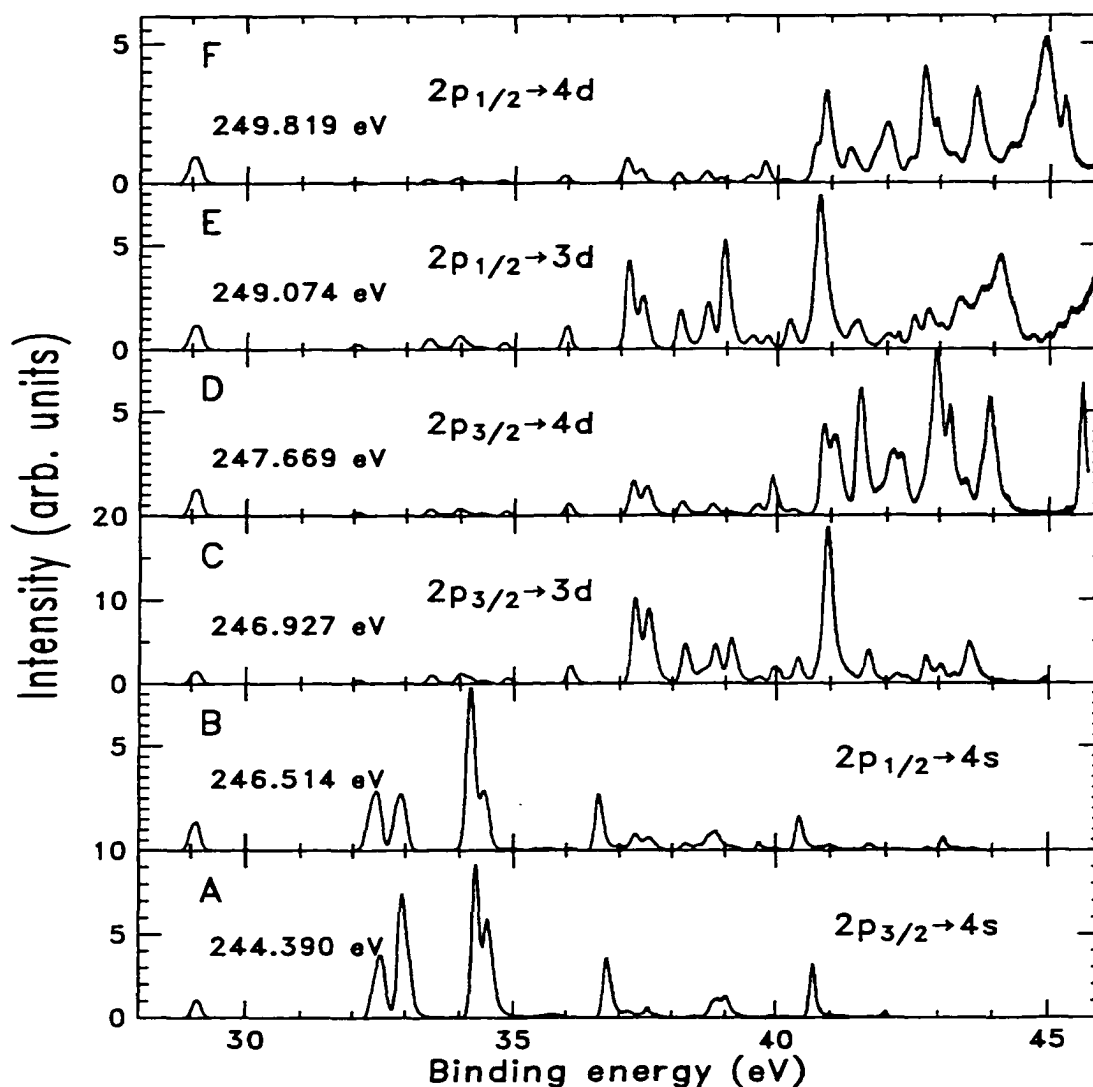


Figure 7. Complete Photoelectron Spectra for the $2p^{-1}4s$ Resonances (A, B), the $2p^{-1}3d$ Resonances (C, E), and the $2p^{-1}4d$ Resonances (D, F). For each case, the intensity distribution is shown at the magic angle ($\theta_m = 54.7^\circ$). The spectra were measured with a 201 V retarding potential applied to the flight tube. The absolute resonant energies have been given by King et al. [4].

For each spectrum, Gaussian curves were fit to each of the various final ionic states, with the relative binding energies of the final ionic states fixed with the spacing matched to the optical data of Minnhagen [46]. The linewidths of the peaks are broadened slightly with increased kinetic energy, which was consistent with the expected decrease in spectrometer resolution at higher kinetic energies (a trait inherent to TOF spectroscopy).

The $2p^{-1}4s$ Resonant Auger Spectra

A plot of the $2p_{3/2}^{-1}4s$ and $2p_{1/2}^{-1}4s$ spectra is shown in Figures 7-A, B (measured at the magic angle). A comparison of these resonant Auger spectra with normal non-resonant Auger spectra (e.g. Meyer et al. [41]) shows that, as predicted by the spectator model, the resonant Auger spectrum looks much like the normal Auger spectrum with only a slight energy shift (due to the screening effect of the spectator electron). This result supports the validity of the spectator model for predicting relative intensities.

Figures 8 and 9 depict portions of the $2p_{1/2}^{-1}4s$ and $2p_{3/2}^{-1}4s$ spectra, respectively. Each of the prominent features is labeled with a number, and each individual LS term is labeled in all figures and tables by a numbered letter. Here, the same binding energy region is viewed from two different angles (0° and 54.7° with respect to the synchrotron light's electric field). For each resolved final ionic state, a Gaussian peak has been fit, with the relative spacing between the peaks assigned using optical data of Minnhagen [46]. Once the data from each spectrometer has been norma-

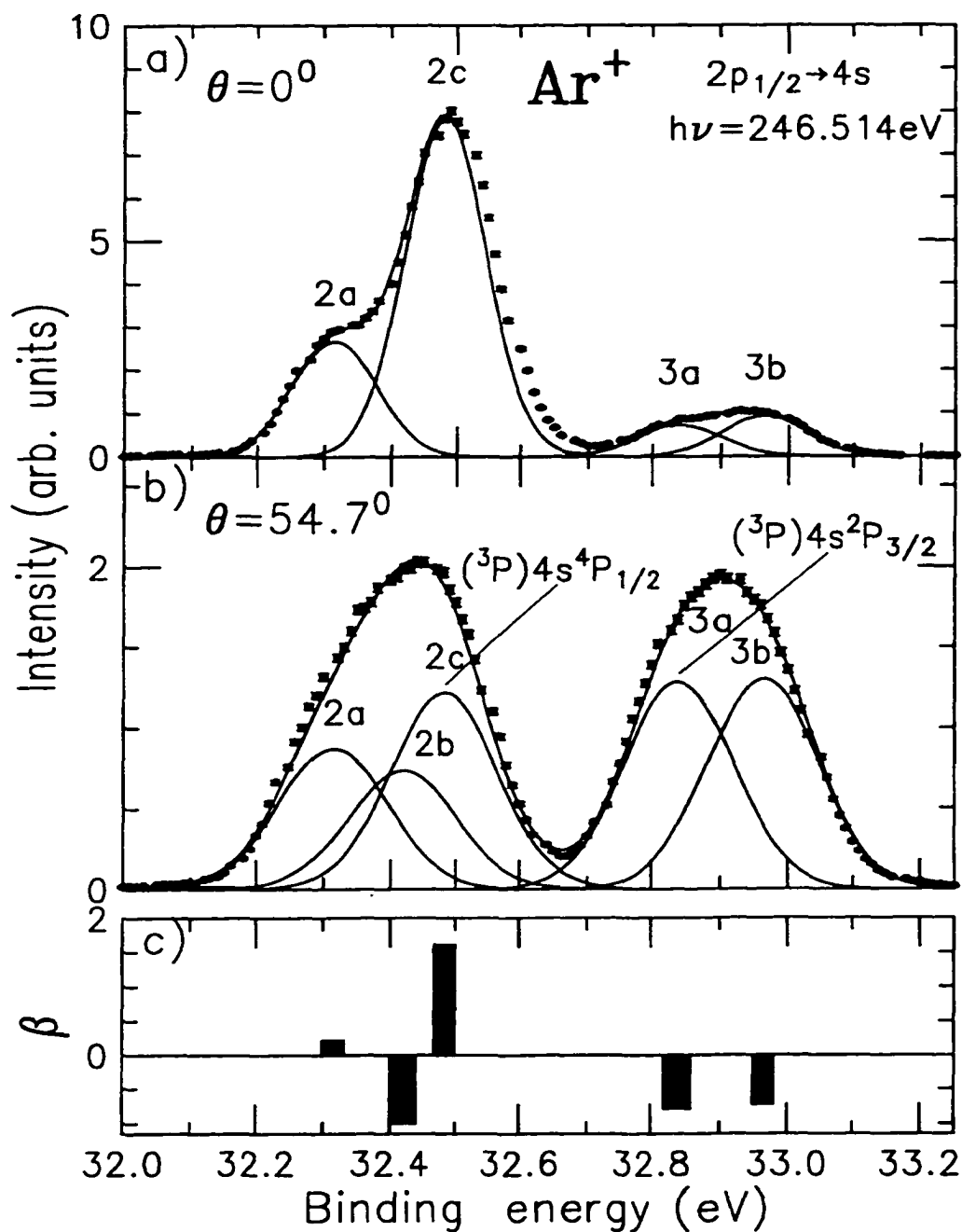


Figure 8. Auger Decay Spectra for Ar $2p_{1/2}^{-1}4s$ Resonance Shown at (a) $\theta = 0^\circ$ and (b) $\theta = 54.7^\circ$. The peak labels correspond to those states listed in Table 1. The angular distribution anisotropy parameters (β) for the $3p^4(^3P)4s^4P$ and $3p^4(^3P)4s^2P$ lines are shown in (c). These spectra were recorded with a 201 V retarding potential applied to the flight tube. The absolute resonant energies have been given by King et al. [4].

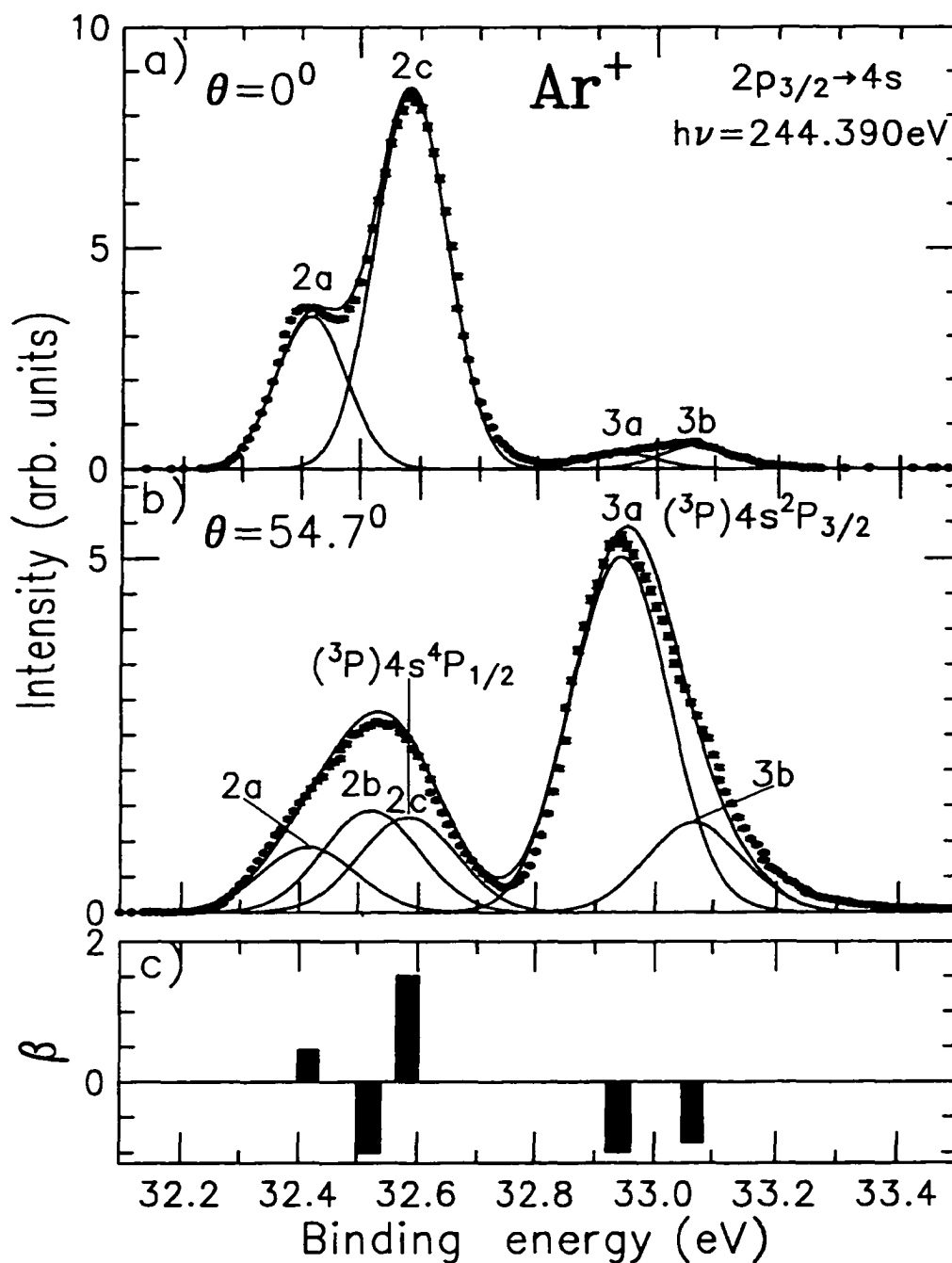


Figure 9. Auger Decay Spectra for Ar $2p_{3/2}^{-1}4s$ Resonance Shown at (a) $\theta = 0^\circ$ and (b) $\theta = 54.7^\circ$. The peak labels correspond to those states listed in Table 2. The β parameters for the $3p^4(^3P)4s^4P$ and $3p^4(^3P)4s^2P$ lines are shown in (c). These spectra were recorded with a 201 V retarding potential applied to the flight tube. The absolute resonant energies have been given by King et al. [4].

lized to the spectrometers' relative efficiency (to compensate for transmission differences between them), a comparison of the areas of a particular peak at the two angles allows the β parameter to be determined. These values are plotted in Figures 8-c and 9-c for the peaks in this region. It can be observed from Figures 8-b and 9-b (note the different scales) that the relative populations of the final ionic states (viewed at different angles) are significantly different, although the β parameter for each state is approximately the same. This illustrates rather well the requirement of the resolving power of this type of measurement. A complete listing of β parameters for nearly all $3p^4nl$ final ionic states is given in Table 1 for the $2p_{1/2}^{-1}4s$ decays and Table 2 for the $2p_{3/2}^{-1}4s$ decays. In order to compare our results with previously unresolved work, we have listed in all tables both the individual β components and their average β value (shown in boldface) which includes the sum of all overlapping peaks in a given LS term. For each value, the uncertainty is given in parentheses following the value. It should be noted that this uncertainty includes the statistical uncertainty added to a systematic uncertainty. The systematic uncertainty, which takes into account the sensitivity of the fit parameters, was found by performing a number of fits to a collection of overlapping peaks allowing for deviations in peak width and position. An error of 5% in the area was found for strong well-resolved peaks and an error of 10-20% was found for the weaker overlapping peaks. In every case the appropriate systematic error was added to the statistical error, and this total uncertainty is given in parentheses after the value in each table.

Table 1

Experimental and Theoretical Angular Distribution Anisotropy Parameters (β) for the Ar $2p_{1/2}^{-1}4s$ Resonance

Final State $3p^4nl$		β Parameters : $2p_{1/2} \rightarrow 4s$					
No	LS-term	β Experiment			β Theory		
		This work	Ref. [15]	Ref. [47]	Ref. [20]	Ref. [22]	
2a	$3p^4(^3P)4s^4P_{5/2}$	0.21(4)				0.19	
2b	$3p^4(^3P)4s^4P_{3/2}$	-1.00(5)				-0.81	
2c	$3p^4(^3P)4s^4P_{1/2}$	1.61(15)				1.8	
2a,b,c	$3p^4(^3P)4s^4P_{5/2,3/2,1/2}$	0.54(7)	0.1	0.56	0.69	-	0.62
3a	$3p^4(^3P)4s^2P_{3/2}$	-0.79(4)				-0.79	
3b	$3p^4(^3P)4s^2P_{1/2}$	-0.73(4)				-0.72	
3a,b	$3p^4(^3P)4s^2P_{3/2,1/2}$	-0.75(4)	-0.37	-0.57	-0.66	-	-0.75
2a,b,c	$3p^4(^3P)4s^4P_{5/2,3/2,1/2}$	-0.09(2)	-0.17	0.01	0.01	0.00	-0.007
3a,b	$3p^4(^3P)4s^2P_{3/2,1/2}$						
7a	$3p^4(^1D)4s^2D_{3/2}$	-1.00(5)					
7b	$3p^4(^1D)4s^2D_{5/2}$	0.05(3)					
8a	$3p^4(^3P)3d^2F_{7/2}$	α					
8b	$3p^4(^3P)3d^2F_{5/2}$	-0.52(3)					
9a	$3p^4(^3P)3d^2D_{3/2}$	-0.15(3)					
9b	$3p^4(^3P)3d^2D_{5/2}$	-0.04(2)					
7a,b	$3p^4(^1D)4s^2D_{5/2,3/2}$	-0.03(2)	-0.22	0.01	0.00	0.00	0.006
8a,b	$3p^4(^3P)3d^2F_{7/2,5/2}$						
9a,b	$3p^4(^3P)3d^2D_{5/2,3/2}$						
12a	$3p^4(^1S)4s^2S_{1/2}$	0.07(3)	-0.20	0.00	0.00	0.00	0.001

[47] Menzel using two different energies, 246.0 eV and 246.5 eV.

α . Strongly positive β .

It can be seen that most β parameters are negative or small positive, the former indicating a preferred emission in the direction perpendicular to the electric field vector of the radiation. This is due to the enhanced population of final ionic states which can be reached via parity unfavored transitions only through the resonant Auger processes [48]. For phototization, an incident photon of angular momentum j_γ ($j_\gamma = 1$)

is absorbed by an initial atomic state of total angular momentum J_0 , producing a photoelectron of orbital angular momentum l . The parity unfavored transitions occur when the angular momenta of the electron and photon couple in such a way that no angular component is transferred to the electron, which means that the momentum transferred between the atom and the ion j_t becomes equal to the electron momentum l . Thus, the angular distribution parameter β becomes automatically -1 because the momentum projection along the photon quantization axis is zero.

Table 2

Experimental and Theoretical Angular Distribution Anisotropy Parameters (β) for the Ar $2p_{3/2}^{-1}4s$ Resonance

Final State $3p^4nl$		β Parameters : $2p_{3/2} \rightarrow 4s$						
No	LS-term	This work	β Experiment			β Theory		
			Ref. [15]	Ref. [47]	Ref. [20]	Ref. [22]	Ref. [19]	
2a	$3p^4(^3P)4s^4P_{5/2}$	0.45(.06)					0.25	
2b	$3p^4(^3P)4s^4P_{3/2}$	-1.00(.05)					-0.88	
2c	$3p^4(^3P)4s^4P_{1/2}$	1.51(.13)					1.65	
2a,b,c	$3p^4(^3P)4s^4P_{5/2,3/2,1/2}$	0.32(.05)	0.37	0.30	0.53	0.34	0.88	
3a	$3p^4(^3P)4s^2P_{3/2}$	-1.00(.05)					-0.98	
3b	$3p^4(^3P)4s^2P_{1/2}$	-0.85(.05)					-0.87	
3a,b	$3p^4(^3P)4s^2P_{3/2,1/2}$	-0.94(.06)	-0.86	-0.93	-0.94	-0.95	-0.83	
2a,b,c	$3p^4(^3P)4s^4P_{5/2,3/2,1/2}$	-0.50(.03)	-0.65	-0.53	-0.47	-0.50	-0.47	
3a,b	$3p^4(^3P)4s^2P_{3/2,1/2}$							
7a	$3p^4(^1D)4s^2D_{3/2}$	0.66(.09)						
7b	$3p^4(^1D)4s^2D_{5/2}$	0.50(.06)						
8a	$3p^4(^3P)3d^2F_{7/2}$	*						
8b	$3p^4(^3P)3d^2F_{5/2}$	-0.35(.04)						
9a	$3p^4(^3P)3d^2D_{3/2}$	0.51(.06)						
9b	$3p^4(^3P)3d^2D_{5/2}$	0.55(.06)						
7a,b	$3p^4(^1D)4s^2D_{5/2,3/2}$	0.58(.07)	0.45	0.36	0.62	0.42	0.46	
8a,b	$3p^4(^3P)3d^2F_{7/2,5/2}$							
9a,b	$3p^4(^3P)3d^2D_{5/2,3/2}$							
12a	$3p^4(^1S)4s^2S_{1/2}$	0.93(.09)	0.66	0.39	1.09	1.00	0.98	1.00

* Large positive β value.

These results are compared with previous lower resolution measurements from Carlson et al. [15] and Menzel [47], and are compared with theoretical calculations of Cooper [19], Hergenhahn et al. [20], and Chen [22]. In his work Cooper [19] has treated the Auger decay as a single-step process while Hergenhahn et al. [20] have considered excitation and decay of the resonant state as a two-step process and predicted the resonant Auger decay based on the spectator model. Chen [22] used a multiconfiguration Dirac-Fock method in intermediate coupling with configuration interaction, also a two-step model. In general, our results differ considerably from those of Carlson et al. [15] and we attribute the discrepancy to the lack of resolution in the previous experiments. However, our results agree quite well with those of Menzel [47] who didn't resolve the individual components. When compared with calculations, we found fair agreement with Cooper's work [19] (Table 2), good agreement with Hergenhahn et al. [20] and very good agreement with Chen [22]. It should, therefore, be noted that the β parameters agree best with the Hergenhahn et al. and Chen calculations [20, 22]. Table 3 lists our relative intensities along with previous experimental (Carlson et al. [15], Menzel [47], and Meyer et al. [42]) and theoretical (Chen [22] and Meyer et al. [42,49]) results in the case of the $2p_{1/2}^{-1}4s$ resonance. Relative intensities for the $2p_{3/2}^{-1}4s$ resonance are displayed in Table 4 and are also compared to previous experimental (Carlson et al. [15], Menzel [47], and Meyer et al. [41,49]) and theoretical (Chen [22], Hergenhahn et al. [20], Cooper [19], and Meyer [49]) values. For both transitions, the relative intensities are taken with respect to the sum of the areas of the $(^3P)4s(^4P)$ peaks since these lines were well separated and did not overlap with other states. The uncertainty for each relative intensity

has been displayed in parentheses following the value. The method used to calculate these uncertainties is described above for the $2p^{-1}4s$ β parameters. In this work, we have been able to resolve many more final ionic states than has been done previously. One can also note that the spectator model [20] agrees relatively well with the measured β parameters.

Table 3

Experimental and Theoretical Relative Intensities for the Ar $2p_{1/2}^{-1}4s$ Resonance
(Measured at the Magic Angle)

No	Final State $3p^4nl$ LS-term	Relative Intensities : $2p_{1/2} \rightarrow 4s$						
		<i>I</i> (θ) Experiment			<i>I</i> (θ) Theory			
		This work	Ref. [15]	Ref. [47]	Ref. [41]	Ref. [22]	Ref. [41,49]	
2a	$3p^4(^3P)4s^4P_{5/2}$	16.1(2.0)					20	
2b	$3p^4(^3P)4s^4P_{3/2}$	13.6(1.9)					12	
2c	$3p^4(^3P)4s^4P_{1/2}$	22.5(1.6)					22	
2a,b,c	$3p^4(^3P)4s^4P_{5/2,3/2,1/2}$	52.2(3.4)	42	51	51	50	54	54 55
3a	$3p^4(^3P)4s^2P_{3/2}$	23.6(1.5)					23	
3b	$3p^4(^3P)4s^2P_{1/2}$	24.2(1.5)					23	
3a,b	$3p^4(^3P)4s^2P_{3/2,1/2}$	47.8(2.8)	58	49	49	50	46	46 45
2a,b,c	$3p^4(^3P)4s^4P_{5/2,3/2,1/2}$	100.0	100	100	100	100	100	100
3a,b	$3p^4(^3P)4s^2P_{3/2,1/2}$							
7a	$3p^4(^1D)4s^2D_{3/2}$	19.2(1.7)						
7b	$3p^4(^1D)4s^2D_{5/2}$	69.7(4.3)						
8a	$3p^4(^3P)3d^2F_{7/2}$	0.9(*)						
8b	$3p^4(^3P)3d^2F_{5/2}$	15.3(2.0)						
9a	$3p^4(^3P)3d^2D_{3/2}$	10.1(1.6)						
9b	$3p^4(^3P)3d^2D_{5/2}$	20.3(1.4)						
7a,b	$3p^4(^1D)4s^2D_{5/2,3/2}$	135.5(8.6)	95	128	130	139	81	93 50
8a,b	$3p^4(^3P)3d^2F_{7/2,5/2}$							
9a,b	$3p^4(^3P)3d^2D_{5/2,3/2}$							
12a	$3p^4(^1S)4s^2S_{1/2}$	31.0(1.8)				24	29	24 23

* Approximately = 1.

It should be noticed from Tables 1 and 2 that, as predicted by the spectator model, the combined anisotropy of the 2P and 4P transitions is very close to zero in the case of the $2p_{1/2}^{-1}4s$ resonance and to -0.5 in the case of the $2p_{3/2}^{-1}4s$ resonance. The spectator model, however, demonstrates rather poor agreement with the measured relative intensities when compared to Chen's model [22], which seems to perform better on both fronts.

Table 4

Experimental and Theoretical Relative Intensities for the Ar $2p_{3/2}^{-1}4s$ Resonance
(Measured at the Magic Angle)

Final State $3p^4nl$		Relative Intensities : $2p_{3/2}^{-1} \rightarrow 4s$								
No	LS-term	This work	$I(\theta)$ Experiment				$I(\theta)$ Theory			
			Ref. [15]	Ref. [47]	Ref. [42]	Ref. [22]	Ref. [20]	Ref. [19]	Ref. [41,49]	
2a	$3p^4(^3P)4s^2P_{5/2}$	9.2(1.1)				12				
2b	$3p^4(^3P)4s^2P_{3/2}$	14.3(1.8)				12				
2c	$3p^4(^3P)4s^2P_{1/2}$	13.4(1.6)				13				
2a,b,c	$3p^4(^3P)4s^2P_{5/2,3/2,1/2}$	36.9(2.3)	17	38	31	37	30	38	36 36	
3a	$3p^4(^3P)4s^2P_{3/2}$	50.4(2.8)				48				
3b	$3p^4(^3P)4s^2P_{1/2}$	12.7(1.6)				15				
3a,b	$3p^4(^3P)4s^2P_{3/2,1/2}$	63.1(3.5)	83	62	69	63	70	62	64 64	
2a,b,c	$3p^4(^3P)4s^2P_{5/2,3/2,1/2}$	100.0	100	100	100	100	100	100	100	
3a,b										
7a	$3p^4(^1D)4s^2D_{3/2}$	5.4(1.6)								
7b	$3p^4(^1D)4s^2D_{5/2}$	46.4(2.6)								
8a	$3p^4(^3P)3d^2F_{7/2}$	0.5(*)								
8b	$3p^4(^3P)3d^2F_{5/2}$	13.2(1.7)								
9a	$3p^4(^3P)3d^2D_{3/2}$	20.3(1.3)								
9b	$3p^4(^3P)3d^2D_{5/2}$	10.7(1.4)								
7a,b	$3p^4(^1D)4s^2D_{5/2,3/2}$	96.5(5.6)	86	119	108	110	75	75	78	80 46
8a,b										
9a,b										
12a	$3p^4(^1S)4s^2S_{1/2}$	21.0(1.2)	31 33	29	29	16	19	19	20 18	

* Very weak line with large uncertainty.

One possible explanation may be that Chen's model [22] calculates the full state vector and takes into account the mixing of all the states, which is important in the determination of the intensities. The spectator model instead uses a simple assumption [20] in relating the resonant and non-resonant spectra. This deficiency, however, does not affect the calculated β values significantly because β is a relative quantity describing the character of a certain transition independent of its strength. The spectator model describes the β values in terms of the most simple geometric coupling situation yielding good values for the sum of the multiplet components, whereas the refined calculations of Chen [22] give also the correct relative intensities of the different multiplets with respect to each other, and even good values for the individual multiplet components with respect to both β and relative intensities. The spectator model allows a good first approximation of the β parameters for the $2p^{-1}4s$ resonance and gives a simple physical explanation for the differences in the angular distribution of resonant and non-resonant Auger electrons.

The $2p^{-1}3d$ Resonant Auger Spectra

The complete $2p_{3/2}^{-1}3d$ and $2p_{1/2}^{-1}3d$ spectra are given in Figures 7-C, E (measured at the magic angle). Contrary to the $2p^{-1}4s$ case described above, this resonant transition does not obey the predicted behavior of the spectator model, i.e. the observed spectra are much different from the normal non-resonant Auger spectra [41]. Instead, the spectra are dominated by shake-up processes. Reasons for this have been discussed by Aksela et al. [39] and Mursu et al. [50], who have demon-

strated the importance of the shake up process arising from collapse of the 3d wave function in the initially excited $2p^{-1}3d$ state, as compared to the final ionic state. Another explanation has been provided by Meyer et al. [41], who have described, in some detail, the special properties of the wave function, which leads to a high shake-up probability.

Figures 10 and 11 show smaller portions of the resonant Auger spectra of the $2p_{1/2}^{-1}3d$ and $2p_{3/2}^{-1}3d$ excitations, respectively. These figures demonstrate the large overlap of peaks, which made the identification of individual final ionic states difficult. If a peak is not well resolved the fit parameters will have a larger uncertainty, which will ultimately propagate to a larger uncertainty in the β parameters. A complete list of relative intensities and β parameters is given in Tables 5 and 6, and a comparison to experimental relative intensities of Mursu et al. [50] has been made. In these tables, the uncertainties for the relative intensities and β parameters are given in parentheses following the values. Again, these uncertainties include both systematic and statistical errors, and have been calculated as described above for the $2p^{-1}4s$ β parameters. For these transitions, the relative intensities have been normalized with respect to the area of the (1D) $3d(^2F_{3/2,7/2})$ state. Mursu et al. [50] originally presented their relative intensities with respect to the total intensity at each photon energy, and their data have been converted to match our normalization in order to facilitate the comparison. The discrepancies between our results and those of Mursu et al. [50] for the relative intensities in the closely spaced peaks can be explained by the difficulty in resolving the overlapping peaks in both sets of data, as mentioned above. Hence,

the relative intensities of neighboring peaks must be considered as estimates only. In all cases, all overlapping individual j -levels (e.g. $3d^4D_{7/2,5/2,3/2,1/2}$) within an LS term ($3d^4D$) were combined under the LS term, and this value is shown in bold type. A comparison of each complete LS term shows overall good agreement with the previous data.

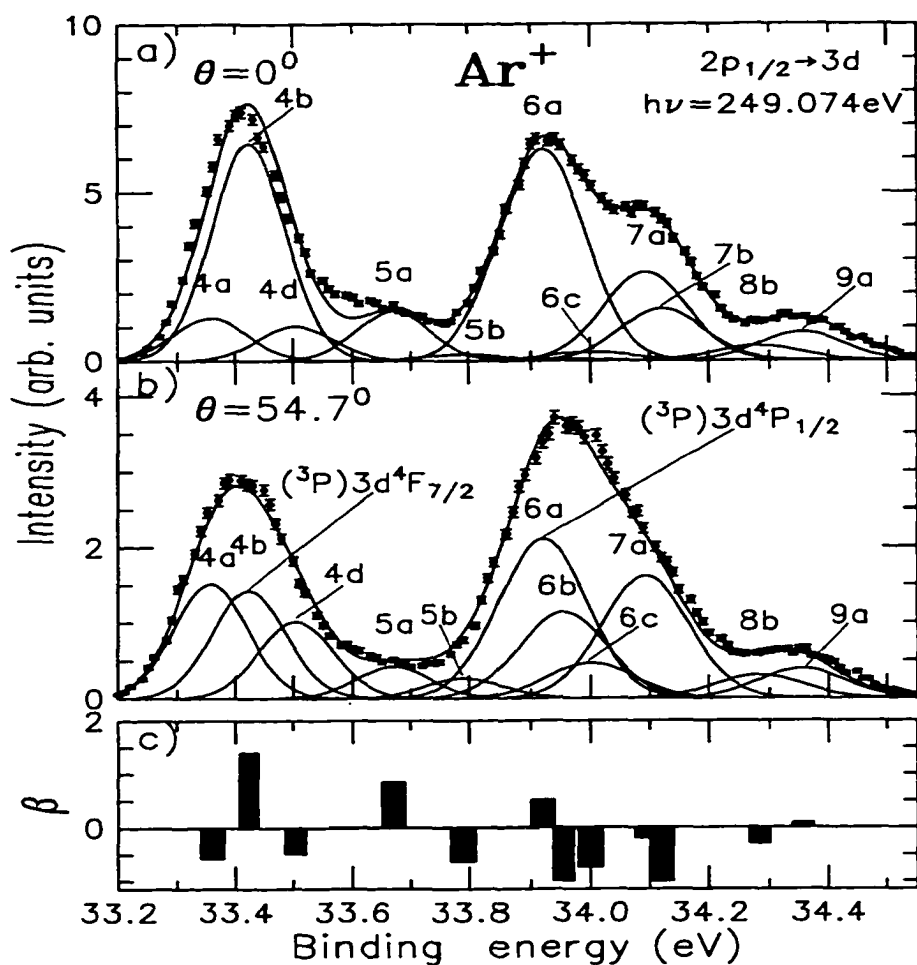


Figure 10. Auger Decay Spectra for Ar $2p_{1/2}^{-1}3d$ Resonance Shown at (a) $\theta = 0^\circ$ and (b) $\theta = 54.7^\circ$. The peak labels correspond to those states listed in Table 5. The β parameters for the $3p^4(^3P)3d^4F$, $3p^4(^3P)3d^2P$, $3p^4(^3P)3d^4P$, $3p^4(^1D)4s^2D$, $3p^4(^3P)3d^2F$, and $3p^4(^3P)3d^2D$ lines are shown in (c). These spectra were recorded with a 201 V retarding potential applied to the flight tube. The absolute resonant energies have been given by King et al. [4]

Our β parameter values for the $2p^{-1}3d$ resonances are, to our knowledge, the first reported experimental or theoretical results. As seen in the $2p^{-1}4s$ resonance above, nearly all states demonstrate negative or small positive β parameters.

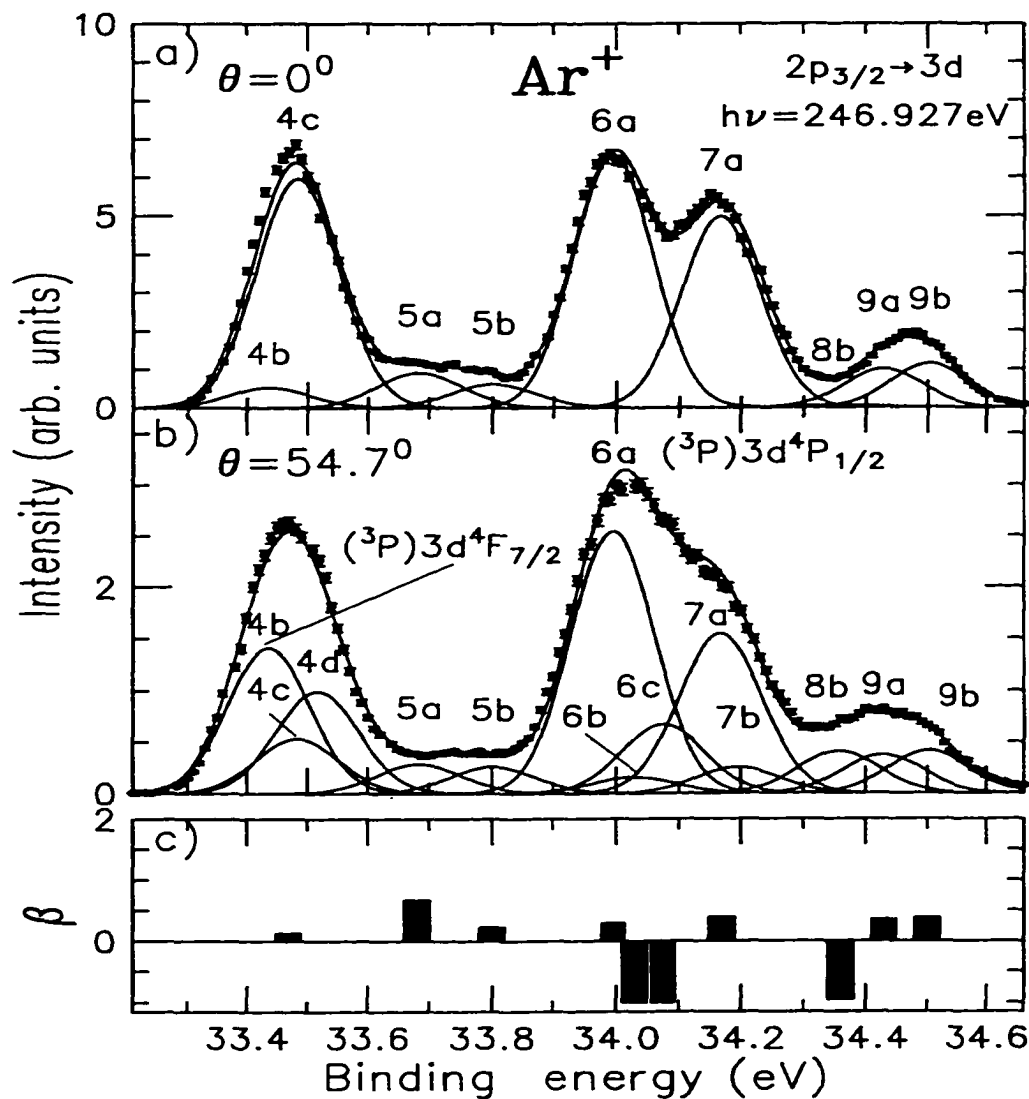


Figure 11. Auger Decay Spectra for Ar $2p_{3/2}^{-1}3d$ Resonance Shown at (a) $\theta = 0^\circ$ and (b) $\theta = 54.7^\circ$. The peak labels correspond to those states listed in Table 6. The β parameters for the $3p^4(^3P)3d^4F$, $3p^4(^3P)3d^2P$, $3p^4(^3P)3d^4P$, $3p^4(^1D)4s^2D$, $3p^4(^3P)3d^2F$, and $3p^4(^3P)3d^2D$ lines are shown in (c). These spectra were recorded with a 201 V retarding potential applied to the flight tube. The absolute resonant energies have been given by King et al. [4].

Table 5

Experimental Relative Intensities (Measured at the Magic Angle) and β Parameters
for the Ar $2p_{1/2}^{-1}3d$ Resonance

No	Final State $3p^4nl$ LS-term	Relative Intensity : $2p_{1/2} \rightarrow 3d$		β Parameters :
		I (θ) This work	I (θ) ^a	β This work
1a	$3p^4(^3P)3d^4D_{7/2}$	25.2(1.7)	15.2	-0.10(2)
1b	$3p^4(^3P)3d^4D_{5/2}$	0.1(*)	2.9	α
1c	$3p^4(^3P)3d^4D_{3/2}$	-	2.5	-
1d	$3p^4(^3P)3d^4D_{1/2}$	1.3(0.7)	11.5	δ
1a,b,c,d	$3p^4(^3P)3d^4D_{7/2,5/2,3/2,1/2}$	26.6(2.5)	32.1	0.03(3)
2a	$3p^4(^3P)4s^4P_{5/2}$	2.2(0.8)	3.3	0.48(8)
2b	$3p^4(^3P)4s^4P_{3/2}$	2.4(0.7)	9.5	-0.70(8)
2c	$3p^4(^3P)4s^4P_{1/2}$	0.1(0.4)	-	γ
2a,b,c	$3p^4(^3P)4s^4P_{5/2,3/2,1/2}$	4.7(1.5)	12.8	0.47(8)
4a	$3p^4(^3P)3d^4F_{9/2}$	21.3(1.5)	-	-0.57(3)
4b	$3p^4(^3P)3d^4F_{7/2}$	20.0(1.8)	-	1.39(13)
4c	$3p^4(^3P)3d^4F_{5/2}$	-	38.3	-
4d	$3p^4(^3P)3d^4F_{3/2}$	14.2(1.9)	27.6	-0.48(3)
4a,b,c,d	$3p^4(^3P)3d^4F_{9/2,7/2,5/2,3/2}$	55.5(3.8)	65.9	0.11(4)
5a	$3p^4(^3P)3d^2P_{1/2}$	5.9(1.6)	4.1	0.84(13)
5b	$3p^4(^3P)3d^2P_{3/2}$	3.7(1.1)	6.6	-0.63(7)
5a,b	$3p^4(^3P)3d^2P_{3/2,1/2}$	9.6(1.5)	10.7	0.29(4)
6a	$3p^4(^3P)3d^4P_{1/2}$	34.0(2.4)	15.6	0.51(6)
6b	$3p^4(^3P)3d^4P_{3/2}$	18.3(1.5)	54.3	-1.00(5)
6c	$3p^4(^3P)3d^4P_{5/2}$	7.5(2.1)	-	-0.74(8)
6a,b,c	$3p^4(^3P)3d^4P_{5/2,3/2,1/2}$	59.8(4.0)	69.9	-0.07(2)
7a	$3p^4(^1D)4s^2D_{3/2}$	26.0(2.0)	33.7	-0.19(3)
7b	$3p^4(^1D)4s^2D_{5/2}$	0.1(0.1)	-	-1.00(10)
7a,b	$3p^4(^1D)4s^2D_{5/2,3/2}$	26.0(2.0)	33.7	0.28(4)
8a	$3p^4(^3P)3d^2F_{7/2}$	-	-	-
8b	$3p^4(^3P)3d^2F_{5/2}$	4.9(1.4)	-	-0.3(5)
8a,b	$3p^4(^3P)3d^2F_{7/2,5/2}$	4.9(1.4)	-	-0.3(5)
9a	$3p^4(^3P)3d^2D_{3/2}$	6.2(1.7)	9.5	0.09(3)
9b	$3p^4(^3P)3d^2D_{5/2}$	0.3(0.3)	9.1	λ
9a,b	$3p^4(^3P)3d^2D_{5/2,3/2}$	6.5(1.9)	18.6	0.44(8)
10a	$3p^4(^1D)3d^2G_{9/2}$	17.1(2.2)	42.8	-1.00(5)
10b	$3p^4(^1D)3d^2G_{7/2}$	12.5(1.7)	-	μ
10a,b	$3p^4(^1D)3d^2G_{9/2,7/2}$	29.6(2.1)	42.8	0.36(5)
11a	$3p^4(^1D)3d^2F_{5/2}$	71.5 (4.2)	100.0	-0.25(3)
11b	$3p^4(^1D)3d^2F_{7/2}$	28.5(2.5)	-	0.11(3)
11a,b	$3p^4(^1D)3d^2F_{7/2,5/2}$	100.0	100.0	-0.18(3)
13a	$3p^4(^1D)3d^2D_{5/2}$	254.0(13.0)	284.0	0.17(4)
13b	$3p^4(^1D)3d^2D_{3/2}$	150.0(8.7)	124.0	-0.22(3)
13a,b	$3p^4(^1D)3d^2D_{5/2,3/2}$	404.0(22.0)	408.0	0.05(2)
14a	$3p^4(^1D)3d^2P_{3/2}$	124.0(7.1)	152.0	-1.00(5)
14b	$3p^4(^1D)3d^2P_{1/2}$	117.0(6.6)	81.0	0.01(2)
14a,b	$3p^4(^1D)3d^2P_{3/2,1/2}$	241.0(13.0)	233.0	-0.49(3)
15a	$3p^4(^1S)3d^2D_{5/2}$	2.7(1.4)	14.0	ν

Table 5-Continued

15b	$3p^4(^1S)3d^2D_{3/2}$	161.0(8.9)	151.0	-0.39(4)
15a,b	$3p^4(^1S)3d^2D_{5/2,3/2}$	163.7(9.5)	165.0	-0.33(3)
19	$3p^4(^1D)3d^2S_{1/2}$	148.0(8.2)	138.0	0.84(9)

a. According to Mursu et. al. [50].

α , δ , γ , λ , μ , and ν are strongly positive β .

*. Very weak line having large uncertainty.

Table 6

Experimental Relative Intensities (Measured at the Magic Angle) and β Parameters for the Ar $2p_{3/2}^{-1}3d$ Resonance

No	Final State $3p^4nl$ LS-term	Relative Intensity : $2p_{3/2} \rightarrow 3d$		β Parameters :
		I (θ) This work	I(θ) ^a	$2p_{3/2} \rightarrow 3d$ β This work
1a	$3p^4(^3P)3d^4D_{7/2}$	5.4(1.7)	9.6	-1.00(10)
1b	$3p^4(^3P)3d^4D_{5/2}$	7.1(1.8)	5.7	0.67(7)
1c	$3p^4(^3P)3d^4D_{3/2}$	12.2(1.6)	3.9	-0.38(3)
1d	$3p^4(^3P)3d^4D_{1/2}$	-	12.2	-
1a,b,c,d	$3p^4(^3P)3d^4D_{7/2,5/2,3/2,1/2}$	24.7(2.0)	31.4	-0.16(3)
2a	$3p^4(^3P)4s^4P_{5/2}$	-	-	-
2b	$3p^4(^3P)4s^4P_{3/2}$	5.1(1.3)	3.5	-1.00(10)
2c	$3p^4(^3P)4s^4P_{1/2}$	0.7(0.5)	7.3	2.00(20)
2a,b,c	$3p^4(^3P)4s^4P_{5/2,3/2,1/2}$	5.8(1.7)	10.8	-0.12(3)
4a	$3p^4(^3P)3d^4F_{9/2}$	-	-	-
4b	$3p^4(^3P)3d^4F_{7/2}$	25.8(1.8)	-	-0.82(5)
4c	$3p^4(^3P)3d^4F_{5/2}$	9.8(2.3)	41.7	α
4d	$3p^4(^3P)3d^4F_{3/2}$	18.2(2.3)	23.5	-1.00(5)
4a,b,c,d	$3p^4(^3P)3d^4F_{9/2,7/2,5/2,3/2}$	53.8(4.2)	65.2	0.07(1)
5a	$3p^4(^3P)3d^2P_{1/2}$	5.2(1.4)	-	0.67(9)
5b	$3p^4(^3P)3d^2P_{3/2}$	4.8(1.3)	7.8	0.23(5)
5a,b	$3p^4(^3P)3d^2P_{3/2,1/2}$	10.0(1.5)	7.8	0.43(6)
6a	$3p^4(^3P)3d^4P_{1/2}$	45.3(2.9)	30.4	0.29(4)
6b	$3p^4(^3P)3d^4P_{3/2}$	2.8(1.5)	32.6	-1.00(10)
6c	$3p^4(^3P)3d^4P_{5/2}$	11.9(1.9)	-	-1.00(5)
6a,b,c	$3p^4(^3P)3d^4P_{5/2,3/2,1/2}$	60.0(4.4)	63.0	-0.03(2)
7a	$3p^4(^1D)4s^2D_{3/2}$	27.5(1.9)	39.1	0.62(9)
7b	$3p^4(^1D)4s^2D_{5/2}$	4.5(1.8)	-	-1.00(10)
7a,b	$3p^4(^1D)4s^2D_{5/2,3/2}$	32.0(2.6)	39.1	0.39(6)
8a	$3p^4(^3P)3d^2F_{7/2}$	-	-	-
8b	$3p^4(^3P)3d^2F_{5/2}$	7.2(1.8)	-	-0.95(10)
8a,b	$3p^4(^3P)3d^2F_{7/2,5/2}$	7.2(1.8)	-	-0.54(7)
9a	$3p^4(^3P)3d^2D_{3/2}$	6.6(1.9)	12.6	0.35(6)
9b	$3p^4(^3P)3d^2D_{5/2}$	7.4(1.8)	10.43	0.38(7)
9a,b	$3p^4(^3P)3d^2D_{5/2,3/2}$	14.0(2.1)	23.03	0.37(5)
10a	$3p^4(^1D)3d^2G_{9/2}$	31.4(2.0)	43.5	-0.10(2)
10b	$3p^4(^1D)3d^2G_{7/2}$	-	-	-
10a,b	$3p^4(^1D)3d^2G_{9/2,7/2}$	45.4(2.8)	66.53	0.24(4)
11a	$3p^4(^1D)3d^2F_{5/2}$	25.1(1.8)	100.0	0.31(4)

Table 6-Continued

11b	$3p^4(^1D)3d^2F_{7/2}$	74.9(4.3)	-	-0.29(3)
11a,b	$3p^4(^1D)3d^2F_{7/2,5/2}$	100.0	100.0	-0.14(3)
13a	$3p^4(^1D)3d^2D_{5/2}$	294.1(16.0)	260.0	0.26(4)
13b	$3p^4(^1D)3d^2D_{3/2}$	225.6(13.0)	285.0	0.13(4)
13a,b	$3p^4(^1D)3d^2D_{5/2,3/2}$	519.7(28.0)	545.0	0.20(4)
14a	$3p^4(^1D)3d^2P_{3/2}$	242.4(13.0)	220.0	-0.98(6)
14b	$3p^4(^1D)3d^2P_{1/2}$	191.7(11.0)	185.0	-0.64(4)
14a,b	$3p^4(^1D)3d^2P_{3/2,1/2}$	434.1(23.0)	405.0	-0.83(5)
15a	$3p^4(^1S)3d^2D_{5/2}$	127.8(7.2)	168.0	-0.01(2)
15b	$3p^4(^1S)3d^2D_{3/2}$	98.8(6.0)	74.0	-0.01(2)
15a,b	$3p^4(^1S)3d^2D_{5/2,3/2}$	226.6(13.0)	242.0	-0.01(2)
19	$3p^4(^1D)3d^2S_{1/2}$	168.0(9.2)	146.0	0.16(4)

a. According to Mursu et al. [50].

α . Strongly positive β .

The $2p^{-1}4d$ Resonant Auger Spectra

The complete photoelectron spectra for the $2p^{-1}4d$ resonances, measured at the magic angle, are shown in Figures 7-D,F. As discussed above for the $2p^{-1}3d$ resonances, the $2p^{-1}4d$ resonances likewise demonstrate a breakdown of the spectator model in predicting relative intensities due to strong shake up modifications as has been proposed by Aksela et al. [39] and Mursu et al. [50].

Figures 12 and 13 show portions of the $2p_{1/2}^{-1}4d$ and $2p_{3/2}^{-1}4d$ spectra where the extracted β parameters for the peaks are displayed in Figures 12-c and 13-c. The dominance of negative β parameters, corresponding to preferred electron emission perpendicular to the electric field, can also be seen for this resonance. This supports Cooper's theory [19] which was only applied to the case of the $2p^{-1}4s$ resonances, but which seems to be also valid for the $2p^{-1}3d$ and $2p^{-1}4d$ resonances. The similarity of β values at the two different spin-orbit resonances is again demonstrated here.

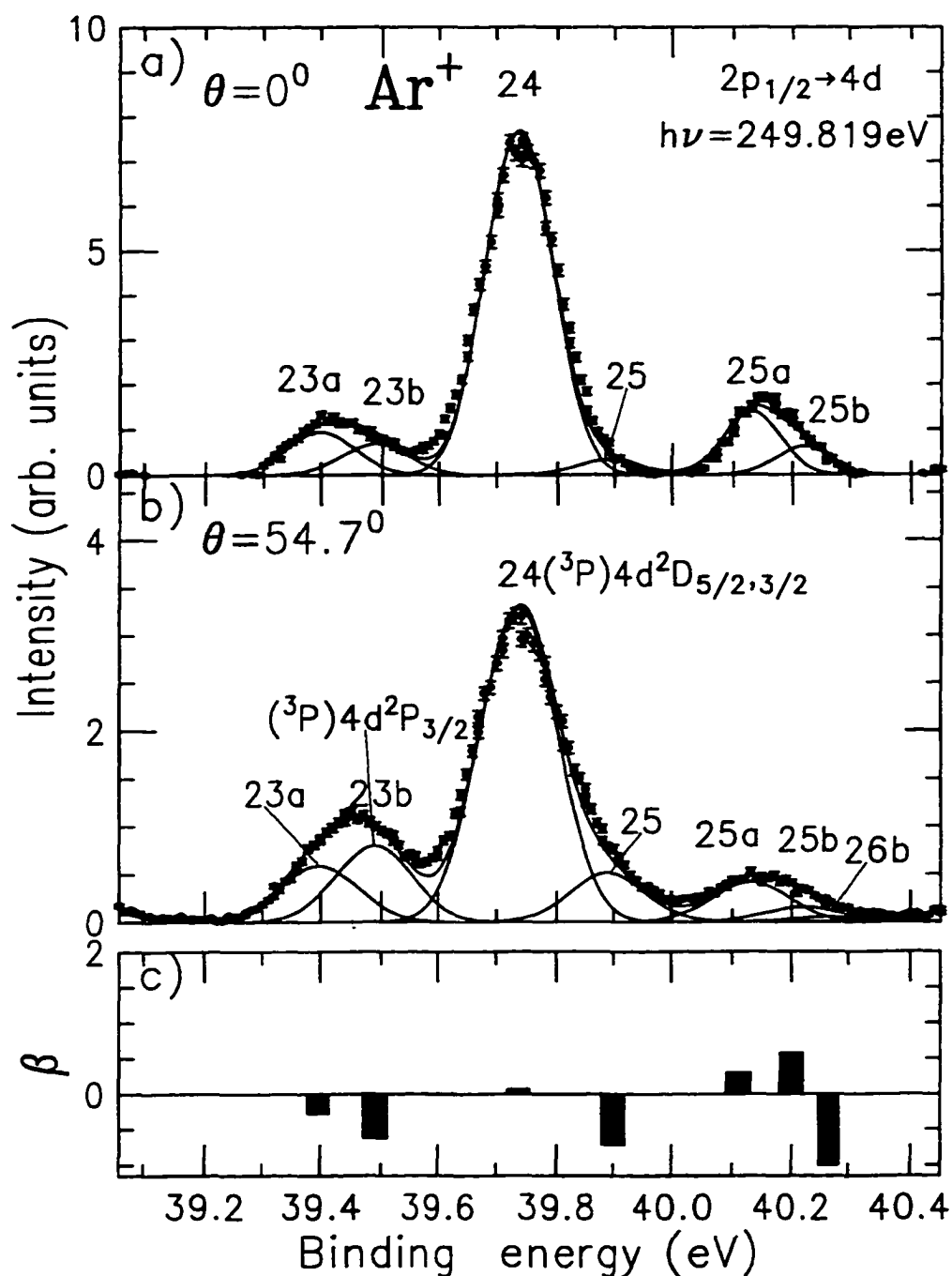


Figure 12. Auger Decay Spectra for Ar $2p_{1/2}^{-1}4d$ Resonance Shown at (a) $\theta = 0^\circ$ and (b) $\theta = 54.7^\circ$. The peak labels correspond to those states listed in Table 7. The β parameters for the $3p^4(^3P)4d^2P$, $3p^4(^3P)4d^2D$, $3p^4(^1D)4d^2G$ and $3p^4(^3P)6s^4P$ lines are shown in (c). These spectra were recorded with a 201 V retarding potential applied to the flight tube. The absolute resonant energies have been given by King et. al. [4].

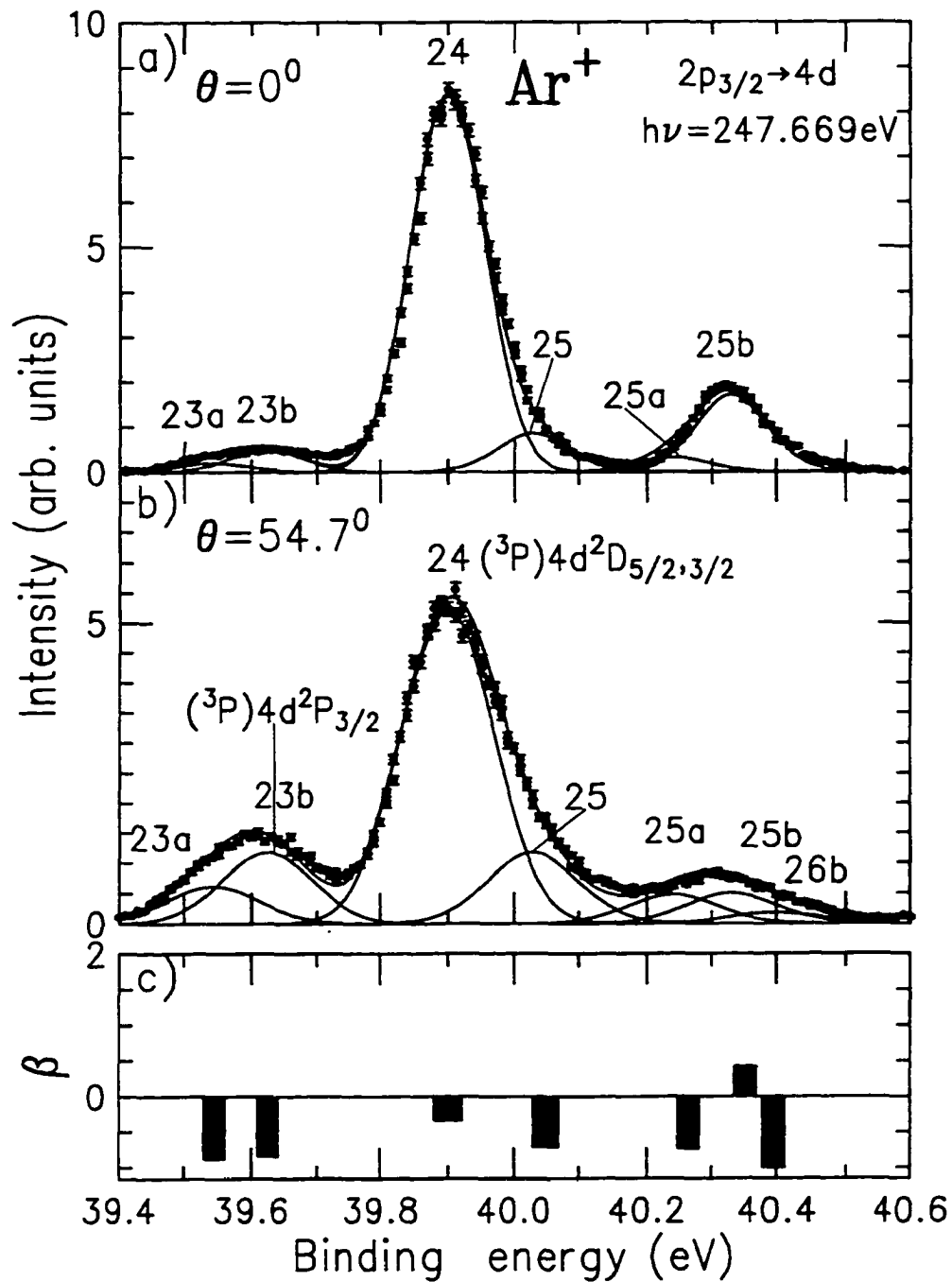


Figure 13. Auger Decay Spectra for Ar $2p_{3/2}^{-1}4d$ Resonance Shown at (a) $\theta = 0^\circ$ and (b) $\theta = 54.7^\circ$. The peak labels correspond to those states listed in Table 8. The β parameters for the $3p^4(^3P)4d^2P$, $3p^4(^3P)4d^2D$, $3p^4(^1D)4d^2G$ and $3p^4(^3P)6s^4P$ lines are shown in (c). The spectra were recorded with a 201 V retarding potential applied to the flight tube. The absolute resonant energies have been given by King et. al. [4].

A complete listing of relative intensities and β parameters for most final ionic states is given in Tables 7-8. The uncertainties in the relative intensities and β parameters are displayed in parentheses following the values. These uncertainties include both systematic and statistical errors and have been calculated using the method described for the $2p^{-1}4s$ β parameters. In this case, the relative intensities are normalized with respect to the well-separated (3P) $4d(^2P_{1/2,3/2})$ lines. The relative intensities of the $2p_{3/2}^{-1}4d$ peaks have been compared with Mursu et al. [50], whose data have been converted to match our normalization. This work, however, is the first reported result of the relative intensities for the $2p_{1/2}^{-1}4d$ transitions. The $3p^44d$ states demonstrate a large overlap with the $3p^43d$ and $3p^4(4s,5s,6s)$ states. The extracted areas, however, do not include these overlapping peaks. This could result in inaccuracies in our determination of the β parameters. This is also the first angular resolved measurement of these transitions and consequently the first measurement of the β parameters for these spectra.

Conclusion

Angular-resolved measurements of the Ar $2p_{1/2,3/2}^{-1}4s$, $3d$, and $4d$ resonant Auger decays have been measured, analyzed and very recently published [51,52]. These measurements were made using time-of-flight electron spectroscopy along with high flux synchrotron radiation from the Advanced Light Source. The intensity distributions and angular distribution anisotropy parameters (β) have been reported

Table 7

Experimental Relative Intensities (Measured at the Magic Angle) and β Parameters
for the Ar $2p_{1/2}^{-1}4d$ Resonance

No	Final State $3p^4nl$ LS-term	Relative Intensity :	β Parameters :
		$2p_{1/2} \rightarrow 4d$ I (θ) This work	$2p_{1/2} \rightarrow 4d$ β This work
15a	$3p^4(^1S)3d^2D_{5/2}$	12.8(2.5)	0.53(.06)
15b	$3p^4(^1S)3d^2D_{3/2}$	109.0(6.3)	-0.58(.06)
15a,b	$3p^4(^1S)3d^2D_{5/2,3/2}$	121.8(7.6)	-0.46(.03)
16a	$3p^4(^3P)5s^4P_{5/2}$	8.6(2.3)	-0.68(.04)
16b	$3p^4(^3P)5s^4P_{3/2}$	-	-
16c	$3p^4(^3P)5s^4P_{1/2}$	12.0(1.9)	-0.61(.04)
16a,b,c	$3p^4(^3P)5s^4P_{5/2,3/2,1/2}$	20.6(0.9)	-0.64(.04)
17a	$3p^4(^3P)5s^2P_{3/2}$	-	-
18a	$3p^4(^3P)4d^4D_{7/2}$	-	-
18b	$3p^4(^3P)4d^4D_{5/2}$	-	-
17b	$3p^4(^3P)5s^2P_{1/2}$	-	-
17a,b	$3p^4(^3P)5s^2P_{3/2,1/2}$	-	-
18c	$3p^4(^3P)4d^4D_{3/2}$	19.6(2.2)	-0.50(.03)
19	$3p^4(^1D)3d^2S_{1/2}$	113.0(6.9)	1.83(.16)
18d	$3p^4(^3P)4d^4D_{1/2}$	-	-
18a,b,c,d	$3p^4(^3P)4d^4D_{7/2,5/2,3/2,1/2}$	19.6(2.2)	-0.50(.03)
20a	$3p^4(^3P)4d^4F_{9/2}$	8.7(2.6)	1.36(.14)
20b	$3p^4(^3P)4d^4F_{7/2}$	12.8(2.8)	-1.00(.05)
21a	$3p^4(^3P)4d^4P_{1/2}$	20.2(1.9)	0.04(.03)
20c	$3p^4(^3P)4d^4F_{5/2}$	-	-
20a,b,c	$3p^4(^3P)4d^4F_{9/2,7/2,5/2}$	21.5(2.8)	-0.04(.03)
21b	$3p^4(^3P)4d^4P_{3/2}$	7.1(3.3)	*
22a	$3p^4(^3P)4d^2F_{7/2}$	19.7(1.9)	-1.00(.05)
21c	$3p^4(^3P)4d^4P_{5/2}$	3.8(0.8)	1.37(.16)
21a,b,c	$3p^4(^3P)4d^4P_{5/2,3/2,1/2}$	31.1(2.5)	1.01(.11)
22b	$3p^4(^3P)4d^2F_{5/2}$	7.5(2.1)	-1.00(.05)
22a,b	$3p^4(^3P)4d^2F_{7/2,5/2}$	27.2(3.5)	-1.00(.05)
23a	$3p^4(^3P)4d^2P_{1/2}$	42.6(2.9)	-0.27(.03)
23b	$3p^4(^3P)4d^2P_{3/2}$	57.4(3.8)	-0.62(.04)
23a,b	$3p^4(^3P)4d^2P_{3/2,1/2}$	100.0	-0.47(.03)
24	$3p^4(^3P)4d^2D_{5/2,3/2}$	238(13)	0.06(.03)
25	$3p^4(^3P)5s^2D_{5/2,3/2}$	37.3(2.6)	-0.72(.04)
25a	$3p^4(^1D)4d^2G_{9/2}$	25.3(2.0)	0.30(.04)
25b	$3p^4(^1D)4d^2G_{7/2}$	12.2(2.3)	0.58(.06)
25a,b	$3p^4(^1D)4d^2G_{9/2,7/2}$	37.5(3.1)	0.44(.06)
26a	$3p^4(^3P)6s^4P_{5/2}$	-	-
26b	$3p^4(^3P)6s^4P_{3/2,1/2}$	8.2(2.2)	-1.00(.05)
26a,b	$3p^4(^3P)6s^4P_{5/2,3/2,1/2}$	8.2(2.2)	-1.00(.05)
27	$3p^4(^1D)4d^2D_{5/2,3/2}$	135.7(8.3)	-0.25(.03)
28	$3p^4(^1D)4d^2P_{3/2,1/2}$	240(14)	0.20(.04)

* Large positive β value.

Table 8

Experimental Relative Intensities (Measured at the Magic Angle) and β Parameters for the Ar $2p_{1/2}^{-1}3d$ Resonance

No	Final State $3p^4nl$ LS-term	Relative Intensity :		β Parameters :
		$2p_{3/2} \rightarrow 4d$ I (θ) This work	I (θ) ^a	$2p_{3/2} \rightarrow 4d$ β This work
15a	$3p^4(^1S)3d^2D_{5/2}$	83.9(5.0)	95.6	-0.68(.04)
15b	$3p^4(^1S)3d^2D_{3/2}$	31.9(2.7)	33.7	-0.50(.03)
15a,b	$3p^4(^1S)3d^2D_{5/2,3/2}$	115.8(7.2)	129.3	-0.62(.04)
16a	$3p^4(^3P)5s^4P_{5/2}$	15.8(2.1)	-	-0.93(.05)
16b	$3p^4(^3P)5s^4P_{3/2}$	2.8(1.5)	23.9	-0.81(.09)
16c	$3p^4(^3P)5s^4P_{1/2}$	6.6(1.9)	-	-0.90(.09)
16a,b,c	$3p^4(^3P)5s^4P_{5/2,3/2,1/2}$	25.2(2.6)	23.9	-0.90(.05)
17a	$3p^4(^3P)5s^2P_{3/2}$	-	-	-
18a	$3p^4(^3P)4d^4D_{7/2}$	-	-	-
18b	$3p^4(^3P)4d^4D_{5/2}$	-	-	-
17b	$3p^4(^3P)5s^2P_{1/2}$	-	-	-
17a,b	$3p^4(^3P)5s^2P_{3/2,1/2}$	-	-	-
18c	$3p^4(^3P)4d^4D_{3/2}$	50.1(3.5)	82.6	-0.06(.02)
19	$3p^4(^1D)3d^2S_{1/2}$	42.2(3.1)	56.5	0.84(.08)
18d	$3p^4(^3P)4d^4D_{1/2}$	-	-	-
18a,b,c,d	$3p^4(^3P)4d^4D_{7/2,5/2,3/2,1/2}$	50.1(3.5)	82.6	-0.06(.02)
20a	$3p^4(^3P)4d^4F_{9/2}$	1.4(**)	-	*
20b	$3p^4(^3P)4d^4F_{7/2}$	9.3(1.5)	15.2	-1.00(.05)
21a	$3p^4(^3P)4d^4P_{1/2}$	15.4(2.3)	-	-0.30(.05)
20c	$3p^4(^3P)4d^4F_{5/2}$	-	32.6	-
20a,b,c	$3p^4(^3P)4d^4F_{9/2,7/2,5/2}$	10.7(2.6)	47.8	-0.95(.05)
21b	$3p^4(^3P)4d^4P_{3/2}$	-	-	-
22a	$3p^4(^3P)4d^2F_{7/2}$	-	-	-
21c	$3p^4(^3P)4d^4P_{5/2}$	7.6(1.5)	10.8	-1.00(.05)
21a,b,c	$3p^4(^3P)4d^4P_{5/2,3/2,1/2}$	23.0(1.9)	10.8	-0.53(.03)
22b	$3p^4(^3P)4d^2F_{5/2}$	9.4(1.4)	-	-0.70(.04)
22a,b	$3p^4(^3P)4d^2F_{7/2,5/2}$	9.4(1.4)	-	-0.70(.04)
23a	$3p^4(^3P)4d^2P_{1/2}$	34.4(2.4)	46.7	-0.88(.05)
23b	$3p^4(^3P)4d^2P_{3/2}$	65.6(4.2)	53.3	-0.83(.05)
23a,b	$3p^4(^3P)4d^2P_{3/2,1/2}$	100.0	100.0	-0.85(.05)
24	$3p^4(^3P)4d^2D_{5/2,3/2}$	291(16)	330.4	-0.34(.03)
25	$3p^4(^3P)5s^2D_{5/2,3/2}$	65.6(4.1)	36.9	-0.71(.04)
25a	$3p^4(^1D)4d^2G_{9/2}$	26.7(1.9)	-	-0.73(.04)
25b	$3p^4(^1D)4d^2G_{7/2}$	28.2(2.4)	-	0.42(.06)
25a,b	$3p^4(^1D)4d^2G_{9/2,7/2}$	54.9(3.9)	-	-0.15(.03)
26a	$3p^4(^3P)6s^4P_{5/2}$	-	-	-
26b	$3p^4(^3P)6s^4P_{3/2,1/2}$	10.1(1.6)	-	-1.00(.05)
26a,b	$3p^4(^3P)6s^4P_{5/2,3/2,1/2}$	10.1(1.6)	-	-1.00(.05)
27	$3p^4(^1D)4d^2D_{5/2,3/2}$	292(17)	469.5	-0.35(.03)
28	$3p^4(^1D)4d^2P_{3/2,1/2}$	415(23)	131.5	-0.43(.03)

a. According to Mursu et al. [50].

* Large positive β value.

** Very weak line having large uncertainty.

[51,52] for nearly all of the $3p^4nl$ final ionic states, and a comparison of these measurements with previous results demonstrates good agreement. It has been shown that a large majority of the β parameters are either small positive or negative. As predicted by the spectator model, the averaged β is isotropic in the case of the $2p_{1/2}^{-1}4s$ resonance. This result corroborates the work by Cooper [19] using the angular momentum transfer theory. In addition, our higher resolution measurements allowed the determination of individual large β values, which appear much weaker in previously unresolved measurements due to a strong cancellation effect by neighboring lines.

This work also demonstrated that while the intensity distributions between different resonances originating from different $2p$ spin states (i.e. $2p_{1/2}$ vs. $2p_{3/2}$) are not always similar, the extracted β parameters for the two resonances agree in many cases. Our results for the intensity distributions further support the prediction of the spectator model for the $2p_{1/2,3/2}^{-1}4s$ resonances, but demonstrate the breakdown of this model for the $2p_{1/2,3/2}^{-1}3d$ and $2p_{1/2,3/2}^{-1}4d$ resonances. Our results agree with much of the theoretical results for the $2p_{1/2,3/2}^{-1}4s$ resonances. However, we hope that this work, which is the first in (a) the case of the β parameters for the $2p_{1/2,3/2}^{-1}3d$ and $2p_{3/2}^{-1}4d$ resonances, and (b) the intensity and β parameter for the $2p_{1/2}^{-1}4d$ resonance, will stimulate further experimental and theoretical investigations.

CHAPTER V

RESONANT AUGER STUDIES IN Kr $3d_{3/2,5/2}^{-1}np$ STATES USING ANGLE-RESOLVED ELECTRON IMAGING SPECTROSCOPY

Abstract

The resonant Auger decay of all the photoexcited $3d_{3/2,5/2}^{-1}np$ states ($n = 5,6,7,8$ and 9) in Kr has been studied, using photons from an undulator beamline at the ALS, and an angle resolved photoelectron imaging spectroscopy technique to record the electron spectra of Kr near the $3d$ ionization threshold. Angular distributions, spectator and shake probabilities have been derived for the Kr $3d^{-1}np \rightarrow 4s^{-1}4p^{-1}(^1P)mp + e^-$ ($n = 5-9$, $m = 5-11$) resonance Auger decay. The results show that the spectator-core coupling is strong at lower n ($n = 5,6$) but it lessens for higher n , with a shake up of $m = n+1$ preferred. A very similar behavior is obtained when comparing the above mentioned probabilities ($3d^{-1}np \rightarrow 4s^{-1}4p^{-1}(^1P)mp$) with previous experimental and theoretical spectator and shake probabilities and with experimental spectator and shake probabilities for the Kr $3d^{-1}np \rightarrow 4s^24p^{-2}mp$ ($n = 5-9$, $m = 5-11$) resonance Auger transitions. No prior angular distributions measurement for the Kr $3d^{-1}np \rightarrow 4s^{-1}4p^{-1}(^1P)mp + e^-$ ($n = 5-9$, $m = 5-11$) resonance Auger decay has been published.

Introduction

The Auger decay spectra of krypton at the $3d \rightarrow 5p$ resonance were first reported by Eberhardt et al. [53]. Since then the resonant Auger transitions and correlation satellite spectra of krypton have been subjects of both experimental [54-59] and theoretical [33,60] studies which have concentrated on the decay to the lowest lying Kr^+ml states. Unfortunately, the Auger decay spectra of the $(Kr\ 3d^{-1}np \rightarrow 4s^{-1}4p^{-1}(^1P)mp)$ ($n = 5-9$, $m = 5-11$) transitions have been neglected. To the best of our knowledge, the first attempt to measure these transitions was made by Aksela et al. [12], with lower experimental resolution that could not resolve the transitions well. Very recently Mursu et al. [61] have studied these transitions. However, they did not study the angular distributions, which is the main emphasis of our work in this chapter. In addition, they could not derive the shake probabilities for all the $4s^{-1}4p^{-1}np$ final states at various resonant excitations.

Åberg [62] formulated the shake model to explain successfully the shake contributions in the spectator resonance Auger spectra. He introduced a complete theoretical treatment for the shake theory including electron correlation in both the ground and final state. Martin and Shirley [63] first demonstrated the importance of including correlated many-electron wave functions for both the initial and final states where the final state wave functions must be orthogonal to each other. This theory was later formulated in a more general form by Arneberg et al. [64], who used second quantization notation.

In this chapter, we present experimental results on photoexcitation and photoi-

onization in Kr by measuring the Auger decay spectra of the Kr ($3d^{-1}np \rightarrow 4s^{-1}4p^1(^1P)mp$) ($n = 5-9$, $m = 5-11$) transitions using angle-resolved photoelectron imaging spectroscopy coupled with photons from an undulator beamline of the ALS. In addition, this work presents for the first time the angular distributions of the resonant Auger electrons resulting from the decay of $3d_{3/2,5/2}^{-1} \rightarrow np$ states. Spectator and shake probabilities for the $3d^{-1}np \rightarrow 4s^{-1}4p^1(^1P)mp$ ($n = 5-9$, $m = 5-11$) resonance Auger transitions have been obtained for almost all the final $4s^{-1}4p^1(^1P)mp$ ($m = 5-11$) states.

Results and Discussion

Figure 14 shows a three-dimensional mapping of the resonant Auger landscape, which was obtained at an angle of 0^0 relative to the polarization plane. As can be seen from this figure, the general features are the two groups of Kr $4s^24p^4nl$ and $4s^14p^5n^1l^1$ transitions. The z-axis represents the intensity, the y-axis the photon energy, and the x-axis the binding energy. The x-y plane of this 3D map is shown in Figure 15 as a two-dimensional 2D-electron emission map depicted in the main panel of Figure 15. In this map, the data is plotted in a contour configuration and the intensity of the electron signal is represented as different shades of gray, where darker regions indicate stronger intensities. The horizontal axis represents the binding energy, and the vertical axis the photon energy.

This 2D map allows closer observation of various structures; it allows examination of all of the data in order to spot areas of interest and in order to follow the progression of various processes. It also allows us to quickly observe experimental

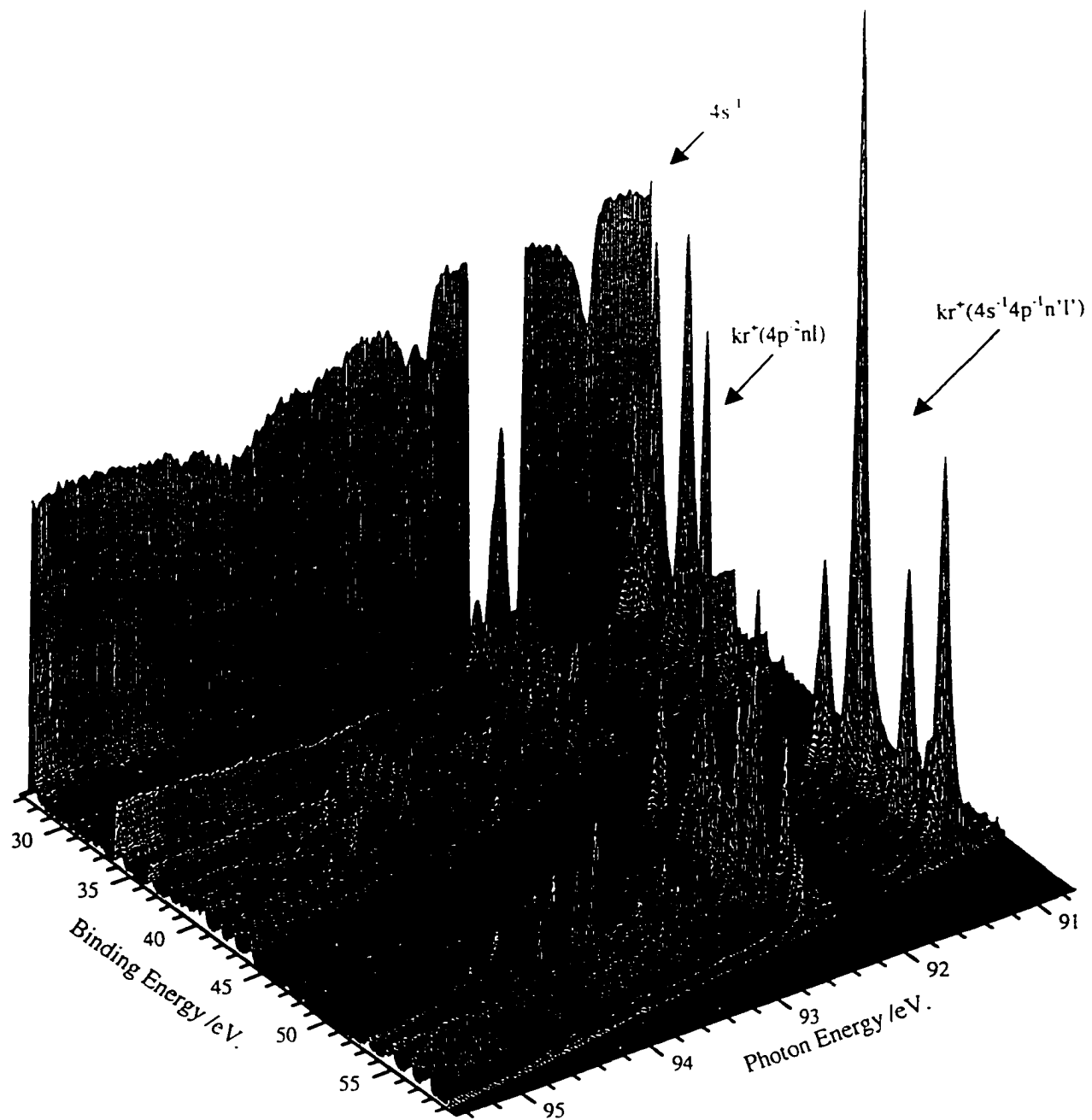


Figure 14. Three Dimensional Mapping of the Resonant Auger Landscape Measured at 0° Relative to the Polarization Plane.

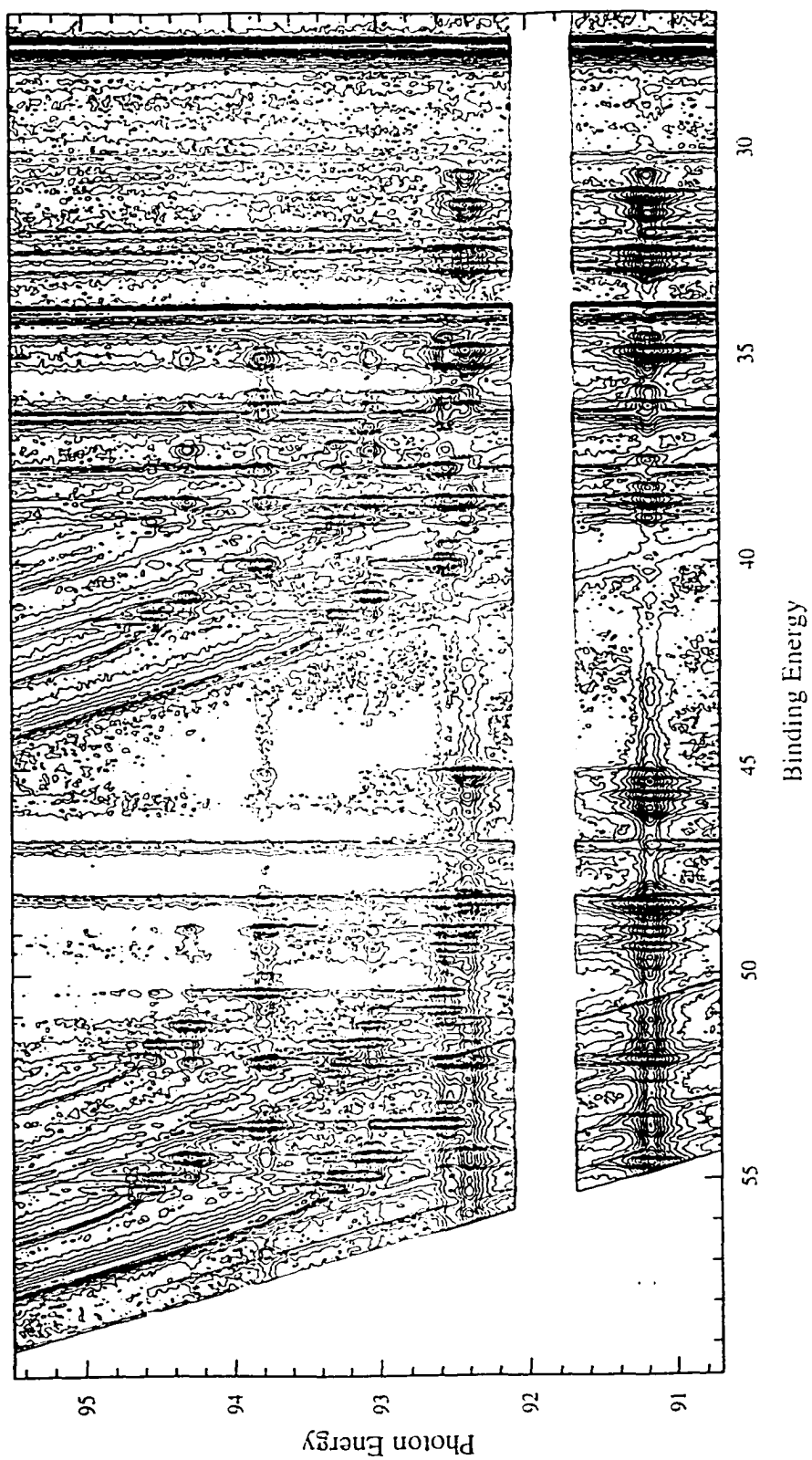


Figure 15. Two-dimensional (2D) Map Showing Auger Electron of the Rydberg Resonances Measured at 0° Relative to the Polarization Plane. The intensity of the electron signal is represented as different shade of gray, where darker regions indicating stronger intensity.

artifacts, such as peaks due to higher order or background electrons, to be identified and removed from the 2D data. In this particular experiment, it was used to observe the progression of the np Rydberg series $n = 5-11$ over a photon energy range of 6 eV. To produce 2D electron emission data sets, a photon energy range of 6-eV-wide and a kinetic energy window covering the majority of the ejected electrons was chosen to allow the investigation of the Kr 3d ionization processes. This data was collected by setting the photon energy to the beginning of the range of interest and photoelectron spectra (PES) were accumulated simultaneously in each analyzer for 10 s. The photon energy was then incremented by 10 meV ($1/4 \times$ photon resolution) and another pair of PES was collected. By repeating this procedure over the photon energy range of interest, which takes a total of about two and a half hours, we are able to produce comprehensive and detailed 2D images. The photon energy step was changed to 100 meV between the $3d_{5/2}^{-1}5p$ and $3d_{3/2}^{-1}5p$ resonances where no resonance states are expected (as shown in Figure 15).

The spectral region covered in the 2D map can be broken down into three parts: (1) The low lying $3d^{-1}np$ ($n = 5-9$) resonances; (2) The overlapping of the high lying resonances and the ionization edges to which they converge, (intermediate states); and (3) The normal Auger lines following the 3d ionization, which exhibit shifting, and broadening due to post collision interaction (PCI). In the case of (1), the low lying resonances lies below the 3d inner shell ionization threshold where the Rydberg electron keeps its angular momentum during the resonant Auger emission but changes its principal quantum number. In the case of (2), the intermediate states

lie just below and just above the 3d-ionization threshold. When the photon energy passes the threshold the shake down processes become more dominant than the shake up. Details of how this evolution takes place are not clear from the theoretical point of view [65]. The case of (3), the so-called normal Auger decay, is shown in the 2D map as intense diagonal lines, which represent the direction of the kinetic energy, and form 45° with the horizontal line that corresponds to the binding energy axis. This decay involves the ejection of an inner-shell electron into the continuum followed by the decay of another electron to the inner shell vacancy and the simultaneous ejection of a second electron, leaving a doubly ionized ion core [34]. Just above the 3d inner shell ionization threshold, the Auger lines exhibit shifting, and broadening due to PCI, where a slow photoelectron is produced resulting in a singly charged ion [66]. Immediately afterward, the lower-lying electrons fill the inner-shell hole, producing a fast Auger electron. If the lifetime of the inner shell hole is very short, the fast Auger electron can overtake the slow photoelectron. The Auger electron is exposed to a singly charged ion, while the photoelectron is exposed to a doubly charged ion core. The out-going photoelectron will be retarded and lose a certain amount of energy while the Auger electron will gain energy. If the retardation is large enough, the photoelectron will not escape and will be recaptured resulting in the final ionic state of a singly charged ion. This exchange of energy between the outgoing slow 3d photoelectron and the fast Auger electron results in a shift in the peak energy. This energy shift can be seen clearly, from the 2D map, from the 3d threshold to the Rydberg States.

In order to observe the details and obtain quantitative information, we extracted from the 2D image photoelectron spectra (PES). Figure 16 a shows a photoelectron spectrum measured at an angle of 54.7° with respect to the electric field vector of the linearly polarized synchrotron beam. The photon energy of 91.2 eV corresponds to the Kr $3d_{5/2} \rightarrow 5p$ transition. This spectrum displays on resonance the population of the Kr $4s^{-1}$, $4p^{-2}nl$, $4s^{-1}4p^{-1}n'l'$ and $4s^{-2}n'l'$ ionic states. The energy scale of the TOF analyzers is non-linear and their resolution is best at lowest kinetic energies. Here the best spectrometer resolution was 110 meV decreasing at the highest kinetic energies to become 147 meV. The photon energy resolution was set to 40 meV at 90 eV. Clearly, one can see that the overall intensity of the lines resulting from transitions to the $Kr^+(4s^{-1}4p^{-1}n'l')$ states is similar to that of the transitions to the $Kr^+(4p^{-2}nl)$ states (the ratio of the intensities of the two groups of lines was 1.2). Similar results have been shown in the case of the Xe $5s^{-1}5p^{-1}n'l'$ and Xe $5p^{-2}nl$ following the Xe $4d_{3/2} \rightarrow 6p$ decay [67]. In order to study the $4s^{-1}4p^{-1}n'l'$ ionic states with optimum resolution, we used a retarding voltage of -30 V on the TOF analyzers since the spectral lines are better resolved as is shown in Figure 16 b. It should be noted that in Figure 16 b, the peaks c and d represent experimental artifacts and the end of the spectrum due to the retarding voltage.

Figures 17 and 18 (0° and 54.7° respectively) show in panels (a-g) the constant ionic states spectra of the Kr^+np ($n = 5-11$) extracted from the 2D data sets at two different angles, while panel h in Figures 17 and 18 shows the total electron yield. At the $3d_{5/2}^{-1}5p$ resonance an asymmetry can be observed at the low photon energy side,

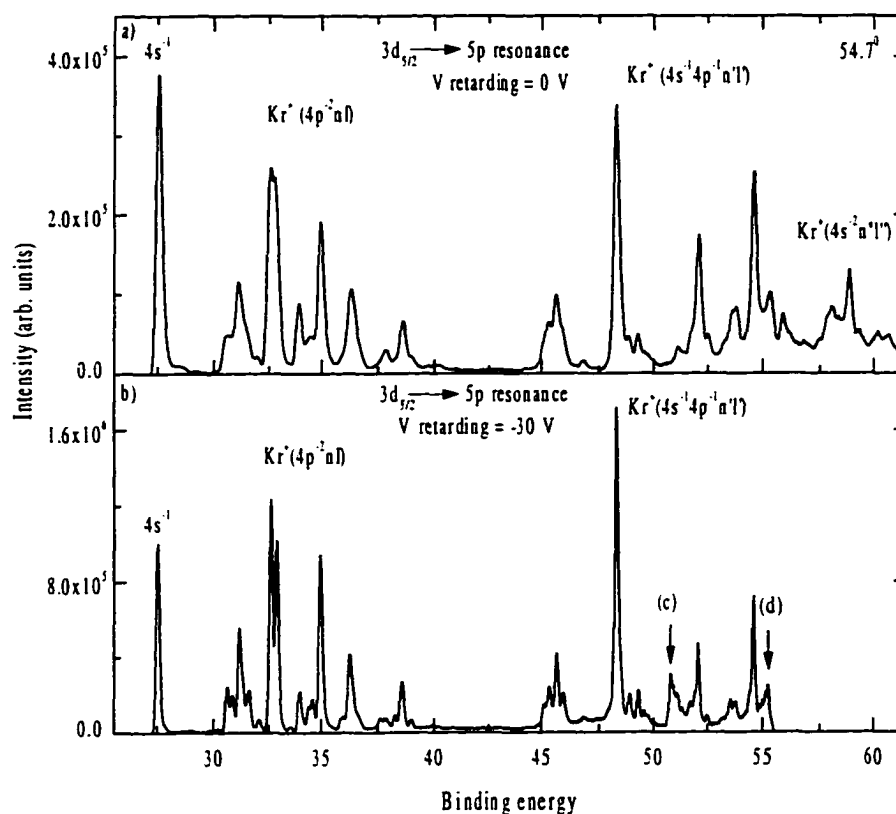


Figure 16. Photoelectron Spectrum of the $3d_{5/2} \rightarrow 5p$ Resonance Taken at the 54.7^0 With Respect to the Electric-field Vector of the Incident Radiation. (a) Data Collected With no Retarding Potential. (b) Data Collected With -30 V Retarding Potential.

panels (e, f and g) for both Figures 17 and 18 respectively. This is due to the higher order lines lying at the edge of the resonance. One can see from panel (a) features arising from very slow electrons, from the previous photon pulse, appearing in a certain photon energy range (92.8-96 eV) of the spectra. Assignments and experimental shake-up probabilities for a given $4s^{-1}4p^{-1}(^1P)np$ final state are given in Table 9. The experimental shake-up probabilities were obtained as a percentage of the total intensity of all the $4s^{-1}4p^{-1}(^1P)np$ final states at each resonance. The statistical uncertainty

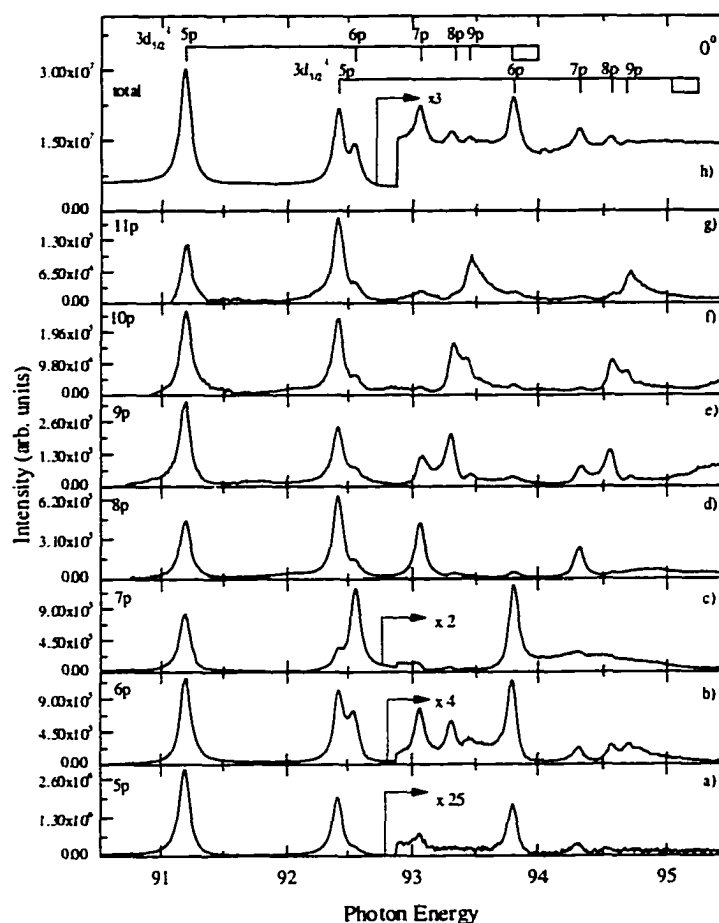


Figure 17. (a)-(g) Constant Ionic State Spectra of the $\text{Kr}^+ np$ ($n = 5-11$) Extracted From the (2D) Display at 0° Relative to the Polarization Plane. The Total Electron Yield is Shown on Panel (h).

in the last digit is given in brackets. The assignments have been made by comparison with the quantum defects obtained from previously measured $\text{Kr}^+ 4s^2 4p^4 ({}^{2S+1}L_J) ns, np$ and nd states [57]. The quantum defects obtained from measurements agree best with those corresponding to the $\text{Kr}^+ ({}^S L_J) np$ Rydberg states. It is very clear from table 9 that the spectator core coupling is very strong in the decay of $3d^{-1}5p \rightarrow 4s^{-1}4p^{-1}({}^1P)$ 5p and $3d^{-1}6p \rightarrow 4s^{-1}4p^{-1}({}^1P)6p$ excitations. In the region where the resonance lines

are well separated ($n = 7-9$), the probabilities of the spectator transition become very small (less than 9 %) and shake-up processes ($Kr^+ np \rightarrow Kr^+(n+1)p$) become very important.

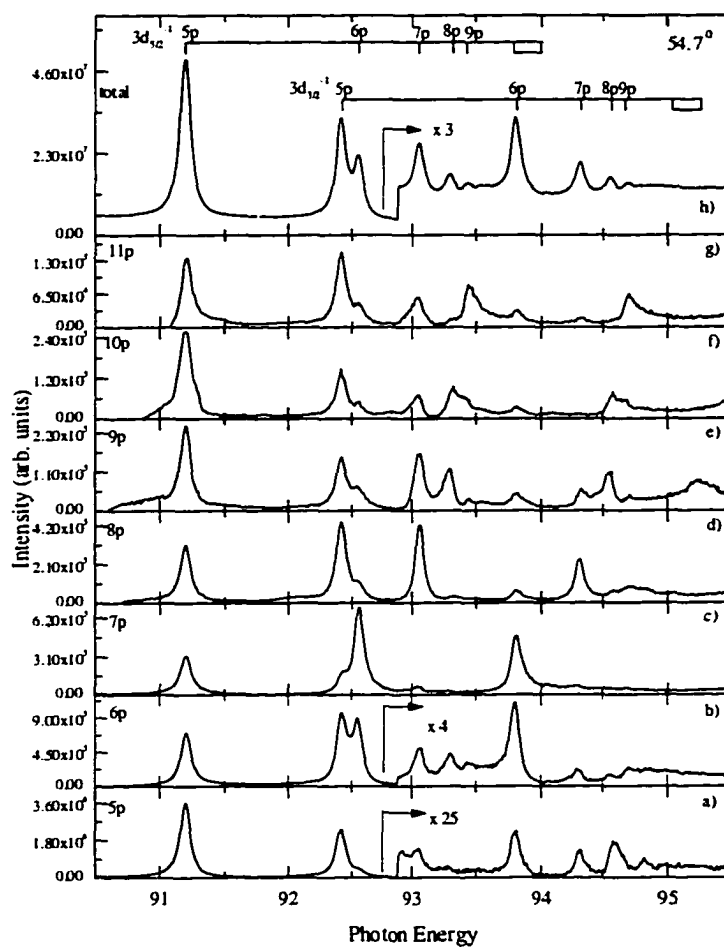


Figure 18. (a)-(g) Constant Ionic State Spectra of the $Kr^+ np$ ($n = 5-11$) Extracted From the (2D) Display at 54.7° Relative to the Polarization Plane. The Total Electron Yield is Shown on Panel (h).

A comparison of these results with measurements and theoretical calculations made by Mursu et al. [61] showed a similar behavior as indicated in Table 9. How-

ever, Mursu et al. could not resolve all the final $4s^{-1}4p^{-1}(^1P)np$ states as shown in the table.

Table 9

Experimental Spectator and Shake Probabilities (in Percentage of the Total Intensities of all the $4s^{-1}4p^{-1}(^1P)mp$ Resonances) for the $3d^{-1}np \rightarrow 4s^{-1}4p^{-1}(^1P)mp$ ($n = 5-9$, $m = 5-11$) Resonance Auger Transitions

Resonant state $3d^{-1}np$								
Final ionic state	n = 5				n = 6			
	$3d_{5/2}^{-1}$		$3d_{3/2}^{-1}$		$3d_{5/2}^{-1}$		$3d_{3/2}^{-1}$	
	This work	Ref. [61] Exp./Calc.						
$4s^{-1}4p^{-1}(^1P)5p$	64.3(4)	75/77	56.6(5)	18/8	8.2(3)	18/8	9.2(3)	7/8
$4s^{-1}4p^{-1}(^1P)6p$	13.0(3)	20/22	21.2(5)	20/23	42.1(7)	29/35	28.7(6)	27/33
$4s^{-1}4p^{-1}(^1P)7p$	5.9(3)	5/0	1.7(3)	5/0	41.1(6)	53/56	46.1(5)	66/57
$4s^{-1}4p^{-1}(^1P)8p$	5.3(2)		11.0(3)		3.3(3)		5.1(2)	
$4s^{-1}4p^{-1}(^1P)9p$	4.1(2)		3.3(2)		3.1(3)		5.2(3)	
$4s^{-1}4p^{-1}(^1P)10p$	5.3(4)		3.0(5)		1.0(4)		2.0(3)	
$4s^{-1}4p^{-1}(^1P)11p$	2.1(8)		3.2(6)		1.2(5)		3.7(4)	
Resonant state $3d^{-1}np$								
Final ionic State	n = 7				n = 8			
	$3d_{5/2}^{-1}$		$3d_{3/2}^{-1}$		$3d_{5/2}^{-1}$		$3d_{3/2}^{-1}$	
	This work	Ref. [61] Exp./Calc.						
$4s^{-1}4p^{-1}(^1P)5p$	-	-/-	-	-/-	-	-/-	-	-/-
$4s^{-1}4p^{-1}(^1P)6p$	9.8(3)	10/10	9.2(3)	9/10	5.7(3)	18/4	5.6(2)	11/4
$4s^{-1}4p^{-1}(^1P)7p$	2.2(4)	5/4	2.5(3)	0/4	0.4(4)	4/4	1.6(3)	-/-
$4s^{-1}4p^{-1}(^1P)8p$	37.1(8)	73/73	47.2(5)	73/74	1.5(3)	6/2	4.1(2)	3/0
$4s^{-1}4p^{-1}(^1P)9p$	25.1(5)	12/10	38.3(7)	18/10	40.7(5)	43/57	44.4(7)	54/57
$4s^{-1}4p^{-1}(^1P)10p$	16.0(6)		-		29.0(4)	30/31	41.7(6)	32/31
$4s^{-1}4p^{-1}(^1P)11p$	9.8(4)		2.8(4)		22.7(4)	-/-	2.6(3)	-/-
Resonant state $3d^{-1}np$								
Final ionic State	n = 9							
	$3d_{5/2}^{-1}$		$3d_{3/2}^{-1}$					
	This work	Ref. [61] Exp.	This work	Ref. [61] Exp.				
$4s^{-1}4p^{-1}(^1P)5p$	-	-	-	-				
$4s^{-1}4p^{-1}(^1P)6p$	1.7(3)	9	1.1(3)	10				
$4s^{-1}4p^{-1}(^1P)7p$	1.3(3)	5	1.8(4)	-				
$4s^{-1}4p^{-1}(^1P)8p$	-	6	2.1(3)	-				
$4s^{-1}4p^{-1}(^1P)9p$	4.3(2)	11	1.5(4)	7				
$4s^{-1}4p^{-1}(^1P)10p$	67.8(6)	38	60.2(5)	36				
$4s^{-1}4p^{-1}(^1P)11p$	24.9(5)	31	33.3(5)	40				

The statistical uncertainty of the last digits is given in parentheses

Although our and Mursu et al.'s results [61] are in reasonable agreement, it is possible that the discrepancy is due to the fact that they did not resolve all the states. In our case, we could resolve up to $n = 11$ in the case of the $3d^{-1}5p \rightarrow 4s^{-1}4p^{-1}(^1P)np$ while they resolved only the first three final states ($n = 7$). Similar behavior has been found in the decay of the $3d^{-1}5p \rightarrow 4p^{-2}5p$ and the $3d^{-1}6p \rightarrow 4p^{-2}6p$ excitations in Kr by Jauhiainen et al. [57]. The probability for the $3d_{5/2}^{-1}5p \rightarrow 4s^{-1}4p^{-1}(^1P)6p$ excitation was found to be 13%. Significantly higher shake-up probability (21%) can be seen in the case of $3d_{3/2}^{-1}5p \rightarrow 4s^{-1}4p^{-1}(^1P)6p$ excitation which is also found for the decay to the $4p^{-2}np$ case [57]. This similarity is extended to a comparison with the Xe $4d^{-1}6p$ resonances [68], where they noticed that the shake probabilities behaved exactly the same way.

Åberg [65], in his theoretical work has explained the shake probability $P_{nn'}$ = $|\langle n'l_j | n'l'_j \rangle|^2$ where the orbital $|n'l_j\rangle$ is evaluated in the field of the singly charged ion with the hole in the subshell $n_i l_i j_i$, whereas $|n'l_j\rangle$ must be evaluated in the field of the final doubly charged ion. He found that the probability of the spectator electron $P_{nn'}$ oscillates as a function of n' . The maximum values of $P_{nn'}$ become smaller and the shake-up probability becomes important as n' increases. Comparing our experimental results with his theoretical prediction shows a good agreement.

Figures 19-25 show angle comparisons of the $3d^{-1}np \rightarrow 4s^{-1}4p^{-1}(^1P)mp$ ($n = 5-9$, $m = 5-11$) transitions. Table 10 shows the experimental β values extracted from the $3d^{-1}np \rightarrow 4s^{-1}4p^{-1}(^1P)mp$ ($n = 4-9$, $m = 5,11$) resonance Auger transitions. For each β value, the uncertainty is given in parentheses. It should be noted that this uncer-

tainty has been calculated by comparing β values for the $3d_{5/2}^{-1}5p \rightarrow 4s^{-1}4p^{-1}(^1P)5p$ resonance from two data sets (0 and 30 V retarding potential) and the percentage differences for each value has been found. Then the uncertainties obtained were applied to all the resonances studied.

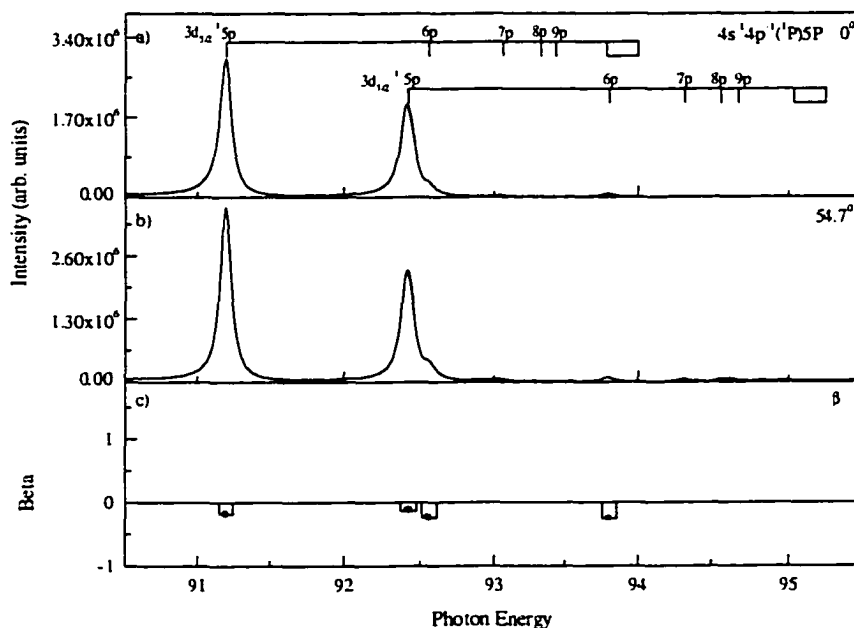


Figure 19. Constant Ionic State Spectra of the Kr^+ 5p Extracted From the (2D) Display at Two Different Angles (a) 0° and (b) 54.7° Relative to the Polarization Plane; (c) Shows the Angular Distribution Parameter β for the $3d^{-1}np \rightarrow 4s^{-1}4p^{-1}(^1P)5p$ ($n = 4-9$) Resonance Auger Transitions.

As yet, there are neither theoretical predictions nor experimental observations for such angular information. We can note that nearly isotropic angular distributions are observed for most of the $3d^{-1}np \rightarrow 4s^{-1}4p^{-1}(^1P)mp$ ($n = m$) strict spectator decays. However, decays involving shake up ($m > n$) or shake down ($m < n$) show larger anisotropies. According to the prediction of the strict spectator model, introduced by Hergenhahn et al. [20], these β values have to be zero, and this agrees qualitatively

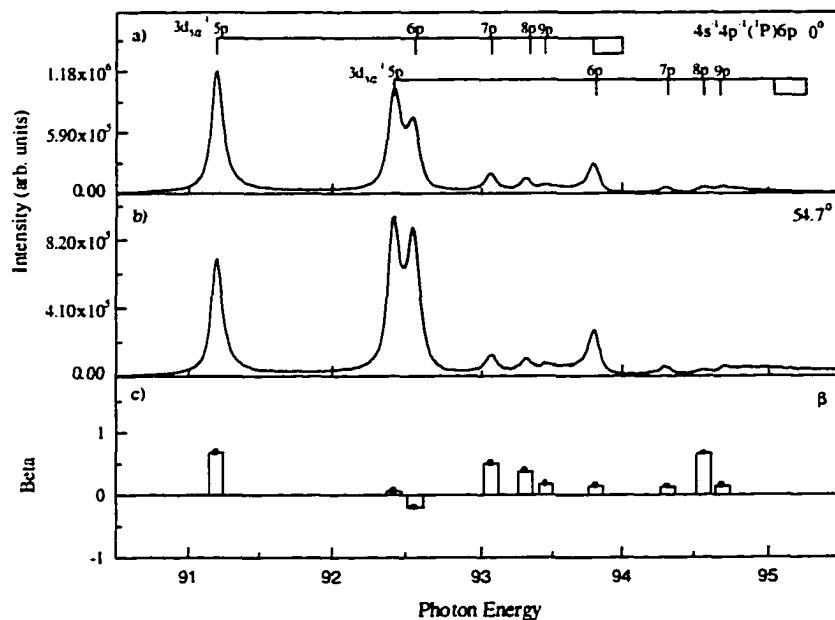


Figure 20. Constant Ionic State Spectra of the Kr^+ 6p Extracted From the (2D) Display at Two Different Angles (a) 0° and (b) 54.7° Relative to the Polarization Plane; (c) Shows the Angular Distribution Parameter β for the $3d^{-1}np \rightarrow 4s^{-1}4p^{-1}(^1P)6p$ ($n = 4-9$) Resonance Auger Transitions.

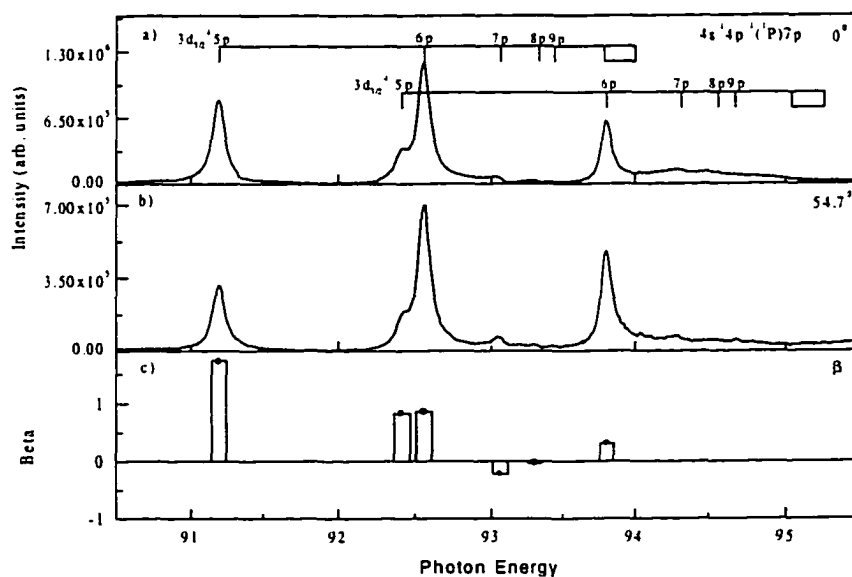


Figure 21. Constant Ionic State Spectra of the Kr^+ 7p Extracted From the (2D) Display at Two Different Angles (a) 0° and (b) 54.7° Relative to the Polarization Plane; (c) Shows the Angular Distribution Parameter β for the $3d^{-1}np \rightarrow 4s^{-1}4p^{-1}(^1P)7p$ ($n = 4-9$) Resonance Auger Transitions.

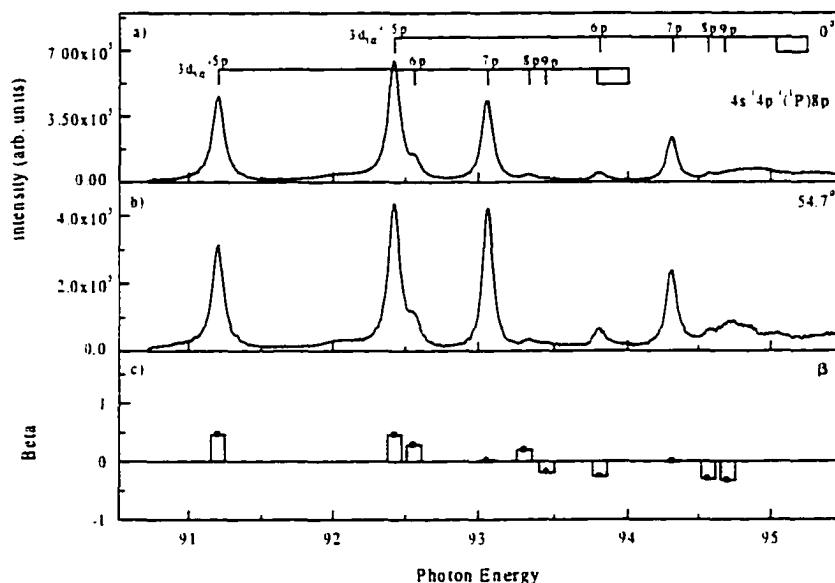


Figure 22. Constant Ionic State Spectra of the Kr^+ 8p Extracted From the (2D) Display at Two Different Angles (a) 0° and (b) 54.7° Relative to the Polarization Plane; (c) Shows the Angular Distribution Parameter β for the $3d^{-1}np \rightarrow 4s^{-1}4p^{-1}(^1P)8p$ ($n = 4-9$) Resonance Auger Transitions.

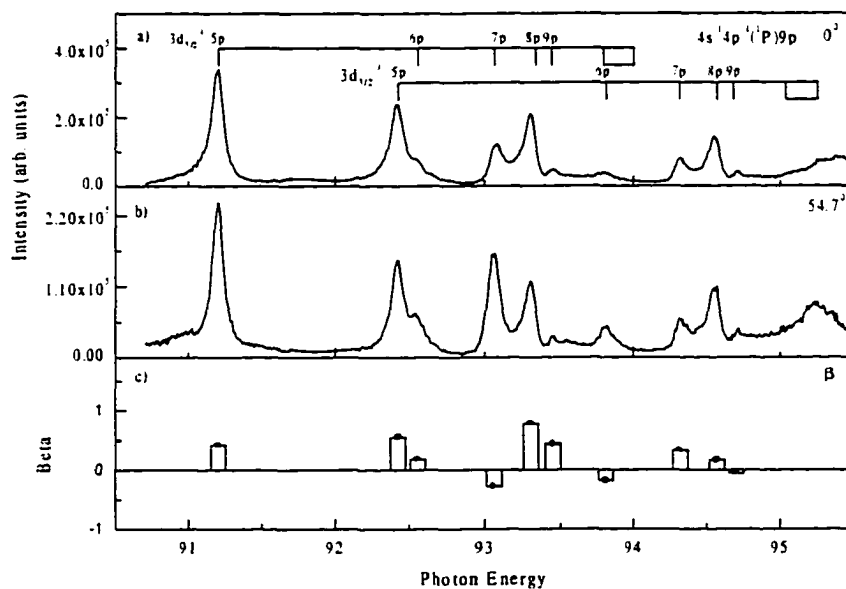


Figure 23. Constant Ionic State Spectra of the Kr^+ 9p Extracted From the (2D) Display at Two Different Angles (a) 0° and (b) 54.7° Relative to the Polarization plane; (c) Shows the Angular Distribution Parameter β for the $3d^{-1}np \rightarrow 4s^{-1}4p^{-1}(^1P)9p$ ($n = 4-9$) Resonance Auger Transitions.

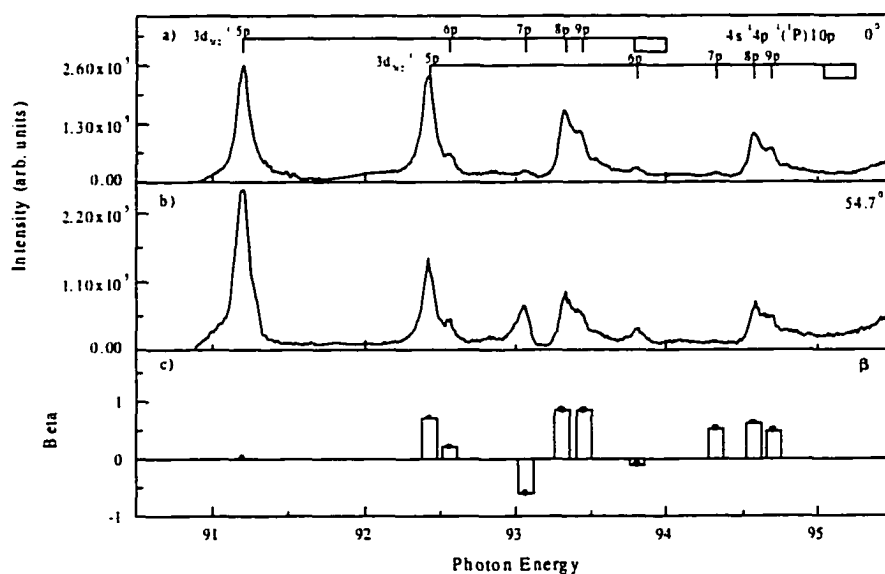


Figure 24. Constant Ionic State Spectra of the Kr^+ 10p Extracted From the (2D) Display at Two Different Angles (a) 0° and (b) 54.7° Relative to the Polarization Plane; (c) Shows the Angular Distribution Parameter β for the $3d^{-1}np \rightarrow 4s^{-1}4p^{-1}(^1P)10p$ ($n = 4-9$) Resonance Auger Transitions.

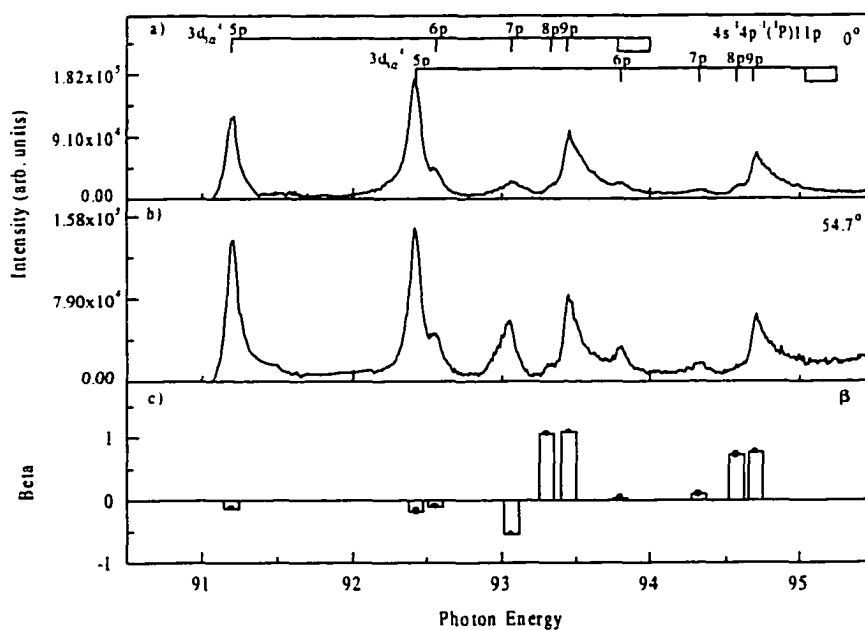


Figure 25. Constant Ionic State Spectra of the Kr^+ 11p Extracted From the (2D) Display at Two Different Angles (a) 0° and (b) 54.7° Relative to the Polarization plane; (c) Shows the Angular Distribution Parameter β for the $3d^{-1}np \rightarrow 4s^{-1}4p^{-1}(^1P)11p$ ($n = 4-9$) Resonance Auger Transitions.

with our experimental observations. When the 3d electrons are excited to the 7p or higher Rydberg orbitals, (Figures 21-25), the strength of the spectator core coupling diminishes, the shake up transition becomes dominant, and a fluctuation of β values is observed.

Table 10

Experimental Angular Distribution Anisotropy Parameters (β) for the $3d^{-1}np \rightarrow 4s^{-1}4p^{-1}mp$ ($n = 5-9$, $m = 5-11$) Resonance Auger Transitions

Final ionic state	Resonant state $3d^{-1}np$					
	$n = 5$		$n = 6$		$n = 7$	
	$3d_{5/2}^{-1}$	$3d_{3/2}^{-1}$	$3d_{5/2}^{-1}$	$3d_{3/2}^{-1}$	$3d_{5/2}^{-1}$	$3d_{3/2}^{-1}$
$4s^{-1}4p^{-1}(^1P)5p$	-0.18(6)	-0.14(5)	-0.24(8)	-0.26(9)	-	-
$4s^{-1}4p^{-1}(^1P)6p$	0.68(16)	0.06(2)	-0.20(5)	0.14(4)	0.50(12)	0.12(3)
$4s^{-1}4p^{-1}(^1P)7p$	1.73(17)	0.83(8)	0.86(9)	0.31(3)	-0.22(2)	-
$4s^{-1}4p^{-1}(^1P)8p$	0.46(11)	0.46(11)	0.28(7)	-0.26(6)	0.02(5)	-0.01(3)
$4s^{-1}4p^{-1}(^1P)9p$	0.42(10)	0.54(13)	0.18(5)	-0.18(5)	-0.28(7)	0.33(8)
$4s^{-1}4p^{-1}(^1P)10p$	0.01(2)	0.71(17)	0.21(5)	-0.11(3)	-0.60(15)	0.52(13)
$4s^{-1}4p^{-1}(^1P)11p$	-0.13(3)	-0.18(5)	-0.10(3)	0.03(2)	-0.54(13)	0.10(3)
Final ionic state	$n = 8$		$n = 9$			
	$3d_{5/2}^{-1}$	$3d_{3/2}^{-1}$	$3d_{5/2}^{-1}$	$3d_{3/2}^{-1}$		
$4s^{-1}4p^{-1}(^1P)5p$	-	-	-	-		
$4s^{-1}4p^{-1}(^1P)6p$	0.37(9)	0.66(15)	0.17(4)	0.14(3)		
$4s^{-1}4p^{-1}(^1P)7p$	-0.03(3)	-	-	-		
$4s^{-1}4p^{-1}(^1P)8p$	0.20(5)	0.30(8)	-0.19(5)	-0.33(8)		
$4s^{-1}4p^{-1}(^1P)9p$	0.77(19)	0.17(4)	0.43(11)	-0.06(2)		
$4s^{-1}4p^{-1}(^1P)10p$	0.85(21)	0.62(15)	0.85(21)	0.48(12)		
$4s^{-1}4p^{-1}(^1P)11p$	1.06(22)	0.72(18)	1.09(27)	0.76(19)		

For each β value, the uncertainty is given in parentheses.

Conclusion

We have studied the resonant Auger decay following photoionization of the 3d inner-shell orbital in krypton. The use of angle resolved two-dimensional imaging technique has enabled us to observe various processes over a large kinetic and photon

energy range. Spectator and shake probabilities for the $3d^{-1}np \rightarrow 4s^{-1}4p^{-1}(^1P)mp$ ($n = 5-9$, $m = 5,11$) resonance Auger transition have been studied and compared with previous non angular resolved measurements and a theoretical calculation by Mursu et al. [61]. Our results show that the spectator core coupling is strong at lower n excitation, but it lessens when higher n resonances are excited and the shake up transition becomes dominant. We also show at higher Rydberg n the importance of the one step shake-up processes. The comparison of our results with previous measurements and theoretical calculation for the $3d^{-1}np \rightarrow 4s^{-1}4p^{-1}(^1P)mp$ [61], the $3d^{-1}np \rightarrow 4p^4mp$ resonance Auger transition [57] and theoretical prediction [65] shows acceptable similarity.

Angular distributions of the Auger electrons resulting from the decay of the resonantly excited $3d^{-1}np$ states in krypton have been derived for the first time. Small β values have been observed when lower resonances are excited, but the values of β fluctuate at higher resonances.

We hope that our work, which gives the first angular distribution studies of the $3d^{-1}np \rightarrow 4s^{-1}4p^{-1}(^1P)mp$ resonance Auger transition, will stimulate further experimental and theoretical work, especially in the intermediate states of the quasi continuum which is just above the 3d-ionization threshold. This is where the shake down becomes more dominant than the shake up, and where more work is needed to understand how this evolution takes place.

CHAPTER VI

HIGH-RESOLUTION ANGLE-RESOLVED STUDY OF XE 4d \rightarrow 6p RESONANT AUGER PROCESS

Abstract

The Auger resonant Raman effect has been used as a method to eliminate the natural lifetime broadening in resonant Auger spectra. We have coupled this method for the first time with high-resolution photons from the Advanced Light Source to study angular distributions and decay rates of the Xe 4d_{5/2} \rightarrow 6p resonant Auger lines. The angular distribution parameters β of almost all possible final ionic 5p⁴(³P, ¹D, ¹S)6p states have been determined. Our data, which remove the discrepancy between previous lower-resolution experimental results, are compared to different theoretical results.

Introduction

The 4d \rightarrow 6p excitations in xenon represent one of the best-known examples of resonant Auger decay. Although the excitation is to an unfilled principal shell, the decay spectrum is quite complex due to the strong spin-orbit coupling in the xenon atom. This complexity demands that a sufficiently high resolution be employed in order to resolve the contributions from each of the spin-orbit components. To date no

truly high-resolution data have been reported for the angular distribution parameter β associated with the decay of these excitations. The highest resolution measurements thus far are the cross section results of Aksela et al. [69].

We report in this chapter an analysis of the angular distributions of the resonant Auger electrons resulting from the decay of the $4d_{5/2}^{-1}6p$ excitations. The data of this analysis are the results of experiments conducted at the ALS under double bunch operation. Xenon atoms were ionized by monochromatic synchrotron radiation from an 8-cm, 55-period undulator and spherical grating monochromator on beamline 9.0.1. We used a 925 lines/mm grating with a 100 μm entrance slit and a 60 μm exit slit providing us with a photon resolution of about 15 meV at the energy of the Xe $4d_{5/2} \rightarrow 6p$ resonance at 65.110 eV.

Results and Discussion

Figure 26 shows photoelectron spectra measured at an angle of 54.7° with respect to the electric field vector of the linearly polarized synchrotron beam. This figure, which corresponds to the Xe $4d_{5/2} \rightarrow 6p$ transition, shows the Xe $5s^{-1}5p^{-1}n'l'$, $5p^{-2}nl$, $5s^{-1}$ and $5p^{-1}$ transitions on resonance at 65.11 eV and off-resonance at 65.00 eV. Clearly, one can see that the intensity of most of the lines are dramatically enhanced on resonance, whereas there is almost no intensity gain in the $5p^{-1}$ and $5s^{-1}$ main lines. This indicates that the spectator decay dominates the participator decay.

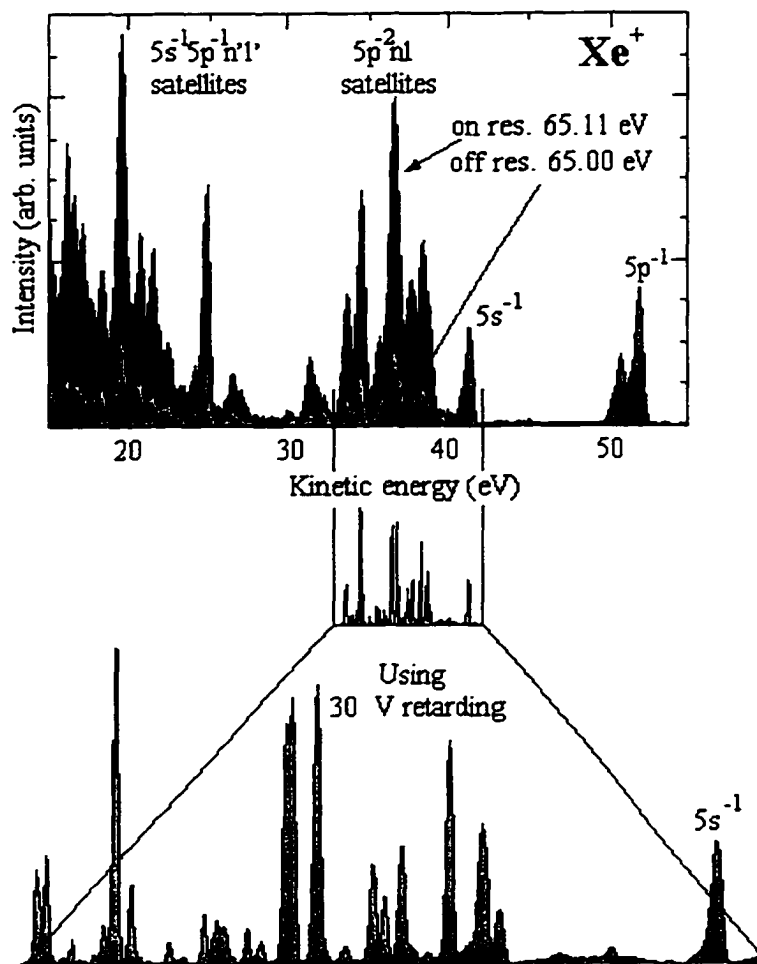


Figure 26. (a) Photoelectron Spectra Taken at the Magic Angle on and Below the $4d_{5/2} \rightarrow 6p$ Resonance. (b) Resonant Decay Spectrum in the Kinetic Energy Range Between 33 and 42 eV Using 30 V Retarding Potential.

In order to look in detail at the Xe $4d_{5/2}^{-1} 6p \rightarrow 5p^{-2} 6p$ correlation satellites, we used a retardation voltage of $V_{\text{ret}} = -30$ V on the electron spectrometers without any loss of resolution. In Figure 27, the same energy range taken at the magic angle and at 0° is shown in the context of the previous angle integrated measurements from Aksela et al. [69] as well as the first angle resolved data from Carlson et al. [15].

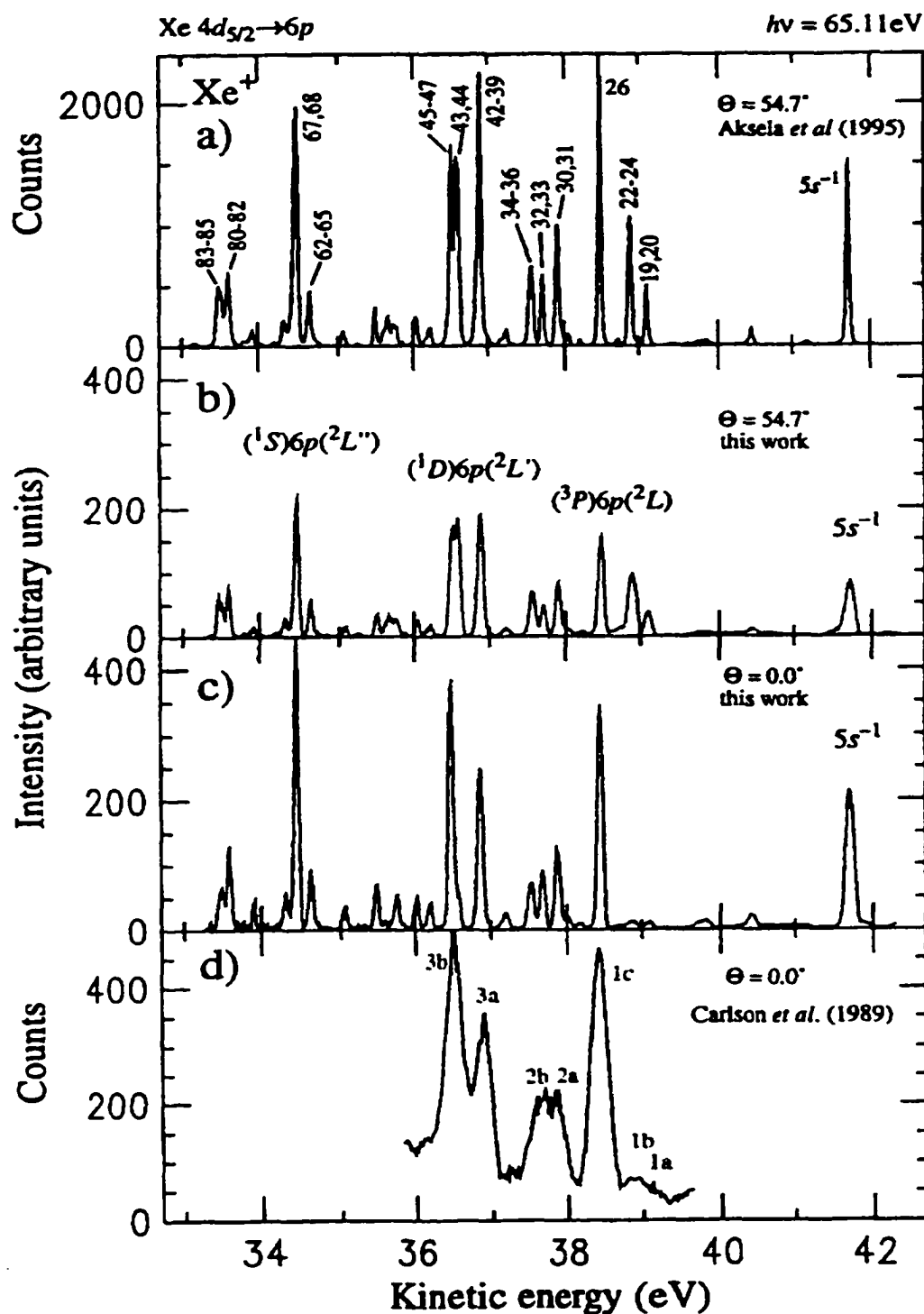


Figure 27. Decay Spectra of the $\text{Xe } 4d_{5/2} \rightarrow 6p$ Resonance Taken at the Magic Angle: (a) Aksela et al. [69] and (b) this Work.. Resonance Spectra Taken at 0° : (c) This Work and (d) Carlson et al. [15].

It can be seen clearly that with this retardation potential (30 V), in the low energy side of the spectrum (Figure 27 a and b) our resolution matches that of the best resolved decay spectra from Aksela et al. [69]. Figure 28 shows a section of the decay spectrum recorded with a 32 V retarding potential at three different angles ($\theta = 0^\circ$, 54.7° and 90°). We fit Gaussian curves to our data to determine the areas under the peaks. In order to stabilize the fitting procedure, the energy differences between overlapping peaks were fixed using experimental energy values from Aksela et al. [69]. With our time-of-flight spectrometers, the linewidth is a nearly linear function of the electron kinetic energy. From the well separated (^3P) $6\text{p}(^2\text{P}_{3/2})$ peak (line 26 in Figure 27) the kinetic energy resolution for this experiment was found to be 1.1% and 1.0% of the final kinetic electron energy with retarding voltages of 30 and 32 V, respectively. The linewidths for all lines were connected in a way that the relative resolution remained constant. From the lines' areas at different angles we derived the angular distribution parameters β for each of the final states as shown in Figure 28 d. The results for the relative intensities and the angular distribution parameters β are shown in Table 11 together with theoretical calculations from Tulkki et al. [70], Chen [22], and Hergenhahn et al. [20,71]. Chen [22], Tulkki et al. [70], and Hergenhahn et al. [71] used a multiconfiguration Dirac-Fock method in intermediate coupling with configuration interaction, whereas the older calculations of Hergenhahn et al. [20] were carried out in jk coupling applying a strict spectator model. Only Tulkki et al. [70] included coupling between different continuum channels in their calculation. All the theoretical calculations have in common that both the direct photoionization and the participator

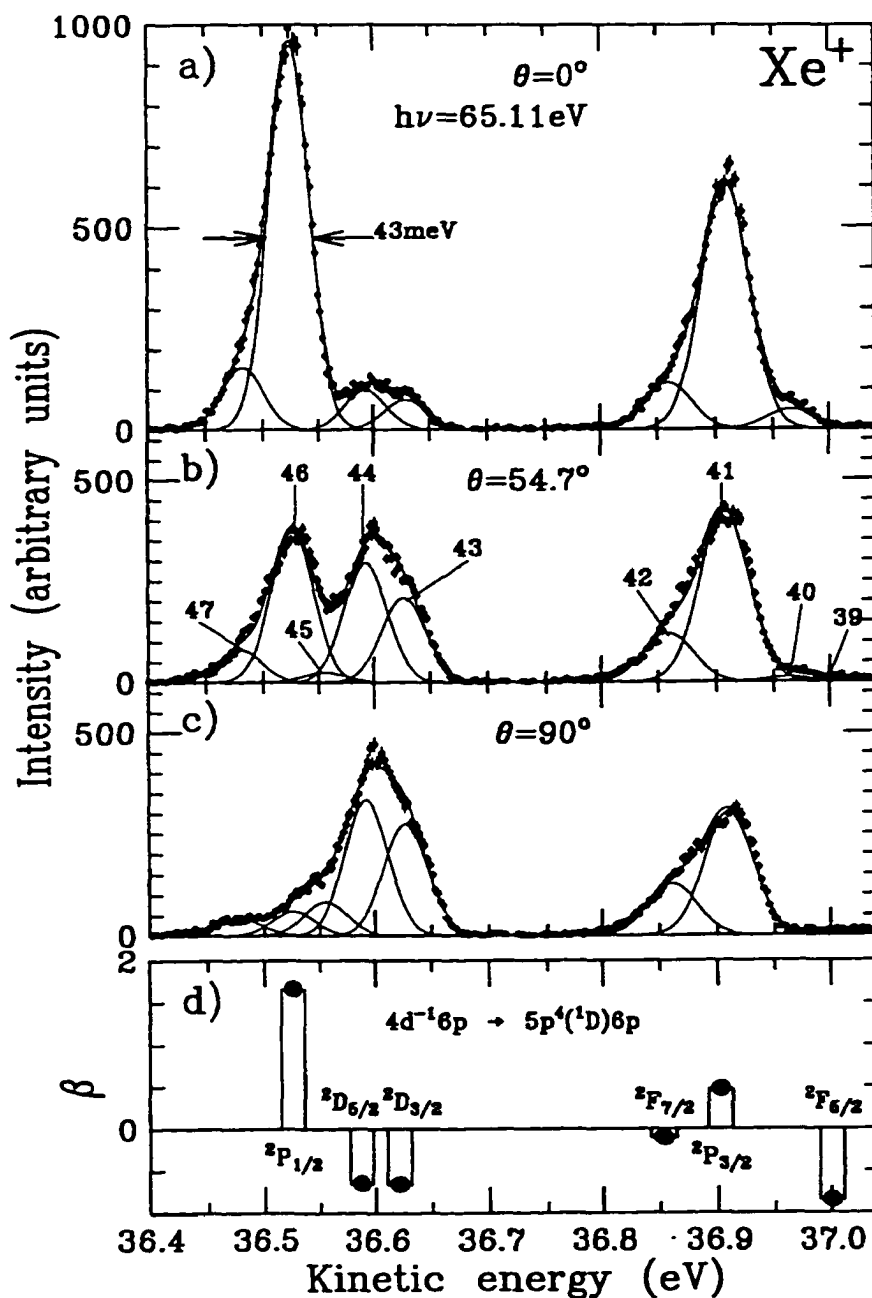


Figure 28. Xe $5p^4nl$ Decay Spectra after $4d_{5/2} \rightarrow 6p$ Resonant Excitation in the Kinetic Energy Range of 36.4-37.1 eV at (a) 0° , (b) 54.7° , and (c) 90° With Respect to the Polarization of the Incident Photons. The Spectra Were Measured With 32 V Retarding Potential Corresponding to a Spectrometer Resolution of Between 43 and 50 meV in the Display Region. (d) Shows the Angular Distribution Parameter β for the $5p^4(^1D)6p$ Spectator Line.

Table 11

Intensities and β Parameters of the Electron Spectrum of Xe $4d_{5/2} \rightarrow 6p$ Excitation
(65.11 eV)

Final ionic state Term	Line in Experi- ment	Kinetic energy (eV) ^a	Relative Inten- sity	β	β theory			
					Ref. [70]	Ref. [22]	Ref. [71]	Ref. [20]
$5p^4(^3P)6p$ $^4P_{3/2}$	19	39.119	2.0(5)	1.4(6)	1.045	0.984	0.061	1.014
$(^3P)6p$ $^4P_{5/2}$	20	39.098	23.2(7)	-0.85(3)	-0.994	-1.000	-0.999	-0.998
$(^3P)6p$ $^2D_{3/2}$	22	38.906	37.5(8)	-0.967(1)	-0.994	-1.000	-1.000	-0.998
$(^3P)6p$ $^2S_{1/2}$	23	38.886	17.1(6)	-0.69(3)	-0.448	0.215	0.157	0.451
$(^3P)6p$ $^4D_{7/2}$	24	38.882			-0.588	-0.974	-0.923	-0.932
$(^3P)6p$ $^2P_{3/2}$	26	38.501	100	1.30(2)	1.030	1.018	0.972	1.014
$(^3P)6p$ $^2P_{1/2}$	28	37.988	5.0(2)	1.03(7)	0.984	0.962	0.749	n. a. ^b
$(^3P)6p$ $^4P_{1/2}$	30	37.955	7.1(3)	-0.13(6)	0.233	0.774	0.927	1.000
$(^3P)6p$ $^2D_{3/2}$	31	37.899	42.8(5)	0.73(3)	0.656	0.653	0.910	0.800
$(^3P)6p$ $^4D_{5/2}$	32	37.716	1.3(4)	0.3(6)	-0.188	-0.331	-0.323	0.737
$(^3P)6p$ $^4S_{3/2}$	33	37.627	24.0(6)	1.13(5)	0.745	0.955	0.557	-0.861
$(^3P)6p$ $^4D_{3/2}$	34	37.570	22.1(5)	-0.14(3)	-0.536	-0.860	-0.764	-0.861
$(^3P)6p$ $^4D_{1/2}$	36	37.535	19.5(4)	0.52(3)	0.593	0.935	0.817	1.000
$(^1D)6p$ $^2F_{5/2}$	39	37.001	2.10(14)	-0.85(10)	-0.875	-0.860	-0.914	-0.928
$(^1D)6p$ $^2P_{3/2}$	41	36.902	82.7(10)	0.47(2)	0.175	0.073	0.319	-0.399
$(^1D)6p$ $^2F_{7/2}$	42	36.853	24.3(5)	-0.11(3)	0.246	0.052	0.116	0.112
$(^1D)6p$ $^2D_{3/2}$	43	36.621	39.90(7)	-0.66(2)	-0.553	-0.375	-0.375	-0.399
$(^1D)6p$ $^2D_{5/2}$	44	36.587	51.0(8)	-0.65(2)	-0.888	-0.882	-0.930	-0.928
$(^1D)6p$ $^2P_{1/2}$	46	36.521	63.1(6)	1.66(2)	1.503	1.307	0.55	0.373
$(^1S)6p$ $^2P_{1/2}$	65	34.602	1.6(3)	0.73(4)	0.130	-0.139	-0.035	n.a. ^b
$(^1S)6p$ $^2P_{3/2}$	67	34.479	98.9(6)	1.17(4)	0.928	0.847	0.754	0.800

^a According to Aksela et al. [69]

^b Not allowed

Intensities are normalized to the well separated $(^3P)6p(^2P_{3/2})$ line.

decay are neglected, and these approximations have been verified experimentally [10,12].

Comparing our results to the different calculations, we find that the agreement varies between excellent and poor, depending on the configuration and method used. For some lines (20,22,31,39), the agreement is excellent, and for others (24,43,44) the agreement between our experimental anisotropy parameters and the results from all four calculations is good. For other lines (30,34,41,65) the theoretical values are in disagreement with each other and with our experimental values. Finally, there are some state configurations where our data agree with one or the other calculations. For instance, Chen [22] comes close to our β value for the (^3P)6p($^4\text{S}_{3/2}$) state (line 33), whereas Tulkki et al. [70] and Hergenhaben et al. [20] do not even have the correct sign. On the other hand, for the (^3P)6p($^4\text{D}_{1/2}$) peak (line 36), Tulkki et al. [70] give almost the same β value as the experiment but the other calculations are off. Interestingly, there is almost a perfect agreement between all theories for our reference peak (^3P)6p($^4\text{P}_{3/2}$) (line 26), but the experimental β value is significantly larger. We were able to observe the splitting of the (^1S)6p($^2\text{P}_{3/2}$) state (lines 67 and 68), as Aksela et al. [69] did, but the fitting procedure was very sensitive to even small changes in the positions and widths of the peak. Therefore, in Table 11 we give only the average β for those lines. In Table 12 we compare our β results with previous experimental data from Carlson et al. [15] with very low resolution, Becker et al. [72], and Kämmerling et al. [14]. There is in general, good agreement between our experiment and these results.

It should be noted that the statistical uncertainty of the last digits is given in brackets. The identification of the peaks in the case of Chen [22], was done with respect to his calculated energies. For Hergenhahn et al. [20,71] the energies of Hansen and Persson [73] were used for their identification.

Table 12

β Parameters of the Electron Spectrum of Xe after $4d_{5/2} \rightarrow 6p$ Excitation With Previous, Low Resolution Data

Line(s)			β		
No. ^a	No. ^b	Present work	I ^c	II ^d	III ^b
19,20	1a	-0.66(6)	-0.60(3)	-0.67(5)	-0.88
22-24	1b	-0.88(2)	-0.90(2)	-0.93(3)	-0.93
26	1c	1.30(2)	1.31(2)	1.35(6)	0.82
28-31	2a	0.65(4)	0.58(2)	0.89(6)	0.26
32-36	2b	0.52(5)	0.54(3)	0.45(6)	0.16
39-42	3a	0.36(4)	0.23(2)	0.55(5)	-0.02
43-47	3b	0.28(3)	0.33(5)	0.46(5)	-0.09
67,68	5	1.17(4)	0.83(5)	1.09(6)	0.51

a. According to Aksela et al. [69].

b. Carlson et al. [15].

c. Kämmerling et al. [14].

d. Becker et al. [72].

Conclusion

Time of flight electron spectroscopy in combination with tunable synchrotron radiation provided by a third generation storage ring has been used to study the angular distributions of the Xe spectator lines following Xe $4d_{5/2} \rightarrow 6p$ excitation. The

high resolving power of the monochromator as well as of our electron analyzers allowed us to determine the β parameters of almost all possible final ionic $5p^4(^3P, ^1D, ^1S)6p$ states with many of them being much closer than the natural linewidth of the 4d inner shell hole (111 meV [4]). Our results published in ref. [17] appear to remove the existing experimental discrepancy. A comparison with different theoretical calculations shows a partly good agreement, but there is room for improvement for some lines.

CHAPTER VII

CONCLUSION

Time of flight electron spectroscopy in combination with tunable synchrotron radiation, provided by a 3rd generation storage ring, has been used to study electron angular distributions of the resonant Auger processes in Ar, Kr, and Xe.

In the case of Ar, we have measured the resonant Auger spectra of the $2p^{-1}4s$ and the $2p^{-1}3d,4d$ inner-shell excited states with high energy resolution. The intensity distributions and the angular distribution anisotropies β have been reported for nearly all of the $3p^4nl$ final ionic states. The decay of the $2p^{-1}4s$ state appears to be dominated by spectator decay, in which the excited electron remains in the same orbital, while the decay of the $2p^{-1}3d,4d$ state appears to be dominated by shake-up processes. Our results confirm previous reports that the spectator model of Hergenbahn et al. [20] accurately describes the intensity distributions and β parameters for the $2p^{-1}4s$ resonance but demonstrate the break down of this model for the $2p^{-1}3d,4d$ resonances. A very good agreement has been found by comparing our experimental results with calculations made by Chen [22], who used the MCDF method with intermediate coupling and configuration interaction. For both intensity and angular distributions, models treating the $2p^{-1}4s$ resonant Auger decay as a two step process produce the most accurate results. For each of the resonances studied ($2p^{-1}4s$, 3d and 4d), the reported β parameters for most of the final ionic states were small positive values or ne-

gative values, indicating a preferred electron ejection isotropically. These results demonstrate the enhanced population of parity unfavored states that can be reached through resonant Auger processes [48].

In the case of Kr, we have studied the resonant Auger decay of the Kr $3d^{-1}np$ states using angle-resolved electron imaging spectroscopy, which enabled us to observe various processes over a large kinetic and photon energy. Spectator and shake probabilities for the $3d^{-1}np \rightarrow 4s^{-1}4p^{-1}(^1P)mp$ ($n = 5-9$, $m = 5-11$) resonant Auger transitions have been studied. Our results show that the spectator core coupling is strong at lower n ($n = 5-6$) but it lessens for higher n , with a shake-up of $m = n + 1$ preferred. Similar behavior is obtained when comparing the above mentioned probabilities with previous experimental and theoretical spectator and shake probabilities [61] and with experimental spectator and shake probabilities for the Kr $3d^{-1}np \rightarrow 4s^2 4p^{-2}mp$ resonance Auger transition [57].

In the case of Xe, by utilizing the Auger resonant Raman effect, the lifetime broadening has been eliminated in the Xe $4d^{-1}6p$ resonant Auger spectra. This allowed us to measure resolved lines and to determine the relative intensities of the separated resonant Auger transition with an accuracy that made possible a detailed comparison with theory. It also allowed us to determine the angular distribution parameters β of almost all possible final ionic $5p^4(^3P, ^1D, ^1S)6p$ states. Moderate resolution would smear out the detailed fine structure, making it impossible to test whether the partial transition rates are correctly reproduced by theory. As mentioned above, for all the experiments conducted in this thesis, we used the method of time-of-flight

(TOF) spectroscopy to detect and energy resolve electrons ejected after a photon-atom interaction. There are several advantages and disadvantages in using this method. For instance, TOF spectroscopy allows an entire photoelectron spectrum to be measured at once so that all features within a certain kinetic energy window are recorded during the same period of time. Furthermore, since multiple peaks can be recorded simultaneously, TOF spectroscopy has high efficiency. Finally, random events such as dark noise are averaged over a large number of channels.

One disadvantage inherent to TOF spectroscopy is the non-linearity of the energy scale and the decrease of spectrometer resolution at higher kinetic energies as mentioned in Chapter V. The resolution of the TOF analyzer is not the best resolution that one can achieve. There are other analyzers that offer better resolution than the TOF analyzer, for example, the hemispherical analyzers (Scienta SES-200 analyzer). The use of such spectrometers will allow one to resolve more spectral lines, and hence make a better comparison with theoretical models. However, our experimental method allowed us in a very short amount of time to improve previous results and to measure, for the first time, several angular distribution parameters with good resolution.

We hope that this work will stimulate further theoretical and experimental investigations.

REFERENCES

- [1] T. Koopman, *Physical* **1**, 104 (1934).
- [2] K. Codling and P. Madden, *Phys. Rev. Lett.* **12**, 1432 (1964).
- [3] U. Fano and W. Cooper, *Rev. Mod. Phys.* **40**, 441 (1968).
- [4] G. C. King, M. Tronc, F. H. Read, and R. C. Bradfrd, *J. Phys. B: At. Mol. Opt. Phys.* **10**, 2479 (1977).
- [5] G. C. King, and F. H. Read, *Atomic Inner-shell Physics*, ed. B. Crasemann (New York: Plenum) **317**, (1985).
- [6] U. Fano and W. Cooper, *Phys. Rev. A* **137**, 1364 (1965).
- [7] T. Hayaishi, Y. Morioka, Y. Kageyama, M. Watanabe, I. H. Suzuki, A. Mikuni, G. Isoyama, S. Asaoka, and N. Nakamura, *J. Phys. B: At. Mol. Opt. Phys.* **17**, 3511 (1984).
- [8] D. W. Lindle, P. A. Heimann, T. A. Ferrett, M. N. Piancastelli, and D. A. Shirley, *Phys. Rev. A* **35**, 4605(1987).
- [9] S. H. Southworth, U. Becker, C. M. Truesdale, P. H. Kobrin, D. W. Lindle, S. Owaki, and D. A. Shirley, *Phys. Rev. A* **28**, 261(1983).
- [10] U. Becker, T. Prescher, E. Schmidt, B. Sonntag, and H. E. Wetzel, *Phys. Rev. A* **33**, 3891 (1986).
- [11] V. Schmidt, S. Krummacher, F. Wuilleumier, and P. Dhez, *Phys. Rev. A* **28**, 261 (1981).
- [12] H. Aksela, S. Aksela, G. M. Bancroft, K. H. Tan, and H. Pulkkinen, *Phys. Rev. A* **33**, 3867 (1986).
- [13] H. Aksela, S. Aksela, H. Pulkkinen, G. M. Bancroft, and K. H. Tan, *Phys. Rev. A* **33**, 3876 (1986).
- [14] B. Kämmerling, B. Krässig, and V. Schmidt, *J. Phys. B: At. Mol. Opt. Phys.* **23**, 4487 (1990).

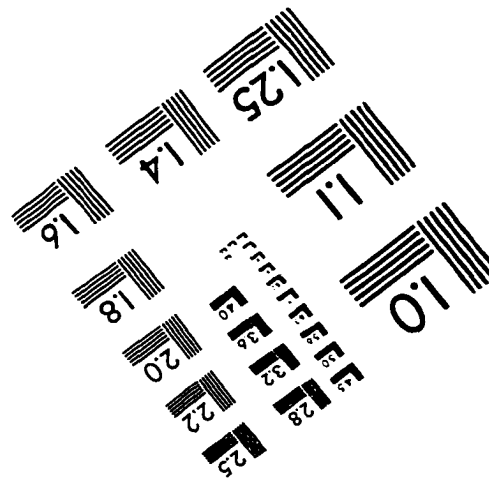
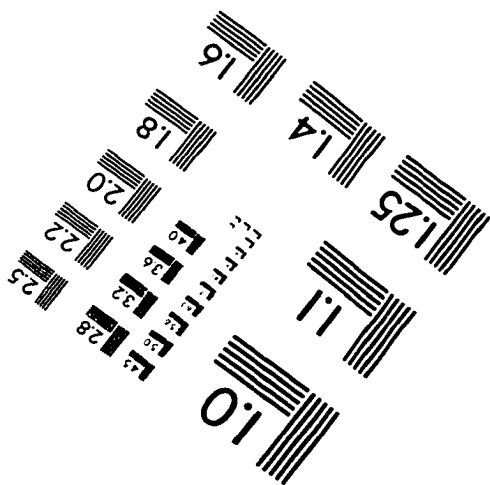
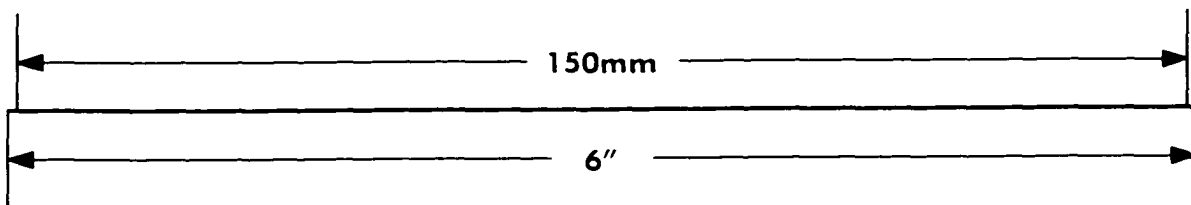
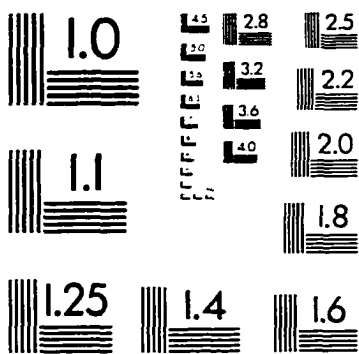
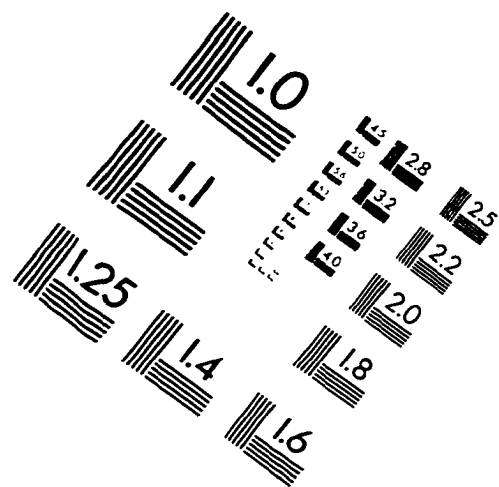
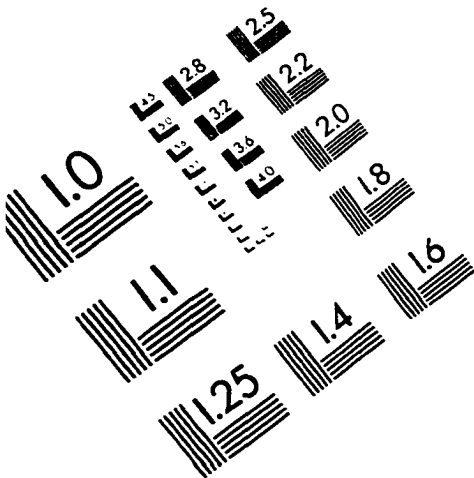
- [15] T. A. Carlson, D. R. Mullins, C. E. Beall, B. W. Yates, J. W. Taylor, D. W. Lindle, and F. Grimm, *Phys. Rev. A* **39**, 1170 (1989).
- [16] C. D. Caldwell, in *Alignment in Low-Energy Photoionization*, 15th International conference on X-ray and Inner-shell Processes, edited by T. A. Carlson, M. O. Krause, and S. T. Manson (AIP, Knoxville, 1990), p. 685.
- [17] B. Langer, N. Berrah, A. Farhat, O. Hemmers, and J. D. Bozek, *Phys. Rev. A* **53**, R1946 (1996).
- [18] C. D. Caldwell and S. Hallman, *Phys. Rev. A* **53**, 3344 (1996).
- [19] J. W. Cooper, *Phys. Rev. A* **39**, 3714 (1989).
- [20] U. Hergenhahn, N. M. Kabachnik, and B. Lohmann, *J. Phys. B: At. Mol. Opt. Phys.* **24**, 4759 (1991).
- [21] M. H. Chen, *Phys. Rev. A* **45**, 1684 (1992).
- [22] M. H. Chen, *Phys. Rev. A* **47**, 3733 (1993).
- [23] M. O. Krause, *Photoionization and Other Probes of Many-electron Interactions*, ed. F. Wuilleumier (New York : Plenum) 133 (1976).
- [24] E. Fermi, *Rev. Mod. Phys.* **4**, 87 (1932).
- [25] C. Cohen-Tannoudji, B. Diu, and F. Laloë, *Quantum Mechanics*, Vols. I and II (Paris : Hermann), (1977).
- [26] H. A. Bethe, and E. E. Salpeter, *Quantum Mechanics of One and Two Electron atoms*, (Berlin : Springer), (1957).
- [27] S. T. Manson, *J. Electron Spectrosc. Relat. Phenom.* **41**, 73 (1976).
- [28] F. Wuilleumier, *Photoionization and Other Probes of Many-electron Interactions*, (New York : Plenum) 133 (1976).
- [29] J. W. Cooper, *Photoionization and Other Probes of Many-electron Interactions*, ed. F. Wuilleumier (New York : Plenum) 133 (1976).
- [30] J. W. Cooper and R. N. Zare, *Lectures in Theoretical Physics*, Vol. XI-C (New York : Gordon and Breach) 317 (1969).

- [31] J. A. Samson and A. F. Starace, *J. Phys. B: At. Mol. Opt. Phys.* **8**, 1806 (1975).
- [32] A. F. Starace and S. Shahabi, *Phys. Rev. A* **25**, 2135 (1982).
- [33] H. Derenbach and V. Schmidt, *J. Phys. B: At. Mol. Opt. Phys.* **17**, 83 (1984).
- [34] J. Berkowitz, *Photoabsorption, Photoionization, and Photoelectron Spectroscopy*, Academic press (1979).
- [35] B. Langer, A. Farhat, B. Nessar, N. Berrah, O. Hemmers, and J. D. Bozek, in *Proceedings of the "Atomic Physics with Hard X-rays from High Brilliance Synchrotron Light Sources" Workshop*, ANL/APS/TM-16, p. 245 (1996).
- [36] F. R. Elder, A. M. Gurewitsch, R. V. Langmuir, and C. Pollock, *Phys. Rev.* **71**, 829 (1947).
- [37] F. Wuilleumier, *Review of Fundamental Processes and Applications of Atoms and Ions*, C. D. Lin, ed., World Scientific (1993).
- [38] Taken from *ALS Beamlines for Independent Investigators*, prepared by the Advanced Light Source, Lawrence Berkeley National Laboratory (1992).
- [39] H. Aksela, S. Aksela, H. Pulkkinen, G. M. Bancroft, and K. H. Tan, *Phys. Rev. A* **37**, 1798 (1988).
- [40] P. A. Heimann, D. W. Lindle, T. A. Ferrett, S. H. Liu, L. J. Medhurst, M.N. Piancastelli, D. A. Shirley, U. Becker, H. G. Kerkhoff, B. Langer, D. Szostak, and R. Wehlitz, *J. Phys. B: At. Mol. Phys.* **20**, 5005 (1987).
- [41] M. Meyer, E. von Raven, M. Richter, B. Sonntag, and J. E. Hansen, *J. Electron Spectrosc. Relat. Phenom.* **51**, 407 (1990).
- [42] M. Meyer, E. von. Raven, B. Sonntag, and J. E. Hansen, *Phys. Rev. A* **43**, 177 (1991).
- [43] M. Meyer, E. von Raven, B. Sonntag, and J. E. Hansen, *Phys. Rev. A* **49**, 3685 (1994).
- [44] H. Aksela and J. Mursu, *Phys. Rev. A* **54**, 2882 (1996).
- [45] R. Camilloni, M. Zitnik, C. Comicioli, K. C. Prince, M. Zacchigna, C. Crotti, C. Ottaviani, C. Quaresima, P. Perfetti, and G. Stefani, *Phys. Rev. Lett.* **77**, 2646 (1996).

- [46] L. Minnhagen, *Arkiv För Fys.* **25** 203 (1963).
- [47] A. Menzel, Ph.D. Thesis, Technische Universität Berlin (1990, unpublished).
- [48] B. Langer, J. Viefhaus, O. Hemmers, A. Menzel, R. Wehlitz, and U. Becker, *Phys. Rev. A* **51**, R882 (1995).
- [49] M. Meyer, Ph.D. Thesis, Universität Hamburg (1990, unpublished).
- [50] J. Mursu, H. Aksela, O-P Sairanen, A. Kivimäki, E. Nömmiste, A. Ausmees, S. Svensson, and S. Aksela, *J. Phys. B: At. Mol. Opt. Phys.* **29**, 4387 (1996).
- [51] A. Farhat, M. Humphrey, B. Langer, N. Berrah, J. D. Bozek and D. Cubaynes, *Phys. Rev. A* **56**, 501 (1997).
- [52] B. Langer, N. Berrah, A. Farhat, M. Humphrey, J. Bozek and U. Becker, *J. Phys. B: At. Mol. Opt. Phys.* **30**, 4255 (1997).
- [53] W. Eberhardt, G. Kalkoffen, and C. Kunz, *Phys. Rev. Lett.* **41**, 156 (1978).
- [54] B. Kämmerling, B. Krässig, O. Schwarzkopf, J. P. Ribeiro, and V. Schmidt, *J. Phys. B: At. Mol. Opt. Phys.* **25**, L5-L10 (1992).
- [55] H. Aksela, J. Jauhianien, E. Kukk, E. Nömmiste, S. Aksela, and J. Tulkki, *Phys. Rev. A* **53**, 290 (1996).
- [56] A. Kikas, S. J. Osborne, A. Ausmees, S. Svensson, O. P. Sairanen, and S. Aksela, *J. Electron Spectrosc. Relat. Phenom.* **77**, 241 (1996).
- [57] J. Jauhianien, H. Aksela, O-P Sairanen, E. Nömmiste, and S. Aksela, *J. Phys. B: At. Mol. Opt. Phys.* **29**, 3385 (1996).
- [58] H. Aksela, M. Kivilompolo, E. Nömmiste, and S. Aksela, *Phys. Rev. Lett.* **25**, 4970 (1997).
- [59] H. Aksela, S. Aksela, A. Mäntykenttä, J. Tulkki, E. Shigmasa, A. Yagishita, and Y. Furusawa, *Phys. Scr. T* **41**, 113 (1992).
- [60] G. B. Armen, *J. Phys. B: At. Mol. Opt. Phys.* **29**, 677 (1996).
- [61] J. Mursu, J. Jauhianien, H. Aksela, and S. Aksela, *J. Phys. B: At. Mol. Opt. Phys.* **31**, 1973 (1998).
- [62] T. Åberg, *Ann. Acad. Sci. Fennicae, Scr. A* **VI** (1969).

- [63] R. L. Martin and D. A. Shirley, *Phys. Rev. A* **13**, 1475 (1976).
- [64] R. Arneberg, J. Müller, and R. Manne, *Chem. Phys.*, **64**, 249 (1982).
- [65] T. Åberg, *Physica Scripta* **T41** 71 (1992).
- [66] D. Cubric, A. A. Wills, J. Comer, and M. A. MacDonald, *J. Phys. B: At. Mol. Opt. Phys.* **25**, 5069 (1992).
- [67] N. Berrah, B. Langer and A. Farhat, *Proceedings of the Raman Emission by X-Rays (REX-1) Workshop*, Published World Scientific, Editors D. L. Ederer and J. H. McGuire, p. 156 (1996).
- [68] H. Aksela, S. Aksela, O-P Sairanen, A. Kivimäki, A. Naves de Brito, E. Nömmiste, J. Tulkki, S. Svensson, A. Ausmees and S. J. Osborne, *Phys. Rev. A* **49**, R4269 (1994).
- [69] H. Aksela, O-P Sairanen, S. Aksela, A. Kivimäki, A. Naves de Brito, E. Nömmiste, J. Tulkki, A. Ausmees, S. J. Osborne, and S. Svensson, *Phys. Rev. A* **51**, 1291 (1995).
- [70] J. Tulkki, H. Aksela, and N. M. Kabachnik, *Phys. Rev. A* **50**, 2366 (1994).
- [71] U. Hergenhahen, B. Lohmann, N. M. Kabachnik, and U. Becker, *J. Phys. B: At. Mol. Opt. Phys.* **26**, L117 (1993).
- [72] U. Becker et al., quoted in Ref. [20]; R. Weckwerth, Diplomarbeit (diploma thesis), Technical University Berlin, 1991 (unpublished).
- [73] J. E. Hanson and W. Persson, *Phys. scr.* **36**, 602 (1987).

IMAGE EVALUATION TEST TARGET (QA-3)



APPLIED IMAGE, Inc
 1653 East Main Street
 Rochester, NY 14609 USA
 Phone: 716/482-0300
 Fax: 716/288-5989

© 1993, Applied Image, Inc., All Rights Reserved